EXPLOITING METAMATERIALS: FUNDAMENTALS AND APPLICATIONS

by

Morteza Karami

A dissertation submitted to the faculty of
The University of North Carolina at Charlotte
in partial fulfillment of the requirements
for the degree of Doctor of Philosophy in
Electrical Engineering

Charlotte

2017

Approved by:

____
Dr. Michael A. Fiddy

____
Dr. Ryan Adams

____
Dr. Ishwar D. Aggarwal

____
Dr. Thomas P. Weldon

____
Dr. Alireza Tabarraei

ABSTRACT

MORTEZA KARAMI. Exploiting Metamaterials: Fundamentals and Applications.
(Under the direction of DR. MICHAEL A. FIDDY)

Metamaterials are man-made structures developed to engineer electromagnetic waves, and they have been studied intensely in recent decades. Although there are still debates about the performance of these types of artificial materials, many practical applications have been demonstrated using metamaterials from the RF and microwave to IR and optical frequencies. Moreover, due to their unique advantages, they might soon find their path in products and technologies to replace traditional optical and electromagnetic devices. In this dissertation, we primarily study a structure composed of S-shape resonators which show a negative refractive index in a range of frequencies, between 5GHz to 9GHz. We investigate the methods to calculate the constitutive electromagnetic parameters of this metamaterial and offer paths to enhance its performance regarding incident wave polarization. We also propose a meta-substrate to engineer bandwidth of the S-resonator metamaterial. Moreover, we explore properties the proposed metamaterial design for various applications including super-resolution imaging, sensing, and filtering. Planar metamaterials are a 2D version of metamaterials which offer novel applications due to their compact size and low loss. Here, we explore properties of a double ring metasurface for making filters and modulators. Finally, nonlinear effects in metamaterial structures are studied, and a new numerical tool is developed to design metamaterials with natural Two-Photon Absorption nonlinear effect.

To my parents, Soheila and Akbar.
And to my brothers, Alireza and Mostafa.
Whom without them I would not be here today.

ACKNOWLEDGEMENTS

This journey through graduate school would not be complete without Dr. Michael Fiddy's role. His virtues, both academic and personal, improved my ability in accomplishing these projects, and I am truly grateful to him for accepting to be my adviser on this journey. I would also like to acknowledge the committee members who participated in the process of the dissertation and thank them for their kindness; Dr. Ryan Adams, Dr. Ishwar D. Aggarwal, Dr. Thomas Weldon, and Dr. Alireza Tabarraei. Also, I would like to thank Dr. Faramarz Farahi for his support throughout my Ph.D. studies.

During past years, I had the opportunity to receive technical tips from different people who I am thankful for their support. The list includes Dr. Jeff Tharp from Ansys who provided valuable inputs on working with HFSS at my first steps in this work, Dr. Robert Ingel in our research group for sharing his knowledge and insight, and my friends Mehrdad, Mohammad, Iman, and Lina who provided me with help and support.

The last but not the least, I would also gratefully acknowledge the ongoing support through the grant of ARO W911NF-14-1-0299.

TABLE OF CONTENTS

LIST OF FIGURES

CHAPTER 1: INTRODUCTION

1.1. Introduction to Metamaterials

Metamaterials are artificial engineered materials and structures composed of building blocks (meta-atoms) of which their size and spacing of meta-atoms are at deep sub-wavelength scale. A peculiar feature of metamaterials is that their effective properties are usually not found in nature. These metamaterials are multi-material systems in mesostructures which exhibit an effective response to corresponding fields that is different from each component material which builds the metamaterial. Conventionally, metamaterials received attentions in electromagnetics and optics to achieve novel results not occurring in nature such as invisibility cloak, negative refractive index, super-resolution imaging, artificial chirality, and hyperbolic dispersion relation. However, the methodology has been applied to various fields such as acoustic, heat transfer, and mechanical structures to obtain new hybrid material responses which are influenced by the properties of the parent materials, but yet demonstrate significantly different characteristics. These engineered structures usually find their unusual properties when their geometrical units, also called meta-atoms, are in the subwavelength scales compared to the fields in their surroundings. In optics and electromagnetics which are the focus of this dissertation, the metamaterial unit cells are arranged periodically to produce optimal effective properties which are drastically unlike the composite materials. The building blocks of metamaterials are usually a combination of metals and dielectrics, and their geometries have a dominant role in defining the effective response of the structure. For instance, in a certain kind of hyperbolic metamaterials, the electromagnetic response of the metal-dielectric multilayers depends on periodic constant and widths of metal and the dielectric layer in the unit cell. In other words, filling factors are crucial in designing metamaterials with desired parameters. This collective behavior is along with the classical methods such as the effective medium theory that suggest an analytical explanation of composite materials, and consider their behavior as a homogenous medium.

Early studies on electromagnetic metamaterials began at the end of the 19th century [1]. The history of theoretical exploration of fundamental light-matter interactions and wave studies in metamaterial goes back to ideas of negative phase velocity and anti-parallel group velocity in Lamb and Schuster's works [2], [3]. Although they did not believe in the existence of these phenomena in practice, the research on this artificial electromagnetic structure continued by several other scientists and engineers [4]–[7]. However, the primary coherent theoretical research which is considered to be the beginning of the metamaterial field was proposed in Veselago's work in 1968 [8]. However, experimental realization of electromagnetic metamaterials took another three decades when Smith and Schultz presented the first metamaterial with simultaneous negative ε and μ in microwave frequencies [9]. In the last years, metamaterial field has expanded significantly. The incredible increase in computing powers let researchers design optimum metamaterial structures with desired parameters, and advances in nanofabrication technologies allowed us to essentially explore the novel properties and applications of metamaterials in optics and photonics. So far, a very wide range of areas has received new ideas from metamaterials including telecommunications, photovoltaics, super-resolution imaging, sensing, and photonics and quantum computing. Although future of metamaterials is promising, the current practical use of them is limited by constraints in fabrication technologies and proper materials to achieve such efficient metamaterial devices which can compete with other conventional systems.

1.2. Electromagnetic Metamaterials

The electromagnetic properties of material are usually specified in terms of its electric permittivity ε, permeability μ, and index of refraction $n = \sqrt{\varepsilon\mu}$. These quantities are typically tensors. Most common materials have $|\varepsilon| \geq 1$ and $|\mu| \geq 1$ as shown in Figure 1.1. The exceptions are $\varepsilon < 0$ in plasmas such as metals at optical frequencies and $\mu < 0$ for some ferromagnetics. However, no material has been found in nature to show simultaneously negative ε and μ and also low loss, especially at higher electromagnetic frequencies.

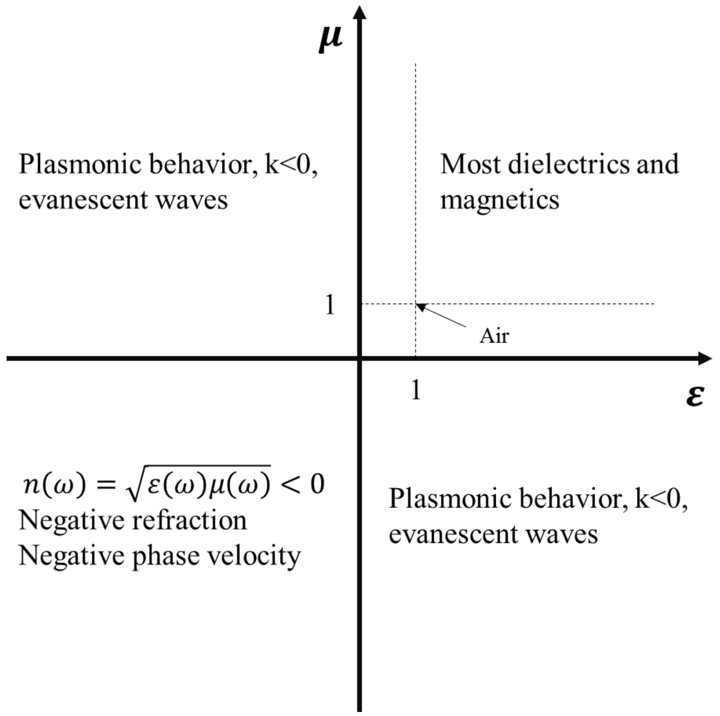

Figure 1.1: Electromagnetic wave propagation in materials with various values of ε and μ.

Metamaterials are different from photonic or electromagnetic bandgap structures in a few fundamental aspects even though they are both periodic electromagnetic structures. One of the major differences is that the lattice constant scale in metamaterials is very small compared to the effective wavelength in the medium. Meta-atoms likewise atoms and molecules could take dipole moments and resonate independently. Therefore, the structure is dispersive, and we can apply effective medium theories to extract their constitutive parameters as they are in a quasi-static region. On the other hand, for bandgap structures, when the periodicity becomes comparable or larger than the incident wavelength, we can no longer apply the effective medium theory. A more complicated and elaborate theory is required to describe the electromagnetic field behavior inside the material array. The Floquet-Bloch theory is a conventional method to analyze such structures in which the electromagnetic fields are expanded into an infinite sum of plane waves propagating in all directions.

A paper by Veselago in 1968 studied the electrodynamics of waves in a medium with both ε and μ negative [8]. It predicts many new phenomena such as negative Snell's law, backward wave propagation, reverse Cerenkov radiation, and reverse Doppler's effect. Until 1996, no solid evidence was suggested, and then Pendry et al. proposed a wire array medium to achieve $\varepsilon < 0$, and split ring resonators (SRR's) to obtain $\mu < 0$ [10], [11]. Just a year later, Smith et al. experimentally demonstrated the first negative index material by combining wire and SRR's [9], and this opened the door to the new field of negative index metamaterials (NIMs). A direct consequence of negative refractive index is negative refraction, a phenomenon expected to be achieved through so-called left-handed metamaterials. Since the first emergence of these pioneering papers, there were objections to the physical possibility of a negative index [12]. Following the controversy, the underlying theoretical mechanism of negative refraction was established, [13], [14], and experimental evidence of negative refraction arising from a negative index at microwave frequencies demonstrated it [15]–[17].

1.3. Chapters Outline

This dissertation focuses on studying fundamental aspects of metamaterials and exploring some of their applications. To characterize metamaterials in order to modify and correct the initial designs, we need valid techniques to calculate effective parameters of the bulk metamaterial. In Chapter 2, a retrieval method is reviewed and based on it a numerical algorithm is developed to extract permittivity and permeability. We introduce our proposed mirrored S-resonator metamaterial and characterize its bulk properties numerically. We demonstrate that this design has an overlapping negative permittivity and permeability resulting in a negative index metamaterial. Moreover, we computationally study the interaction of the metamaterial with the incident field in the time domain. Finally, a planar metamaterial consisting of closed rings is proposed and characterized. The connection between the negative index and negative refraction is explained in Chapter 3. Simulations suggest that the negative refraction seen in a prism made out of mirrored S-resonators is a consequence of negative index, and is distinguishable from Bragg-like diffraction effects. In Chapter 4, we modify the design to address some concerns for using metamaterials such as bandwidth and polarization sensitivity. A meta-substrate can offer a route toward bandwidth engineering in metamaterials. Also, a polarization-insensitive design is introduced, and it is argued that it is a potential candidate for rapid prototyping by 3D printing. In Chapter 5 and 6, we investigate the imaging applications of the metamaterial. Near-field imaging and transfer of evanescent waves are presented in Chapter 5, while the possible far-field imaging through reciprocity is discussed in Chapter 6. We then explore the sensing properties of the metamaterial in Chapter 7. It is shown that the metamaterial can be used as a passive remote sensor, either intensity-based or frequency-based. Chapter 8 is about nonlinear phenomena in metamaterials, particularly Two-Photon Absorption (TPA). We numerically develop a tool to calculate the effect of TPA in designing nanostructure metamaterials. Finally, in appendices, samples of algorithms for retrieval procedure of effective parameters of metamaterials and TPA calculations in nonlinear materials are presented.

CHAPTER 2: DESIGNING METAMATERIALS

To design a left-handed metamaterial, electric and magnetic resonances are required to exist in the structure; conventionally a conductive split ring is used in designs to produce a magnetic response and a rod for its electrical characteristics. However, some proposed inclusions rely only on a single geometry to deliver a negative permittivity and negative permeability response. It has been shown that a meandering wire or S-shaped resonator exhibits an overlapping negative effective ε and μ over a significant broad range of frequencies [18]. We use this geometry of S-shaped resonators to realize most of the bulk metamaterial structures presented in this dissertation.

2.1. Effective Parameter Retrieval Method

In 1904, J. Maxwell Garnett proposed an effective media theory to originally describe dilute suspensions of small homogeneous spheres embedded in a host medium [19]. Later on, Bruggeman presented an approximate method to predict optical properties of composite materials [20]. These completely phenomenological models seem to work quite well even for spheres that are not very small on the scale of the wavelength and so the filling factor, f, is larger than expected. Although these theories can be applied to metamaterials, the question is how well they perform in highly dispersive regimes where concepts such as group or energy velocity cannot be easily defined. This question is reinforced by the difficulties experienced when trying to extract averaged bulk properties like refractive index from scattering parameters.

The Maxwell-Garnett approximation, for example, gives an estimate for the bulk permittivity, ε_{MG},

$$\frac{\varepsilon_{MG} - \varepsilon_2}{\varepsilon_{MG} + 2\varepsilon_2} = f\frac{\varepsilon_1 - \varepsilon_2}{\varepsilon_1 + 2\varepsilon_2} \tag{2.1}$$

where f is a simple volume filling factor between two already averaged descriptions of media, ε_1 and ε_2. The model implies that the microstructure of the medium can be neglected or completely averaged away. This, in turn, requires the inclusions to be relatively weakly scattering or far from resonance or strongly coupled together enough that there is a delocalized response. A typical rule of thumb for use of such a medium model is that there are about 6 or more inclusions (meta-atoms) per wavelength and that they do not interact with each other.

Obviously, as the inclusions or meta-atoms increase in size and material periodicities become of the order of the wavelength in scale, then diffraction effects begin to dominate. For random arrays, an effective medium model might well still describe the effective permittivity quite well if the permittivity contrast is not too high and the spheres are located apart enough. For higher filling factors, multipolar effects come into play and need to be taken into account. In other words, a mix of multiple responses due to local structures coupling together will lead to errors in the predicted ε_{MG}.

Metamaterials are composite materials, and effective medium theories are required to anticipate their constitutive properties. One of the most successful methods to achieve this goal is the simple Nicholson-Ross-Weir (NRW) extraction procedure [21] which is based on measurement of relative transmitted and reflected powers to calculate effective parameters.

The NRW method contains the logarithm of a complex function which can include many complex branch ambiguities that each lead to unique effective parameters which yield the same value for the logarithm. When the material is homogenous, the NRW procedure correctly determines the primary branch. However, for inhomogeneous materials, the selected branch is not always the correct choice because of multiple reflections from discontinuities. Therefore, the assumption of homogeneity leads to inaccurate results in metamaterials. Although the building blocks of metamaterials are much smaller in size than the wavelengths of operation bandwidth, in the order of λ/6, they are still not small enough to satisfy a homogeneous medium condition; consequently modified NRW techniques are required to characterize the effective parameters of metamaterials [22]–[27].

The modified methods assume a thin enough sample of metamaterial compared to the wavelength of incident field to tackle the homogeneity issue. Another obstacle is the rapid variation of parameter values near resonances which prevents estimation of the electrical thickness of the sample [28]. Also when the reflection and transmitted powers are very small in magnitude, the retrieval process might fail to predict the effective parameters [22].

Above all, some metamaterials are severely inhomogeneous, and only Lorentz and Drude dispersion models can be applied to characterize such materials [29].

We review a well-known retrieval method proposed by Chen et al. [23] which has the advantage of being tailored and originally tested on the S-shaped resonators. This method is based on NRW procedure as mentioned before where reflection and transmission data is measured to calculate the effective parameters. For a normal incident plane wave on a slab of thickness d, where the thickness is measured from the first face of the slab, reflection coefficient represents S_{11}, and S_{21} is obtained from transmission coefficient T by $S_{11} = Te^{ik_0 d}$where k_0 is the wave number of the incident field in free space. The S-parameters, refractive index n, and impedance Z are related by [21], [30],

$$\begin{aligned} S_{11} &= \frac{(Z-1/Z+1)\left(1-e^{i2nk_0d}\right)}{1-(Z-1/Z+1)^2 e^{i2nk_0d}} \\ S_{21} &= \frac{\left(1-(Z-1/Z+1)\right)e^{i2nk_0d}}{1-(Z-1/Z+1)^2 e^{i2nk_0d}} \end{aligned} \qquad (2.2)$$

Hence the refractive and index can be obtained from above equations,

$$Z = \pm\sqrt{\frac{(1+S_{11})^2 - S_{21}^2}{(1-S_{11})^2 - S_{21}^2}}$$

$$\begin{aligned} e^{ink_0d} &= \frac{1}{2S_{21}(1-S_{11}^2+S_{21}^2)} \pm i\sqrt{1\left(\frac{1}{2S_{21}(1-S_{11}^2+S_{21}^2)}\right)^2} \qquad (2.3) \\ &= \frac{S_{21}}{1-S_{11}\dfrac{Z-1}{Z+1}} \end{aligned}$$

to determine the signs in Equation (2.3), a passive metamaterial is assumed which requires $Z', n'' \geq 0$. The refractive index value can further be calculated from,

$$n = \frac{1}{k_0 d}\left\{\left[\left[\ln\left(e^{ink_0d}\right)\right]'' + 2m\pi\right] - i\left[\ln\left(e^{ink_0d}\right)\right]'\right\} \tag{2.4}$$

where m is an integer representing the branch of n' as the real part of the index is calculated by logarithm function producing infinite number of branches for all possible correct values in Equation (2.4). Possible perturbations of S_{11} and S_{21} values produced in numerical calculations or from experimental measurement might change sign of Z' and n'' when they are near zero. To avoid this sign ambiguity, once the impedance Z is obtained, the refractive index can be determined by,

$$e^{ink_0d} = \frac{S_{21}}{1 - S_{11}\frac{Z-1}{Z+1}} \tag{2.5}$$

To solve the sign ambiguity in n', or in other words to find the correct branch of above logarithm function, the method follows the suggestion that dispersive permittivity and permeability are continuous function of frequency for a slab of small thickness with respect to the wavelength [24], [28], [31]. It needs a careful approach particularly at resonant frequencies producing discontinuities in extracted parameters. To determine the branch of n' at the initial frequency, we first consider,

$$\begin{gathered} \mu'' = n'Z'' + n''Z' \\ \varepsilon = \frac{1}{|Z|^2}\left(-n'Z'' + n''Z'\right) \end{gathered} \tag{2.6}$$

the conditions for a passive medium $\mu'', \varepsilon'' \geq 0$ enforce,

$$\left|n'Z''\right| \leq n''Z' \tag{2.7}$$

that indicates when $n''Z'$ is near zero while Z'' is not, n' has to be near zero. At the initial frequency and then all subsequent frequencies, one has to find the correct branch integer m which satisfies Equation (2.7). There might be frequency regions where the chosen branch number does not satisfy Equation (2.7), it has been believed the reason is behind presence of multiple modes causing the n' becoming large, and the effective wavelength being in the order of the physical size of the unit cell thereby invalidating the assumption of small meta-atoms compared to the effective wavelength [32]–[34].

It was mentioned that metamaterials are not homogenous, so the retrieval method aims to find the exact position of slab faces to determine its thickness and provide an effective homogenized description. When the plane wave is incident on metal parts of a metamaterial, induced currents produce a scattered field which changes the uniformity of total field. Therefore, the first boundary of slab thickness is located where the reflected wave is still like a plane wave. If the material were homogenous, the retrieval process would deliver same values by increasing the slab thickness. Using this fact, metamaterial slab thickness can increase by its unit cell thickness in the propagation direction of incident wave to help us characterize the effective boundaries of slab thickness. Since reflection S_{11} depends on the location of the fist boundary, impedance also depends on its location as the impedance is related to S_{11}. In their paper, authors suggest an optimization model to match impedance for different number of metamaterial unit cells to determine the first boundary and the slab thickness [23]. It was concluded that the first boundary and the thickness are equal to the first boundary of the unit cell and its thickness.

We find that this parameter extraction method is successful in choosing the correct values for the wave impedance and the imaginary part of the refractive index from scattering parameters. However, it is unable to predict effective material parameters for some frequency regions once one enforces passive material conditions $Z^{"}, n^{"} \geq 0$. In addition, to determine n', an iterative process based on Taylor series is required which computationally can be a slow process.

The above parameter retrieval method and most similar techniques do not address the anisotropic nature of most metamaterials, and by assuming only a plane wave normally incident on the metamaterial, they ignore the requirement of using tensors to describe the electromagnetic properties of the bulk structure properly. Moreover, although efforts have been made to predict all elements of the effective permittivity and permeability tensors [35], still the results are valid only in the far-field, and the near-field behavior is ignored. An improved method introduced later in [36] suggests using Kramers-Kronig relations to determine the exact solution at each frequency.

The above procedure and most of the similar techniques assume an infinitely extended unit cell of metamaterial along the plane of incidence. By this assumption, the complexity of the problem arising from boundary conditions reduces, and ultimately a solid model can describe effective parameters of metamaterials. However, practical bulk metamaterials consist limited numbers of meta-atoms. Therefore, as finite size concept requires, we need to consider the boundaries of structure to evaluate its effective parameters. When a bulk metamaterial is not infinitely extended in at least one dimension, surface and spatial resonances can be significant which would affect effective parameters from the ones obtained from models for infinite metamaterials. Although these issues deviate finite size metamaterial properties from ideal models, researchers have tried to find similar models which estimate effective parameters when the structure has different sizes [37], [38].

2.2. S-resonators Background

One of the well-known resonator designs to build bulk metamaterials is a meandering wire or S-shaped resonator that would form a bianisotropic metamaterial structure when doubled with its mirrored image. By having the right dimensions for this resonator, one would be able to achieve overlapping negative permittivity and permeability bandwidth to obtain an effective negative and zero index bulk metamaterial [18], [39].

To analyze the S-shaped resonator, we should start from its simpler design of mirrored split ring resonator (SRR) which was proposed first in [40] to eliminate magnetoelectric couplings and hence its bulk bianisotropy characteristic of conventional split ring resonators. It was shown that when the resonator is in an electromagnetic field, the two capacitances C formed between the metallic arms allow an induced current to flow around the SRR, Figure 2.1(a).

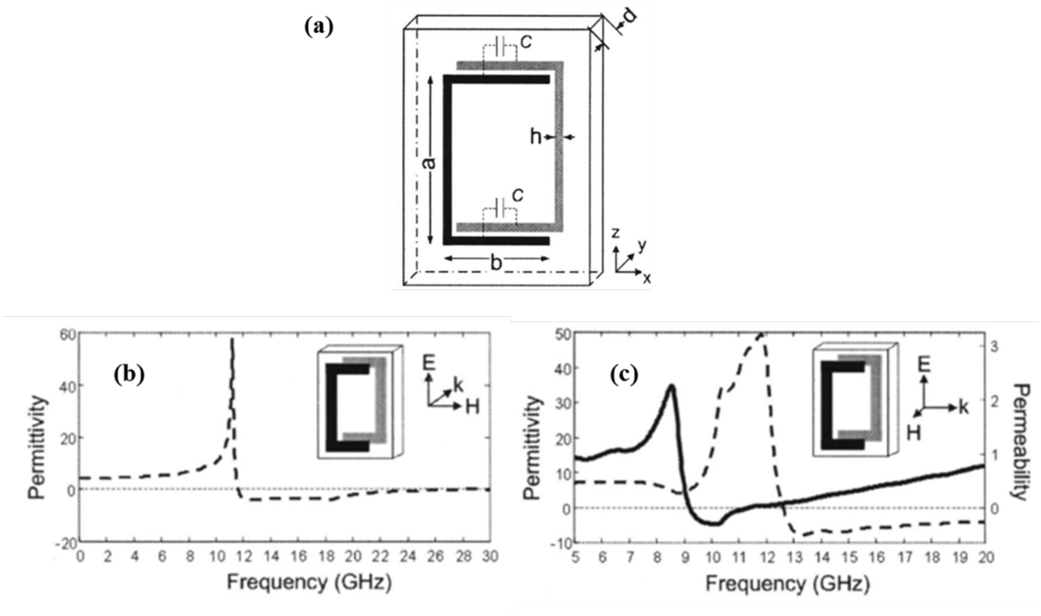

Figure 2.1: (a) Modified split ring resonator design as the initial step toward S-resonator design; (b) Real permittivity; (c) Real permittivity (dashed line) and real permeability (solid line). Incident wave vector and its polarization are shown in the inset. (figures are courtesy of [18])

Then authors proceed to calculate the effective permittivity ε_{eff} and permeability μ_{eff} using,

$$\varepsilon_{eff} = n/Z\,;\ \mu_{eff} = nZ \tag{2.8}$$

where n is the refractive index and Z is the wave impedance which each can be determined through a retrieval algorithm [23] based on the measurement of scattering parameters (S-parameters) which themselves are calculated from the reflection and transmission coefficients with the assumption of a normal incident wave on the metamaterial slab [28], [30]. Extracted effective parameters were reported as in Figure 2.1, which shows that only incident wave propagating along the x-direction demonstrates both negative effective ε and

μ, Figure 2.1(c), where the ε_{eff} is significantly dispersive around the magnetic resonance, and each of the two arms of SRR behaves as an electrical plasma medium. Although the electric resonant frequencies in Figure 2.1(b) and (c) are close to each other as expected, to induce a magnetic resonance, the incident wave must travel along the x-direction.

As depicted in Figure 2.1(c), the current SRR does not offer an overlapping negative permittivity ε_{eff} and permeability μ_{eff}. Therefore, by modifying the design, researchers increased the frequency of the magnetic resonance or decreased the electric resonant frequency to yield the desired overlapping negative bandwidth. The configuration of the mirrored S-resonator which was proposed in [18] is shown in Figure 2.2(a), where each resonator is printed as mirrored of each other on sides of the substrate. In addition to the two capacitances of former SRR, there is an additional capacitance C_1 between middle metallic strips. Considering calculated effective parameters for different orientation of S-resonator with respect to the incident field, they find an overlapping negative ε_{eff} and μ_{eff}, Figure 2.2(c), which suggests the presence of a negative refractive frequency bandwidth.

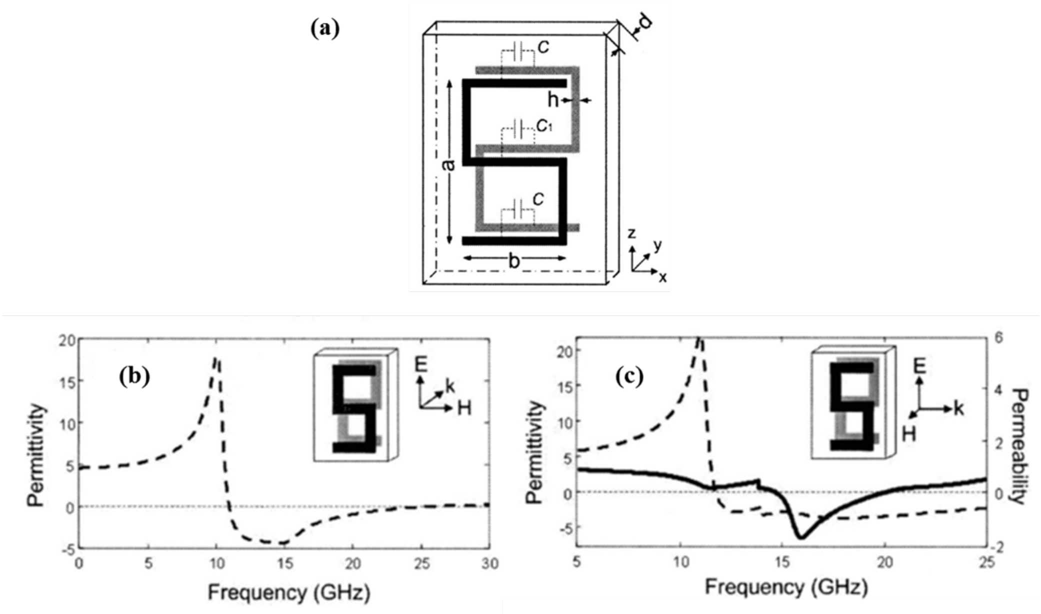

Figure 2.2: (a) S-resonator design; (b) Real permittivity; (c) Real permittivity (dashed line) and real permeability (solid line). Incident wave vector and its polarization are shown in the inset. (figures are courtesy of [18])

A theoretical framework which is formed on circuit model analysis can anticipate the resonant frequencies of S-resonator. The inductance of each loop is directly proportional to the area enclosed by each loop,

$$L = \mu_0 (b - 2h)\left(\frac{a - 3h}{2}\right) \approx \mu_0 \frac{ab}{2} \tag{2.9}$$

when the metal trace thickness h is very small considering loop dimension. Furthermore, magnetic resonant frequency can be calculated from circuit theory by assuming C_1=C,

$$\omega_{m0}^{(1)} = \sqrt{\frac{1}{(L/2)(2C/3)}} = \sqrt{\frac{3}{LC}} \tag{2.10}$$

The magnetic resonant frequency of Figure 2.1(a) can also be calculated as,

$$\omega_{m0}^{(2)} \approx \sqrt{\frac{1}{(2L)(C/2)}} = \sqrt{\frac{1}{LC}} \tag{2.11}$$

which means the resonance frequency of S-resonator is $\sqrt{3}$ times of SRR in Figure 2.1(a). Comparing numerical results in [18], the magnetic resonant frequency of simple SRR is $\omega_{m0}^{(2)}$=9 GHz, while for S-resonator it is $\omega_{m0}^{(1)}$=15 GHz which is $\approx 9\sqrt{3}$ and follows what as circuit analysis suggests.

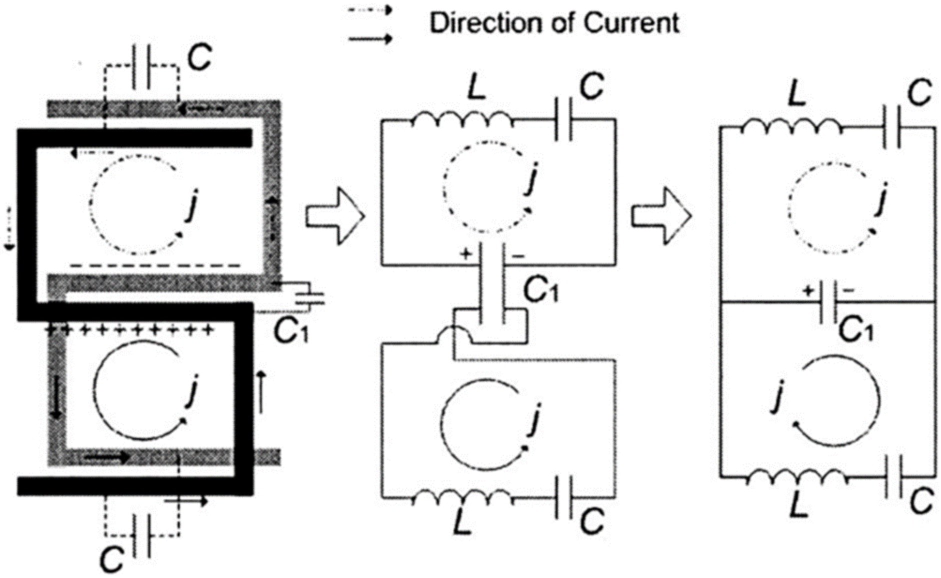

Figure 2.3: Equivalent circuit for S-resonator, where the capacitance C1 allows the current to flow in each loop in the presence of an external EM field. (figure is courtesy of [18])

For the electrical properties, when the S-resonator is in an external time-varying field, its two opposite metallic arms behave like a plasma medium and display the same electric properties as of SRR. However, the extra lengths of metal in S-resonator cause an additional inductance resulting in a decrease in the overall plasma frequency [41].

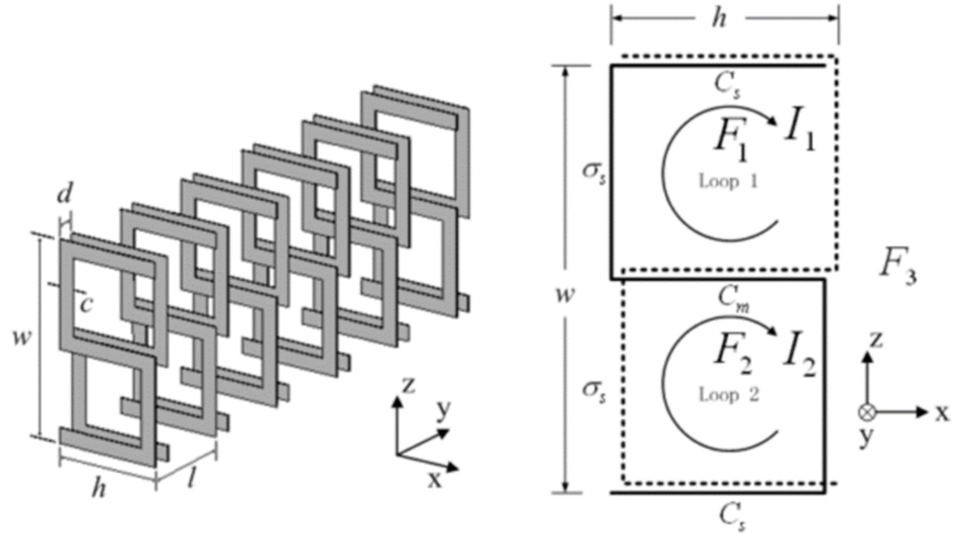

Figure 2.4: An array of S-resonators (left). A unit cell of S-resonator with dimension (right). (figures are courtesy of [42])

Kong *et al.* presented a more comprehensive analytical examination of the S-shaped resonators in [42]. They began by defining the fractional volume of the mirrored S-resonator as F1 for the top loop, F2 for the bottom loop, and F3 for the partial volume between the loops and in the middle. One can write a generalized form of these terms based on their definition as,

$$F_1 + F_2 + F_3 = 1 \tag{2.12}$$

In the presence of an external time-varying field, H_0, which oscillates along the y-direction, the induced currents would flow in the loops and they would be represented by I_1 and I_2 for top and bottom loop respectively. When the S-resonators are closed enough in an array, the magnetic fields in each three volumes of the S-resonator should satisfy,

$$\begin{gathered} H_1 - H_2 = j_1 - j_2 \\ H_1 - H_3 = j_1 \\ H_1F_1 + H_2F_2 + H_3F_3 = H_0 \end{gathered} \tag{2.13}$$

where,

$$j_1 = \frac{I_1}{l}\ ;\ j_2 = \frac{I_2}{l} \tag{2.14}$$

with l as the lateral lattice constant of the bulk structure along the y-direction.

From Equation (2.13), the fields in each volume can be calculated as,

$$\begin{gathered} H_1 = H_0 + (1 - F_1)j_1 - F_2j_2 \\ H_2 = H_0 + (1 - F_2)j_2 - F_1j_1 \\ H_3 = H_0 - F_1j_1 - F_2j_2 \end{gathered} \tag{2.15}$$

It is shown that the total electromotive force (emf) around each loop in a unit cell is derived as,

$$\begin{gathered} emf_1 = -\frac{\partial}{\partial t}(\mu_0 H_1 F_1 S) = \sigma_s I_1 + \frac{1}{C_s}\int I_1\,dt + \frac{1}{C_m}\int (I_1 + I_2)\,dt \\ emf_2 = -\frac{\partial}{\partial t}(\mu_0 H_2 F_2 S) = \sigma_s I_2 + \frac{1}{C_s}\int I_2\,dt + \frac{1}{C_m}\int (I_1 + I_2)\,dt \end{gathered} \tag{2.16}$$

where σ_s is the resistance from metallic traces in each loop, C_s is the capacitance between center metallic arms, C_m and is the capacitance of the top and bottom arms, Figure 2.4.

The capacitances can be calculated as,

$$C_s = C_m = \varepsilon_0 \frac{hc}{d} + \varepsilon_0 \frac{hc}{l-d} \tag{2.17}$$

by replacing $\frac{\partial}{\partial t}$ by $-i\omega$ and $\int dt$ by $\frac{1}{-i\omega}$ and using Equation (2.15) we can write Equation (2.16) as,

$$\begin{aligned} i\omega\mu_0 H_1 F_1 S - \sigma_s j_1 l + \frac{j_1 l}{i\omega C_s} + \frac{(j_1 + j_2)l}{i\omega C_m} = 0 \\ i\omega\mu_0 H_2 F_2 S - \sigma_s j_2 l + \frac{j_2 l}{i\omega C_s} + \frac{(j_1 + j_2)l}{i\omega C_m} = 0 \end{aligned} \tag{2.18}$$

Using Equation (2.14), j_1 and j_2 can be calculated from Equation (2.16), and subsequently $\mu_{eff}$is obtained from [11] as,

$$\begin{aligned} \mu_{eff} &= \frac{B_{avg}}{\mu_0 H_3} = \frac{H_0}{H_0 - F_1 j_1 - F_2 j_2} \\ &= 1 - \frac{(\omega\mu_0 S)^2 F_1 F_2 (F_1 + F_2) - \mu_0 S\left[(F_1^2 + F_2^2)\frac{l}{C_S} + (F_1 - F_2)^2 \frac{l}{C_m}\right] + iA(\sigma)}{(\omega\mu_0 S)^2 F_1 F_2 - \mu_0 S (F_1 + F_2)\left(\frac{l}{C_S} + \frac{l}{C_m}\right) + \frac{1}{\omega^2}\frac{l}{C_S}\left(\frac{l}{C_S} + \frac{2l}{C_m}\right) - B(\sigma) + iC(\sigma)} \end{aligned} \tag{2.19}$$

where,

$$\begin{aligned} A(\sigma) &= \omega\mu_0 S (F_1^2 + F_2^2)\sigma_s l \\ B(\sigma) &= (\sigma_s l)^2 \\ C(\sigma) &= \left[\omega\mu_0 S (F_1 + F_2) - \frac{2}{\omega}\left(\frac{l}{C_S} + \frac{l}{C_m}\right)\right]\sigma_s l \end{aligned} \tag{2.20}$$

In our work, the S-resonator design has symmetrical loops, $F_1 = F_2 = F$, therefore μ_{eff} is derived as,

$$\mu_{eff} = 1 - \frac{2F + i\,A(\sigma)/X}{1 - \dfrac{1}{\omega^2 \mu_0 FS\left(\dfrac{l}{C_S} + \dfrac{2L}{C_m}\right) - B(\sigma)/X + i\,C(\sigma)/X}} \tag{2.21}$$

where,

$$X = (\omega\mu_0 FS)^2\left(1 - \frac{1}{\omega\mu_0 FS}\frac{l}{C_s}\right) \tag{2.22}$$

Moreover, the magnetic resonance frequency is given by,

$$\omega_{m0} = \sqrt{\frac{1}{\mu_0 FS}\left(\frac{l}{C_s} + \frac{2l}{C_m}\right)} \tag{2.23}$$

also, the magnetic plasma frequency is determined by,

$$\omega_{mp} = \sqrt{\frac{1}{\mu_0 FS(1-2F)}\left(\frac{l}{C_s} + \frac{2l}{C_m}\right)} = \omega_{m0}\sqrt{\frac{1}{1-2F}} \tag{2.24}$$

Now circuit theory can simplify the above equation by assigning an inductance L to each loop of the S-resonator. Therefore the Equation (2.24) is written as,

$$\omega_{mp} = \sqrt{L\frac{1}{\dfrac{1}{C_s} + \dfrac{1}{C_m/2}}} = \sqrt{\frac{l}{\mu_0 FS}\left(\frac{1}{C_s} + \frac{2}{C_m}\right)} \tag{2.25}$$

which is the same as calculated ω_{m0}.

The electrical characteristics of S-resonators are very similar to a metallic wire medium described in [10] which itself is driven by the Drude model, and the general form of its effective permittivity is shown to be,

$$\varepsilon_{eff} = 1 - \frac{\omega_{ep}^2 - \omega_{e0}^2}{\omega^2 - \omega_{e0}^2 + i\gamma\omega} \tag{2.26}$$

where ω_{e0} is the electric resonant frequency, ω_{e0} is the plasma frequency, and γ is the damping coefficient representing dissipation of energy in free electron plasma.

The electric resonant frequency of the S-resonator is lower than that of wire medium, and the reason is due to the larger capacitance in the S-resonator [42]. This offers a tool to modify the electric resonance of the S-resonator to achieve an overlapping negative effective permittivity and permeability.

We need to mention that these analytical expressions are for a unit cell of S-resonators along the z-direction, and by adding more meta-atoms, the analytical approach becomes extremely difficult and complicated. Therefore, in addition to numerical and theoretical approaches toward confirmation of the negative refractive index, Kong and colleagues investigated their proposed metamaterial design through experiments to verify this double negative feature of the bulk structure [18]. According to their experiments, a prism was fabricated to examine Snell's law of refraction, Figure 2.5.

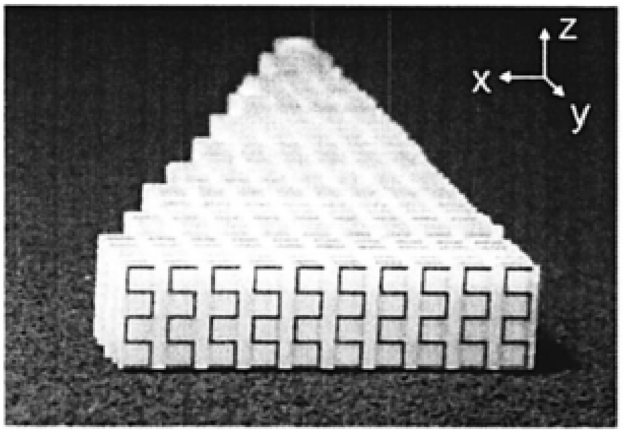

Figure 2.5: A prism made from S-resonators. (figure is courtesy of [18])

They measured the angle of transmitted power from the normal axis on the exit face of the prism and bu using the Snell's law they could estimate the bulk effective refractive index. Their experiments confirmed a negative refraction from the S-shaped resonator bulk structure over a frequency range which was different than what obtained from numerical calculations, Figure 2.6. The reason was due to a higher dielectric substrate and the connected S-resonators which both decreased the electric resonant frequency and altered the magnetic resonant frequency, but the qualitative behavior stayed unchanged, so they were still able to observe a negative refraction.

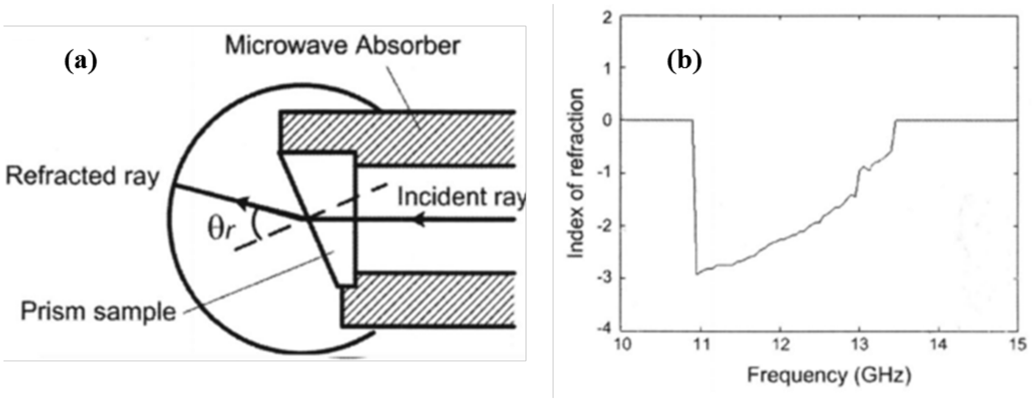

Figure 2.6: (a) Schematic of setup for Snell refraction experiment. (b) Refractive index obtained from the angle of measured power in the far field from prism's exit face. (figures are courtesy of [18])

2.3. Studying Designed S-resonators

Based on all the previous arguments, we choose the S-shaped resonators as the main meta-atom from which to build meta-structures. This motivation clearly comes from its already established analytical and experimental approaches to achieve a double negative metamaterial. The S-shaped resonator was studied before in our group for different configurations, [43]. It was shown that a mirrored S-shaped resonator metamaterial exhibits overlapping negative permittivity and permeability. Figure 2.7 illustrates the mirrored S-shaped resonator which we designed for this purpose and is embedded in its dielectric host. In experiments, the S-resonators are printed on either side of FR4 circuit boards, and plain boards are inserted between printed ones. For the sake of simulations, we can assume metal S-resonators are embedded in a dialectic hot which has FR4 properties.

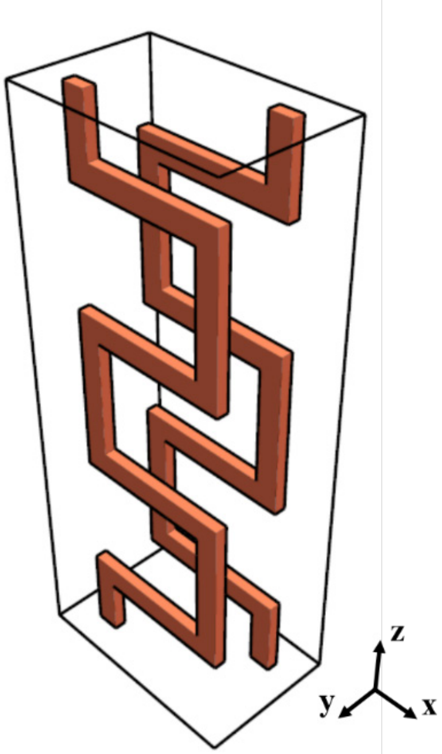

Figure 2.7: Schematic of a part of the mirrored S-resonator metamaterial. In simulations of effective parameters extraction, there are an infinite array of these resonators along the z-direction and the y-direction. The exciting plane wave is propagating along the x-direction with polarization along the z-direction.

In Figure 2.8, the dimensions of the unit cell are Dx=6.4mm, Dy=7.68, and Dz=3.28mm; and for the metal strips we have h=3.2mm, w=3.84mm, tw=0.64mm, with a lateral separation of mirrored S-resonators as d=1.6mm in the y-direction, and their trace thickness is 38µm. Metal strips are made out of copper, and the dielectric substrate of FR4 has a permittivity ε of 4.4 and loss tangent of 0.02.

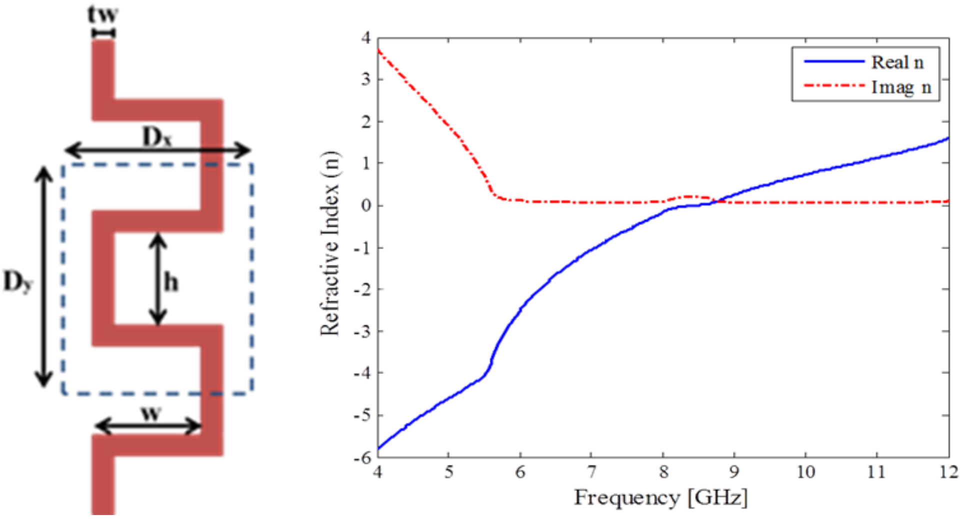

Figure 2.8: The meta-atom dimensions printed copper S-shaped resonators on the FR4 circuit board with ε=4.4 and loss tangent of 0.02, with h=3.2mm, w=3.84mm, tw=0.64mm, d=1.6mm, and trace thickness of 38μm. The unit cell dimensions are Dx=6.4mm, Dy=7.68, and Dz=3.28mm. On the right, the extracted refractive index for this design showing an unquestionable negative-index region for frequencies of 5.8-8GHz and near-zero index for 8.1-8.6GHz.

All the main simulations in this dissertation are conducted either in the frequency domain and finite element method (FEM) using Ansys HFSS or using finite-difference-time-domain (FDTD) method through available commercial software Lumerical FDTD. In numerical studies, a unit cell is assumed to be infinitely extended through enforcing periodic boundaries. Here, periodic boundaries are set for the XY and the XZ planes. The exciting plane wave is traveling along the z-direction with a polarization along the x-direction, Figure 2.9.

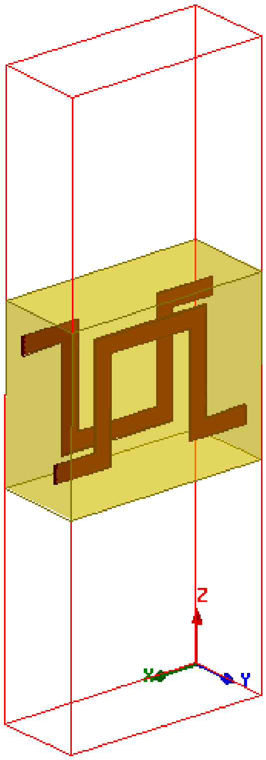

Figure 2.9: Simulation setup for calculating S-parameters of the S-resonators in HFSS. The unit cell is infinitely extended in the XY plane by enforcing periodic boundaries on the XZ and the YZ faces of the air box (red box) which encloses the unit cell. The excitation wave travels along the z-direction and with a polarization along the x-direction.

The S-parameters obtained for a single unit cell along the propagation direction is plotted in Figure 2.10 where S_{11} is related to reflection coefficient and S_{21} is related to transmission coefficient. In the plot for the S-parameters magnitude, Figure 2.10(left), there are two regions indicating separate resonances. We know that the first one which is at 6GHz belongs to a magnetic resonance produced in the loops made by the mirrored S-resonators and the second one which is at 9.1GHz comes from an electric resonance produced in the metal strips of the S-resonators. We can anticipate that the overlapping negative effective ε and μ would be between these two resonances.

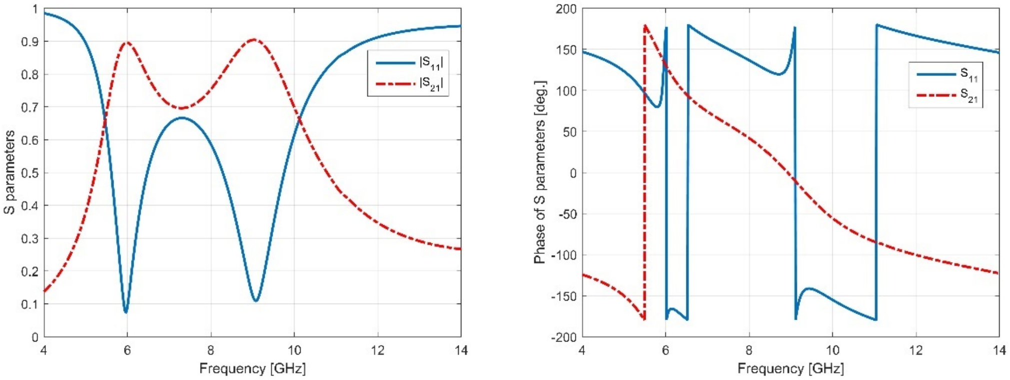

Figure 2.10: Magnitude of S-parameters (left), and their phase (right) for an infinitely extended S-resonator slab on the plane of incidence with a single unit cell along the propagation direction.

The impedance is extracted from S-parameters which itself also indicates the two dominant resonances of the metamaterial, Figure 2.11. In our representations, a positive real part of impedance and its negative imaginary part satisfy the requirement for a passive medium. Later in Chapter 4, we will discuss the design parameters to modify and tailor the effective resonance behavior of the S-resonator metamaterial.

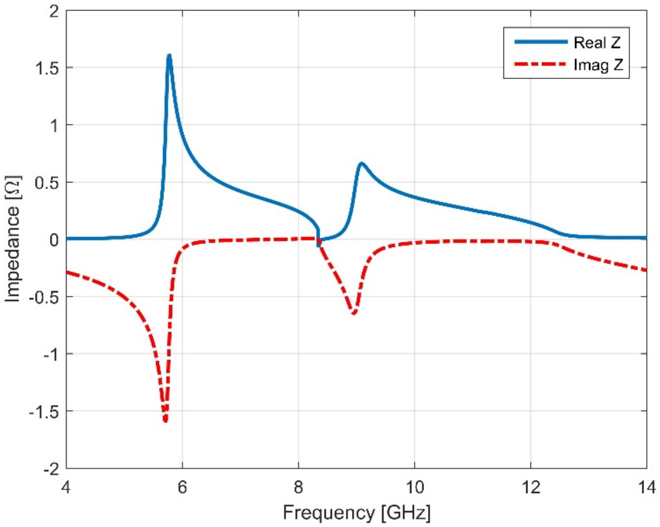

Figure 2.11: Impedance of an infinitely extended S-resonator slab on the plane of incidence with a single unit cell along the propagation direction.

After that, all possible branches which satisfy the logarithm function for refractive index, Equation(2.5), are calculated, and some are depicted in Figure 2.12.

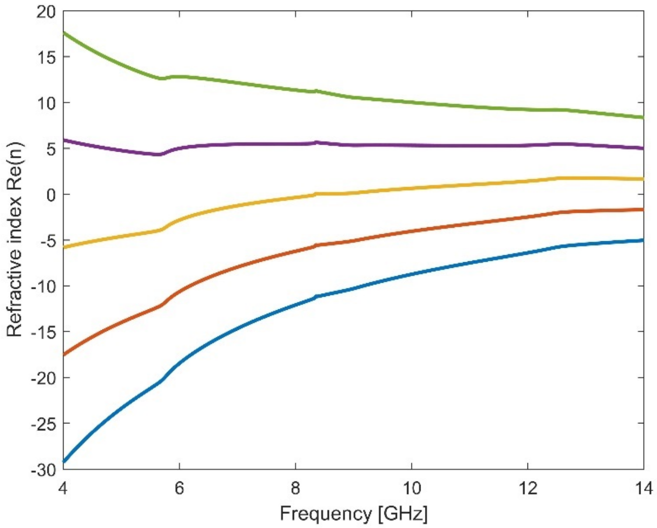

Figure 2.12: Some of the possible refractive index branches for its real part.

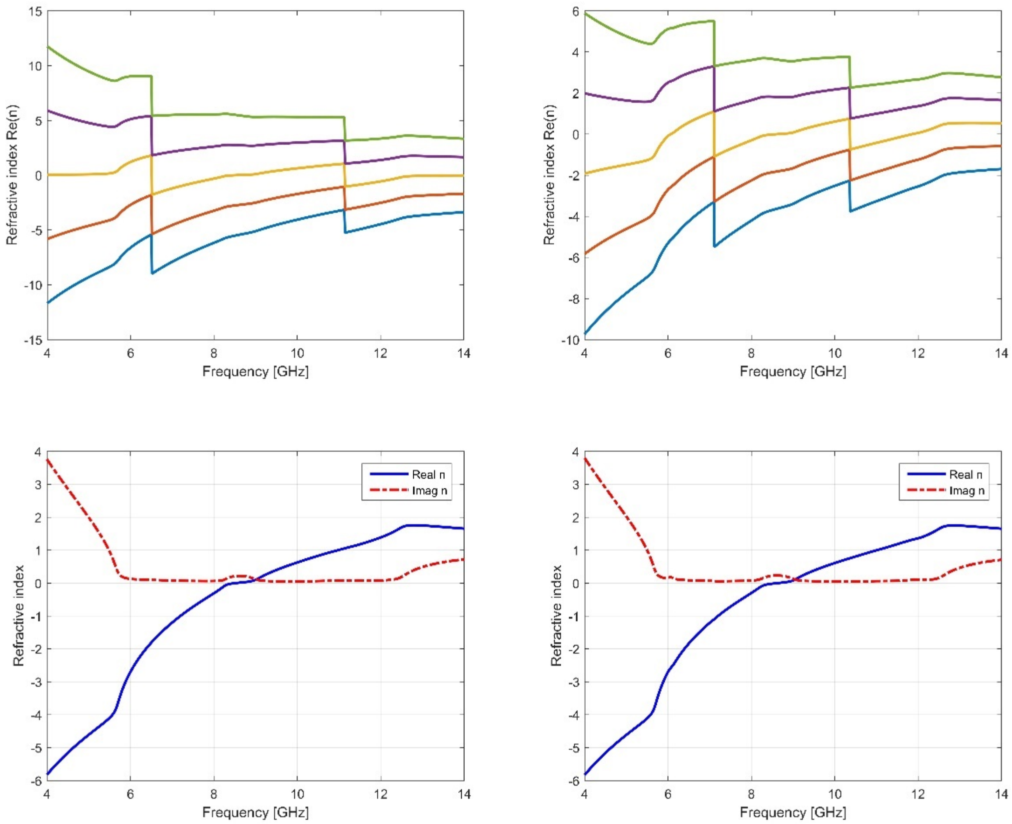

Figure 2.13: Some of the possible index branches for its real part (top), and extracted index after choosing the correct branch number (bottom). Two unit cells along the propagation direction (left), and three unit cells along the propagation direction (right).

Since choosing the correct branch number can be difficult, we use the fact that the refractive index should remain the same over frequencies by increasing the number of unit cells along the propagation direction as far as the slab thickness is thin enough compared to the effective wavelength within the slab. We then obtain the correct branch by comparing the generated index branches for different lengths of the metamaterial slab, Figure 2.13. The chosen branch number in each case produces the same initial index for all three different slab thicknesses. Moreover, following continuity condition, these choices generate the same refractive index. Therefore, the correct branch number is chosen, and the extracted refractive index of this single unit cell along the traveling wave is shown in Figure 2.14.

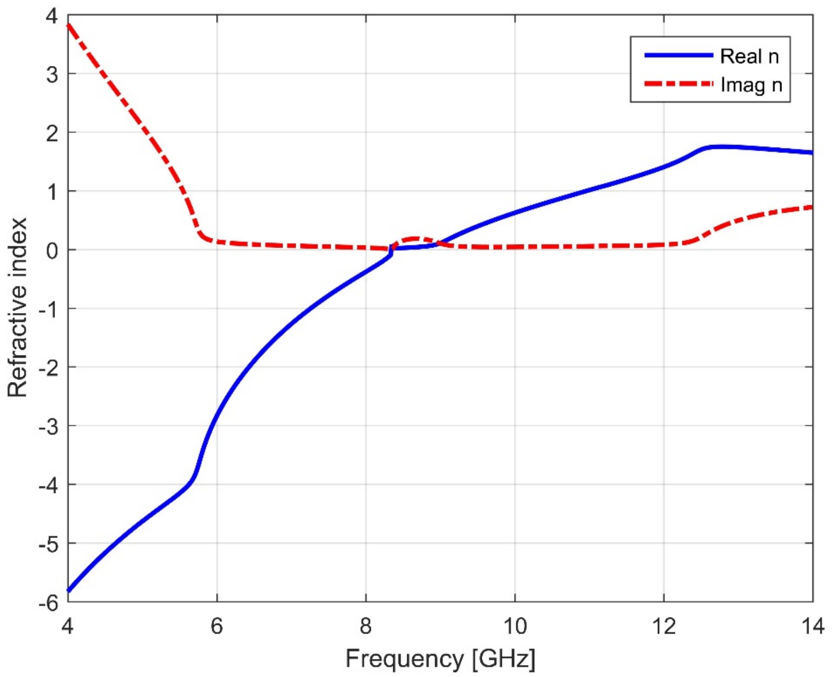

Figure 2.14: Extracted effective refractive index of the mirrored S-resonators with single unit cell along the propagation direction.

As can be seen in the above figure, there is a frequency region in which the real part of the refractive index is negative, indicating an overlapping of negative values of effective permittivity and permeability. The imaginary part of the index is very close to zero for a portion of this segment, and it increases for the rest of it. Based on conditions for extracting valid values for index based on resonances of the structure [23], the retrieval method can confirm only the regions where the loss, imaginary part of the index, is very low. The other areas with higher imaginary values are affiliated with large losses due to resonances, and the extraction method is unreliable to justify the physical meaning of the extracted index. Hence, we can accept the region in 5.8-8.1GHz as an unquestionable negative-index region. In other words, the mirrored S-resonator metamaterial has a negative refractive index with a frequency bandwidth of 2.3GHz. The relative size of meta-atoms compared to free space wavelength in this frequency range is between $\lambda/6$ and $\lambda/8$ which is small enough to be considered as a homogenous medium for parameter extraction purpose. In addition, the frequency range of 8.5-12.1GHz represents a valid positive index region. The area between 8.1-8.5GHz which is near zero with a higher loss than the vicinity areas is because of the logarithmic function behavior around zeros or singularities.

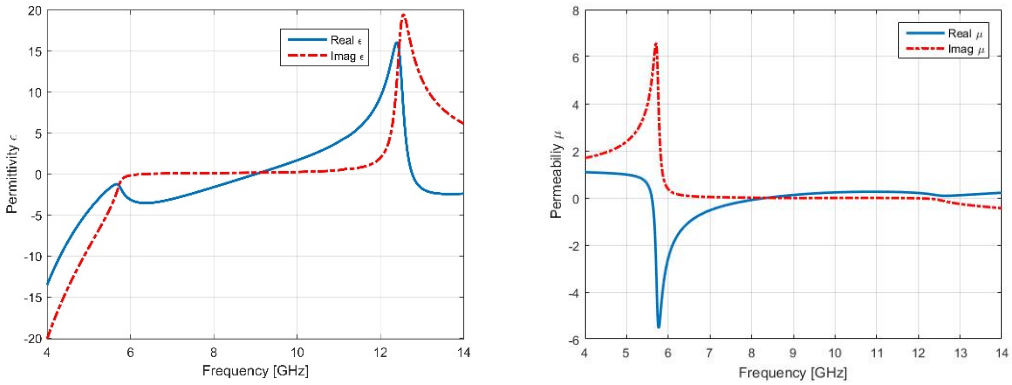

Figure 2.15: Effective permittivity (left), and effective permeability (right).

We can then extract the effective permittivity and permeability from the obtained index and impedance, Figure 2.15. It is clear that both ε_{eff} and μ_{eff} have a negative real part in the 5.8-8.1GHz frequency range with low positive imaginary values. Also, we can see corresponding electric and magnetic resonances in these figures.

Following the extraction method [23], the bulk properties of this metamaterial are determined from scattering parameters, and the retrieval method assumes an infinite array of meta-atoms in the plane perpendicular to the plane of incidence. The retrieved refractive index values are consistent with expectations. They do not arise from diffraction phenomena, and their dependence on the collective resonant properties of the metamaterial is evident [44].

There is an interest in tuning the S-resonators to control the frequency of operation. We know that metamaterials are very sensitive to environment change regarding their interaction with electromagnetic waves. For instance, by modifying the design of the meta-atom, we can achieve a shift in frequency respond of the structure. Figure 2.16 shows an example approach to change the effective refractive index of the bulk metamaterial by modifying its substrate.

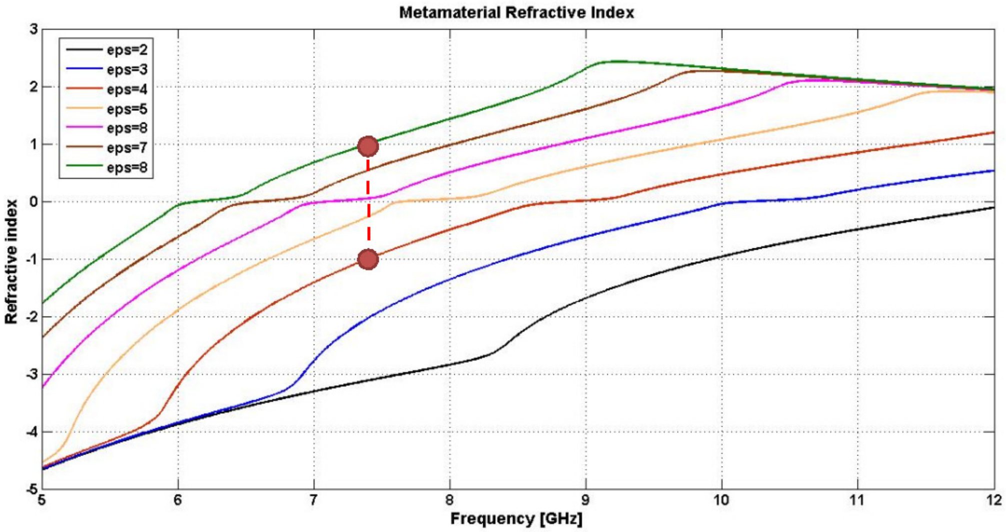

Figure 2.16: By changing permittivity of the S-resonator substrate, we can control the frequency of operation having the overall respond fixed. For instance, two permittivity of 4 and 8 results in effective refractive indices of +1 and -1.

We proceed our studies of the S-resonator metamaterial with investigating time evolution of the field in the presence of the metamaterial. Most of the numerical approaches are based on frequency domain evaluation of the metamaterials which eliminates the comprehensive understanding of resonances and couplings in meta-atoms as all the fields are calculated in steady state for each single frequency. Advantages of frequency domain methods such as finite element method (FEM) are i) more stable numerical results, and ii) fewer unknowns to solve for each mesh space and iteration, which saves the calculation time by increasing the simulation size and mesh. Therefore, they can be efficient and time-savings methods to study metamaterials especially when the bulk structure of interest is bigger than the wavelength in some orders of magnitude. On the other hand, exploring transient nature of interactions between incident field and the metamaterial structure can unravel the dynamic of the couplings between the incoming field and the resonators as well as energy distribution of the field over frequencies and how the presence of the strong resonators in the metamaterial structure would modify this energy distribution.

We conduct the time domain series of simulations in Lumerical FDTD which is a commercial package for FDTD simulations in optics and photonics and to some applications in RF and Microwave. The simulation environment is shown in Figure 2.17, where an infinitely extended metamaterial structure is built by enforcing periodic boundaries on the XY and the XZ planes. Two rows of mirrored S-resonators are designed along the propagation direction to consider stronger mutual couplings while the field travels through the structure. All dimensions for the unit cell is the same as for the simulations in HFSS except trace thickness which is doubled in FDTD simulations to 76nm to run the simulation with smaller amounts of meshing and eventually to save on simulation time since it should not change the final results significantly. The dielectric substrate is FR4 and has an index of 2.09772+i0.0209751 over the frequencies of interest. We set the YZ planes as PML boundaries to absorb the most optimum amount of incident field energy on these faces eliminating any potential numerical back reflection. Incident field is shown to propagate along the x-direction with polarization along the y-direction. Field monitors are placed in multiple positions, yellow crossed marks, to record time variation of the field at these points.

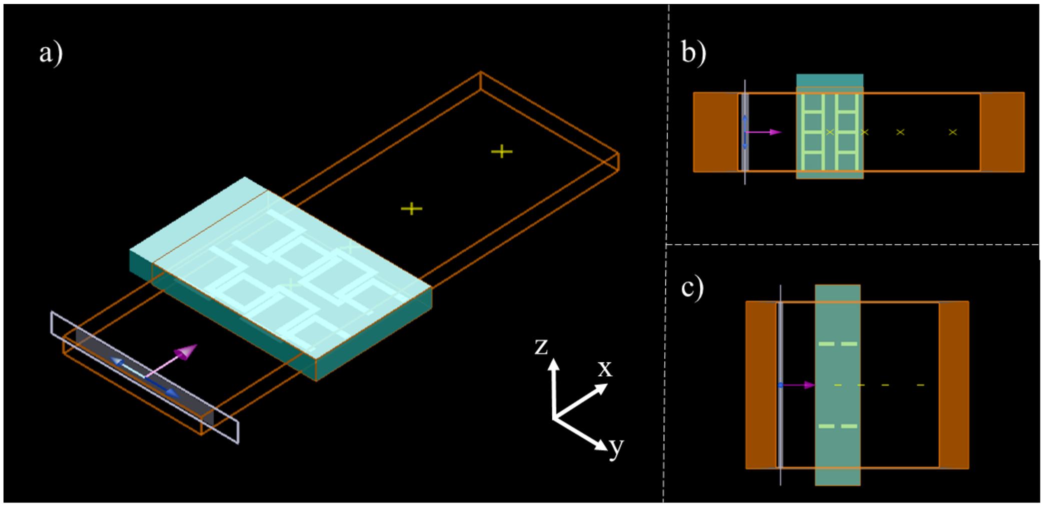

Figure 2.17: Simulation setup in Lumerical FDTD; a) two rows of mirrored S-resonators are embodied in the dielectric substrate. Periodic boundaries are applied on the XZ and XY planes, and the YZ planes are set as PML boundary. A purple arrow indicates the excitation field as its wave vector and blue vectors as the polarization of the field. The yellow crossed marks are the position of the field monitors; b) the XY view of the setup; c) the XZ view of the setup.

To excite the structure, a broadband pulse of 0.3ns time length with a bandwidth of 18.63GHz is injected in the simulation setup with signal properties shown in Figure 2.18. The incident field is a plane wave and its energy is distributed over frequencies of 0.7 to 19GHz which covers the main resonance frequencies of the mirrored S-resonators.

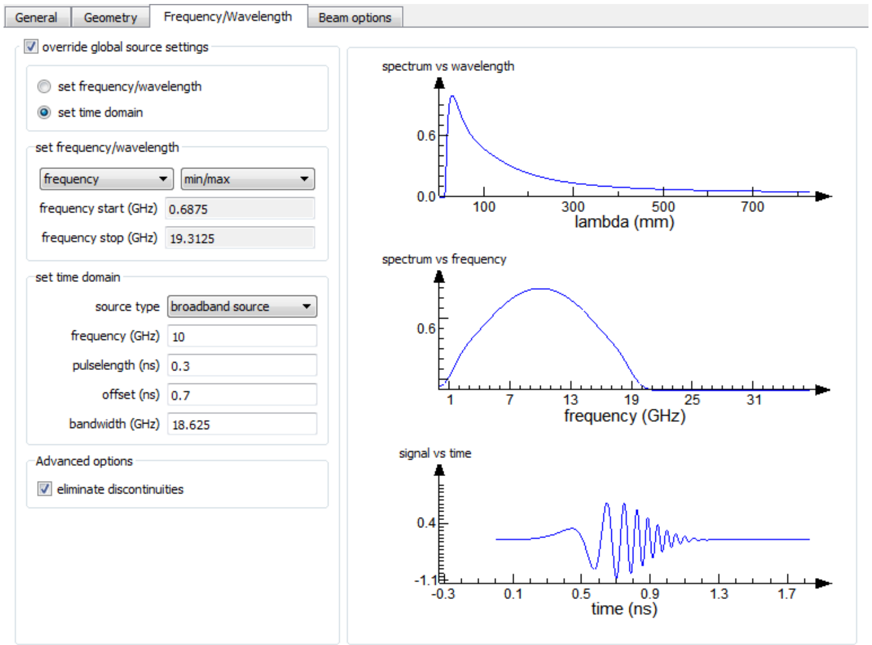

☑ override global source settings

○ set frequency/wavelength
● set time domain

set frequency/wavelength

frequency ▾ min/max ▾
frequency start (GHz) 0.6875
frequency stop (GHz) 19.3125

set time domain

source type broadband source ▾
frequency (GHz) 10
pulselength (ns) 0.3
offset (ns) 0.7
bandwidth (GHz) 18.625

Advanced options

☑ eliminate discontinuities

Figure 2.18: Excitation field setting window in Lumerical. Time signal, as well as frequency and wavelength spectra, are shown approximately based on input values.

Using this excitation pulse, we can study the resonances and dynamic of interaction between the field and the metamaterial, Figure 2.19. Comparing spectra of the case with the only FR4 substrate and its combination with mirrored S-resonators reveal the resonance frequencies of the structure. The significant loss in the latter comes from the strong couplings with free space field and its scattering off the metal strips.

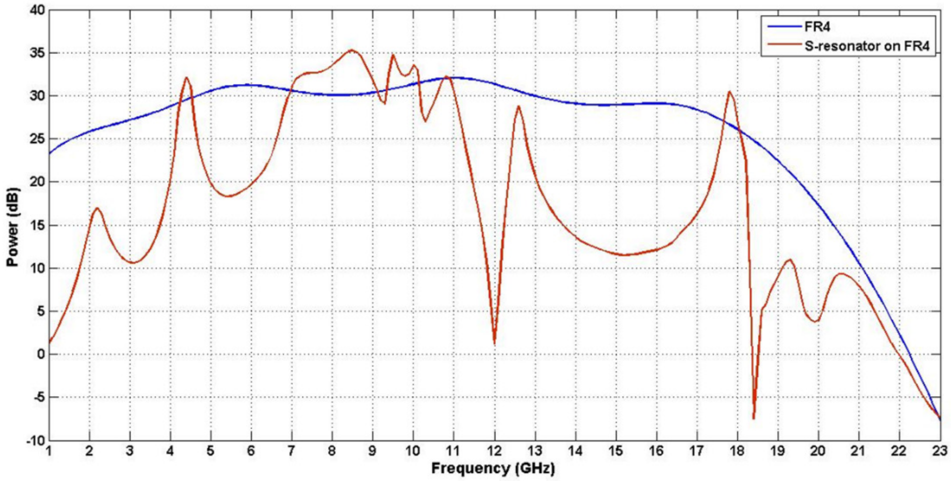

Figure 2.19: Field spectra measured at 0.2mm after slab when only FR4 substrate exists compared to the presence of metamaterial.

The above spectra demonstrate the resonant nature of the metamaterial and the possible energy coupling between frequencies. To better understand this energy coupling, we use narrower signal pulses with frequencies close to the resonant frequencies of the metamaterial. Figure 2.20 illustrates settings of a sample excitation pulse with central frequency at 8.5GHz. A single frequency field means an infinite time signal, but we only need a small amount of field time length to run the simulation optimally. By taking into account the requirement of having convergent simulation results, the simulation runs for 20ns while the plane wave travels through the structure. Although settings are for single frequency excitation signals, in practice the software is generating a very narrow bandwidth signal which is sufficiently narrow for this purpose.

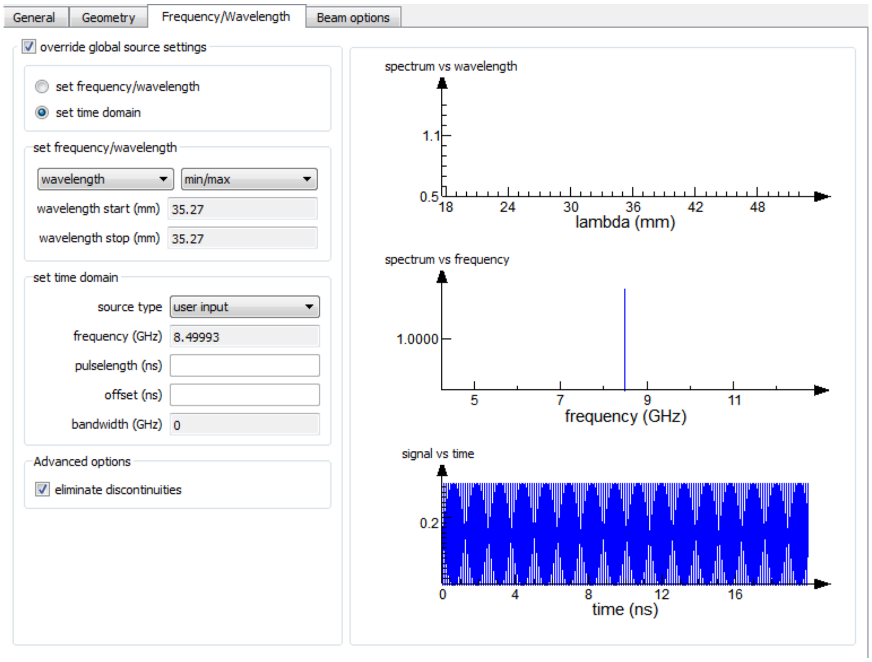

☑ override global source settings

○ set frequency/wavelength
● set time domain

set frequency/wavelength
wavelength | min/max
wavelength start (mm) 35.27
wavelength stop (mm) 35.27

set time domain
source type user input
frequency (GHz) 8.49993
pulselength (ns)
offset (ns)
bandwidth (GHz) 0

Advanced options
☑ eliminate discontinuities

Figure 2.20: A narrow bandwidth plane wave is used to excite the metamaterial. Although numerically we can set the source to have a single frequency wave with infinite time length, in practice there is a time length and therefore a narrow frequency bandwidth.

The transmitted field right after the slab, 0.2mm after the exit face, is recorded by a point field monitor and the results are shown in Figure 2.21. They indicate that there should be more frequency components in the first 2ns of the field evaluation, and after 4.5 ns, the field reaches its maximum value and is stable after that. To analyze the frequency content of this time signal, we use Fourier Transform analysis in MATLAB to obtain the frequency spectra of the field. In Figure 2.22, we can see the transmitted spectra of different excitation frequencies for only substrate slab and the metamaterial slab.

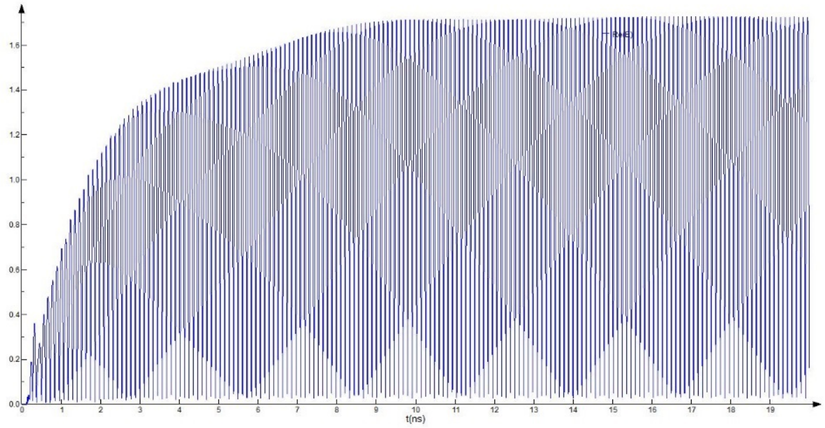

Figure 2.21: The E-field magnitude of the transmitted wave through the metamaterial slab which shows there should be more frequency components in the first 2ns of the field evaluation, and after 4.5 ns, the field reaches its maximum value and is stable after that.

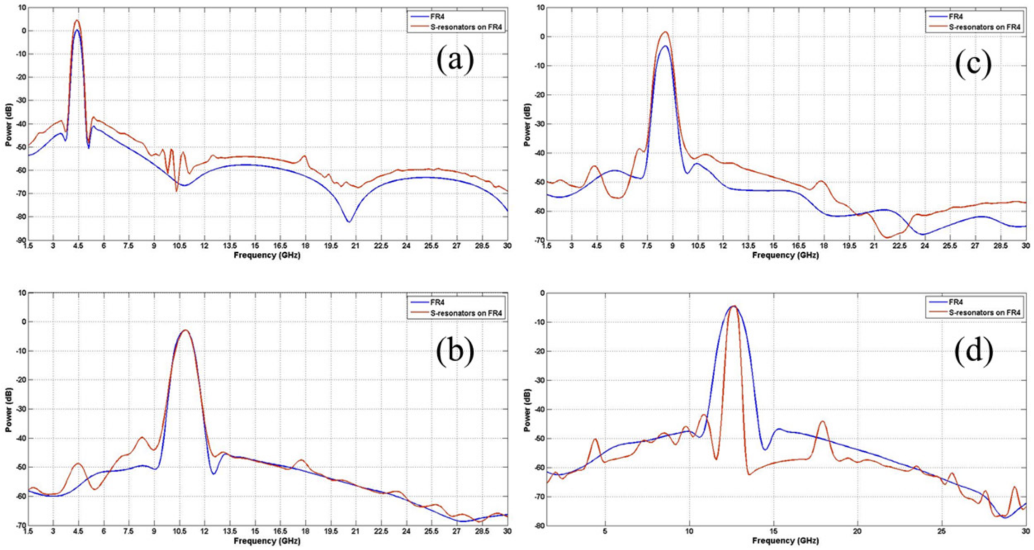

Figure 2.22: Transmitted frequency spectra of multiple excitation frequencies for the substrate slab and the metamaterial slab; excitation frequencies a) 4.4GHz, b) 8.5GHz, c) 10.8GHz, d) 12.6GHz.

As illustrated in Figure 2.22, all single frequency excitations are broadened in contrast to the theoretical excitation settings in the software, and this bandwidth is between 0.5 to

2GHz where for an excitation frequency of 4.4GHz, Figure 2.22(a), it has the lowest bandwidth of about 0.5GHz. Another interesting fact in the bandwidth analysis is that although most of the transmitted bandwidth after the substrate slab and the metamaterial slab are comparable, at the higher excitation frequency of 12.6GHz, the frequency bandwidth is decreased by about 40% when S-resonators are present in the simulation. This suggests that the metamaterial acts as a very effective bandpass filter while the peak output power has remained almost the same.

By further studying these power spectra, Figure 2.22, we observe the presence of the dominant resonant frequencies of the metamaterial which were shown before in Figure 2.19 using a broadband excitation. For instance, the peak resonant frequency of 4.4GHz has significant power even when the excitation signal is at higher frequencies. Although a portion of the measured power at this peak can be associated with the signal power, the proportion increase is noticeable enough to assume that a part of power comes from the coupling of the signal frequency at higher resonant frequencies to other resonant frequencies. This mechanism can be explained as power coupling of the fundamental resonances in the resonator while one of the resonances is excited. On the other hand, these spectra only demonstrate the distributed power as average power over the entire sampled time which is 20ns in these simulations. Therefore, a spectrographic analysis can show the time evaluation of these spectra densities with a better explanation, Figure 2.23.

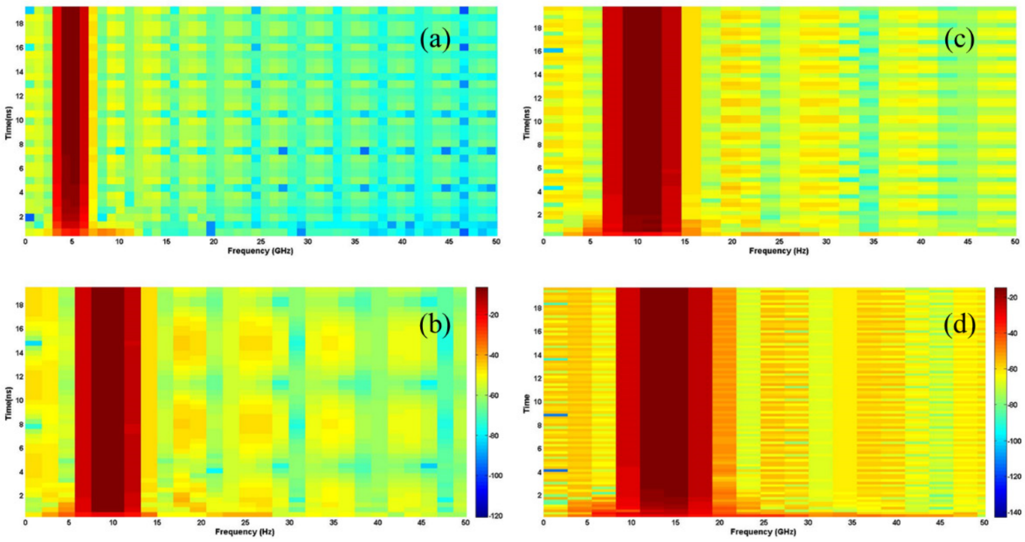

Figure 2.23: Spectrograph of transmitted frequency spectra of multiple excitation frequencies for the metamaterial slab; excitation frequencies a) 4.4GHz, b) 8.5GHz, c) 10.8GHz, d) 12.6GHz.

As illustrated in the above figures, some of the signal power is distributed over adjacent frequencies in the first 2ns of time evaluation, and then power remains within the central frequency bandwidth for the rest of time evaluation, while the coupled power to nearby frequencies dissipates away. The nature of these coupled fields is evanescent as they are not propagating energy toward the far field.

2.4. Designing Metasurfaces

There is a version of metamaterials that are extended only on the surface and are called metasurface. These 2D structures are similar to frequency selective surfaces (FSSs), but their unit cells and spacing are on the subwavelength scale. Early works on these structures called them metafilms referring to the distribution of electrically small resonators on a surface with negligible thickness [45], [46]. To characterize their electromagnetic behavior, one can assign surface electric and magnetic polarizability to these scatterers. Compared to bulk metamaterials, metasurfaces occupy less space and offer a very compact design while delivering superior results. Their electrically small size means they have significantly less loss compared to 3D metamaterials, so they can be better candidates for applications where bulky metamaterial's loss is a major drawback.

Planar metamaterials have attracted great attentions due to their unique functionalities for various applications such as cloaking [47], [48], magnetic mirror [49], and many more [50]. Conventionally, these planar metamaterials have been designed as periodically arranged resonators with many different geometries proposed by their unit cell. By breaking spatial symmetry in the design of resonators, trapped modes could couple strongly to free space excitation which results in Fano resonances and electromagnetically induced transparency (EIT) phenomena [51]. In particular, double concentric rings were shown to exhibit polarization and angle independent resonance transmission frequency with a narrow band-pass [52]. We numerically study the role of asymmetries introduced in concentric rings, resulting in additional Fano resonances, and therefore finding applications in spectral filtering devices and sensors.

In Figure 2.24(a), the layout of concentric and non-concentric rings are shown. The rings are perfect electrical conductors of inner and outer radii of 4.3mm and 5.25mm respectively with a trace width of 0.4mm, and they are enclosed in a 15mm by 15mm unit cell. The structure is excited using a plane wave which propagates along the z-axis and has linear polarization along the y-axis.

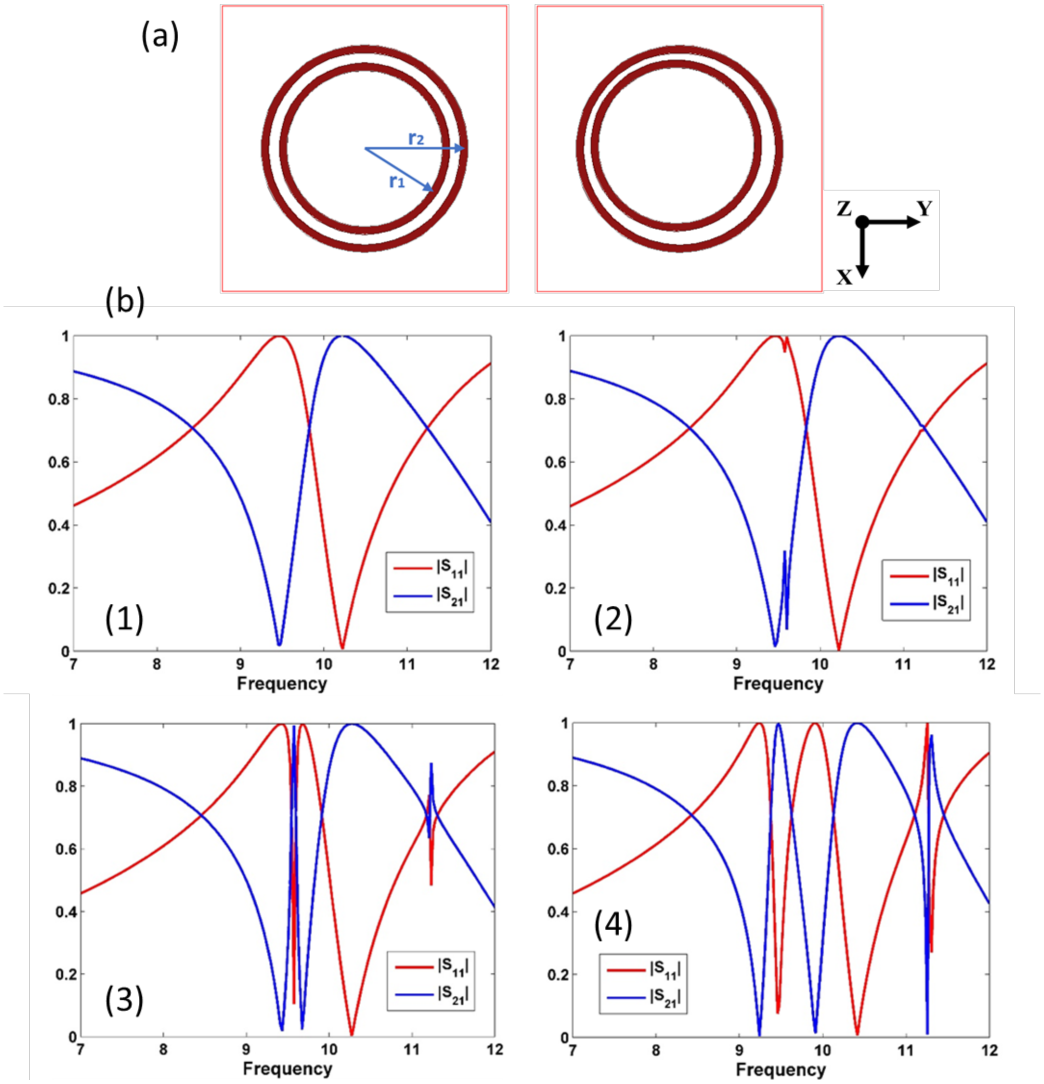

Figure 2.24: a) Unit cell designs of double concentric and non-concentric rings; r_1=4.3mm, and r_2=5.25mm; b) Transmission (blue) and Reflection (red) spectra of different centers separation, 1) 0, 2) 0.14mm, 3) 0.28mm, and 4) 0.42mm.

By shifting the center of the inner ring in the XY plane and along the y=x line, an additional EIT resonance at around 9.55 GHz emerges and becomes significant, and it reaches its narrowest band pass when ring centers separation, d, is about half of rings gap, Figure 2.24(b).

We further studied the electromagnetic properties of the metasurface by adding an outer ring to the double-ring design which generates extra resonances as one could expect, as shown in Figure 2.25. To have the number of passband frequencies doubled, the center of the inner and middle rings are shifted 0.84mm and 0.42mm respectively along the y=x line, and results are shown in Figure 3.

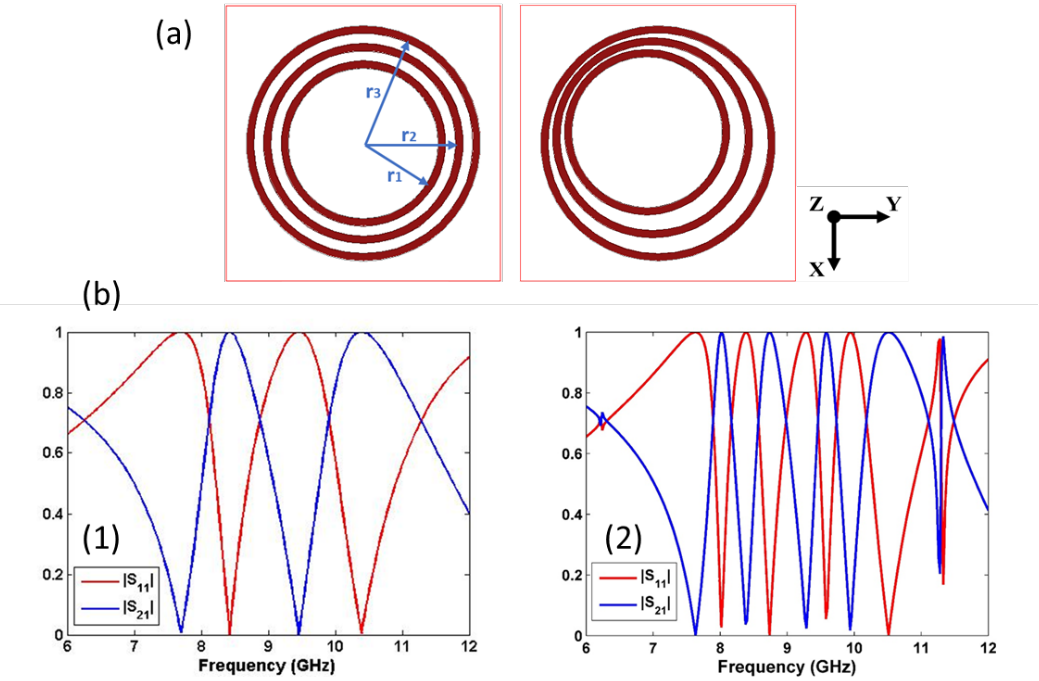

Figure 2.25: a) Unit cell designs of triple concentric rings in concentric and non-concentric orientations with r_3=6.2mm; b) transmission spectra for 1) concentric, and 2) non-concentric design.

Stacking a limited number of these planar metamaterials on top of each other can shift and modify the resonances which are due to couplings between the layers as far as the gap is in the subwavelength scale. Our simulations show that stacking more than two layers of double rings drastically decreases the average transmitted power as the loss increases due to additional mutual couplings and scattering off the planar resonators.

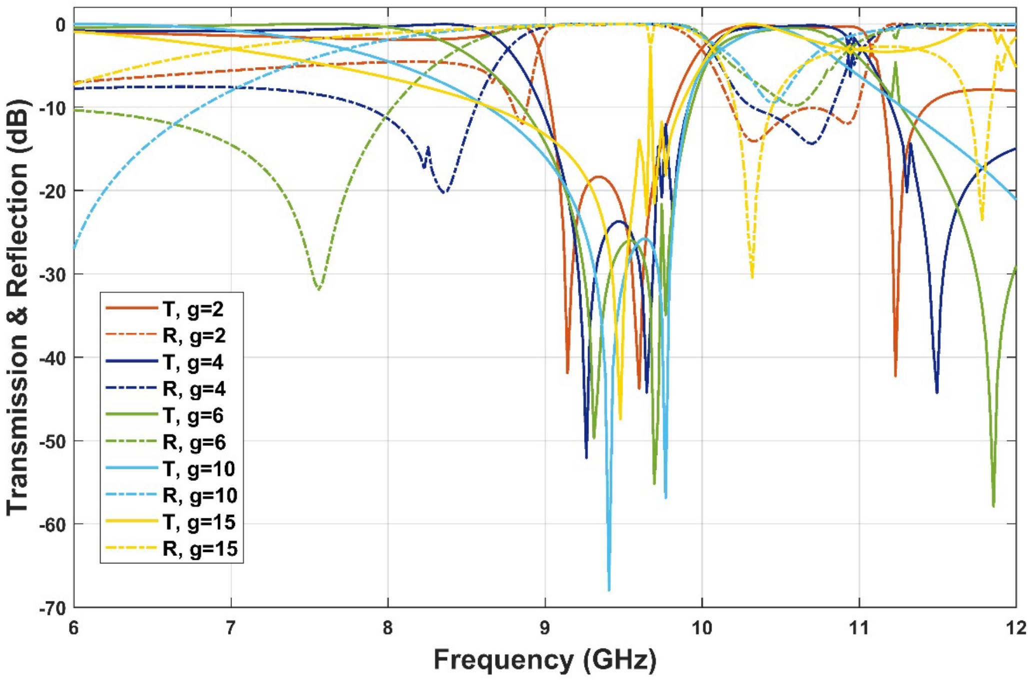

Figure 2.26: Transmission and reflection of a double layer of non-concentric double rings with different gap thickness (in mm).

Another method to manipulate the behavior of the metasurface and control its resonances is to use Babinet principle in design process [53]. Based on this principle, a complementary electromagnetic structure is obtained by swapping the metals and dielectrics in the design. The complementary metasurface has complementary impedance, therefore complementary transmission with respect to its original design. By combining a double ring and its complementary unit cell, a new unit cell is realized which has more resonances and is called a self-complimentary metasurface, Figure 2.27.

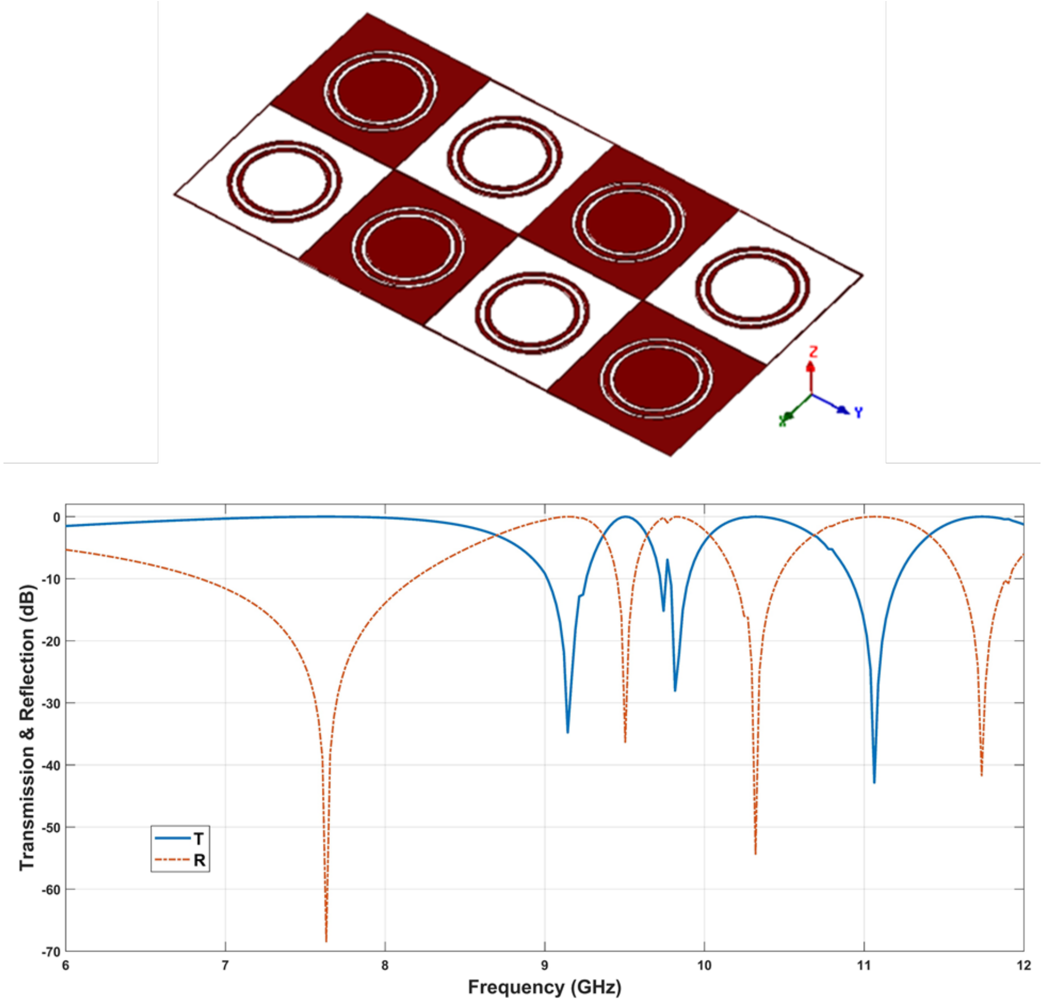

Figure 2.27: A self-complementary metasurface and its transmission and reflection spectra when the metasurface is infinitely extended on the XY plane.

In summary, we have investigated the role of asymmetries in multiple concentric ring metasurfaces, and it was shown that by introducing increasing symmetry breaking, ultra-narrow bandpass regions are achievable. Further studies based on this approach provide opportunities for developing spectral filters and modulators.

2.5. Conclusion

The background of S-resonator metamaterials was reviewed, and a new design was proposed. We used a well-established retrieval process for extracting the effective parameters of mirrored S-resonators metamaterial which show overlapping negative real values for permittivity and permeability within the frequency range of 5.8 GHz to 8.2 GHz. This results in a negative index metamaterial showing left-handed electromagnetic properties. We also studied the interactions of the metamaterial and the incident field in the time domain which itself shows a left-handed metamaterial. At last, we introduced a planar metamaterial and characterized its transmission and resonances which demonstrated its potential for applications such as filtering.

CHAPTER 3: NEGATIVE INDEX AND NEGATIVE REFRACTION

The concept of negative refraction and the backward wave has been the center of attention for a long time. The earliest idea goes back to 1904 when Arthur Schuster explored the possibility of backward wave effect [3]. He considered that backward wave might exist when there is an anomalous dispersion in the medium. In the anomalous dispersion region, absorption band, the wave velocity increases as the effective wavelength decreases, and therefore the group velocity and the phase velocity can have opposite directions. He concluded that the field energy propagates along the wave vector direction at the group velocity, but the phase velocity direction is anti-parallel. Schuster studied the possibility of backward waves and negative refraction in an isotropic dielectric material with an anomalous dispersion without considering the permeability and magnetic properties of materials. Moreover, he linked the origin of negative refraction to the negative phase velocity.

In his pioneering paper, Veselago [54] indicates the requirements of a left-handed material with negative real parts of permittivity and permeability to realize phenomenon such as negative refraction. To represent the mathematical framework of negative refraction, Figure 3.1 represents the negative refraction in a left-handed material (LHM) compared to the regular positive refraction in right-handed materials (RHM).

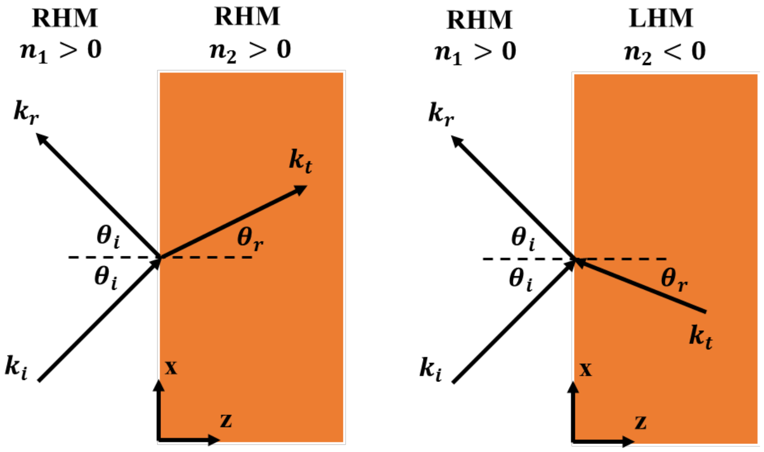

Figure 3.1: Positive refraction (left), and negative refraction (right).

By assuming an incident wave of polarization along the y-direction, the continuity condition of the electric field at the interface yields,

$$E_i e^{-j(\boldsymbol{k}_i.\boldsymbol{r}-\omega t)} + E_r e^{-j(\boldsymbol{k}_r.\boldsymbol{r}-\omega t)} = E_t e^{-j(\boldsymbol{k}_t.\boldsymbol{r}-\omega t)} \tag{3.1}$$

as the relationship between the incident, reflected, and transmitted waves. This equation can be simplified considering the boundary conditions as,

$$E_i e^{-j(k_{ix}x)} + E_r e^{-j(k_{rx}x)} = E_t e^{-j(k_{tx}x)} \tag{3.2}$$

with $k_x = \frac{\omega}{c} n \sin\theta$. Since Equation (3.2) must be valid at the interface, all wave vectors have to be the same. Therefore, the famous Snell's law is determined,

$$\theta_i = \theta_r \; ; \; n_1 \sin\theta_i = n_2 \sin\theta_t \tag{3.3}$$

moreover, for refraction from an RHM to LHM, the above equation becomes,

$$n_1 \sin\theta_i = -|n_2| \sin\theta_t \tag{3.4}$$

since $n_1 > 0$, it is obvious that the angle of refraction at the interface of RHM and LHM must be negative to satisfy the relationship, $\theta_t < 0$.

Another characteristic of the negative index medium is the backward wave which means the wave vector in the LHM material (here refracted medium) is toward the interface. Considering the refracted wave propagating at any point of $z \neq 0$,

$$\boldsymbol{k_t}.\boldsymbol{r} = k_{tx}x + k_{tz}z = \frac{\omega}{c}(n_2 \sin\theta_r\,\hat{x} + n_2\cos\theta_r\,\hat{z}) \tag{3.5}$$

in the conventional materials (RHM) the wave points toward a positive direction away from the interface as $n_2, \theta_r > 0$; but in the left-handed material the Equation (3.5) becomes,

$$\boldsymbol{k_t}.\boldsymbol{r} = \frac{\omega}{c}(|n_2|\sin(\theta_r)\,\hat{x} - |n_2|\cos(\theta_r)\,\hat{z}) \tag{3.6}$$

since $n_2, \theta_r < 0$, which demonstrated changing sign in the direction of the wave vector.

To review the propagation of the wave in a lossless left-handed material, we note that if only one of the effective parameters of ε or μ is negative, the material will act as a band gap medium and the wave cannot propagate. For instance, for the case with $\varepsilon < 0$ and $\mu > 0$, the refractive index is given by,

$$n = \sqrt{\varepsilon\mu} = \sqrt{-|\varepsilon||\mu|} = -i\sqrt{|\varepsilon||\mu|} \tag{3.7}$$

that satisfies the condition for the passive material. Inserting this term into the wave equation,

$$\boldsymbol{E} = \boldsymbol{E_0}e^{-i\frac{\omega}{c}n\boldsymbol{k}.\boldsymbol{r}} = \boldsymbol{E_0}e^{-i\frac{\omega}{c}\left(-i\sqrt{|\varepsilon||\mu|}\right)\boldsymbol{k}.\boldsymbol{r}} = \boldsymbol{E_0}e^{-\frac{\omega}{c}\left(\sqrt{|\varepsilon||\mu|}\right)\boldsymbol{k}.\boldsymbol{r}} \tag{3.8}$$

we see that the wave will attenuate in the material. However, if both ε and μ are negative, the refractive index is given by,

$$n = \sqrt{\varepsilon\mu} = i^2\sqrt{-|\varepsilon|}\sqrt{-|\mu|} = -\sqrt{|\varepsilon||\mu|} \tag{3.9}$$

that is real, and hence the wave propagates inside the medium.

Although when Veselago proposed the mathematical possibility of a double negative index material, left-handed material, there was not any available medium to experimentally validate the phenomenon. In 2000, Smith et al. reported the first metamaterial exhibiting negative index, [9]. Their structure was composed of metal rods and split-ring resonators (SRRs), Figure 3.2. They designed the size and geometry of the elements to have the effective permittivity and permeability with overlapping negative real values to realize a negative index medium with a propagating wave.

Figure 3.2: The first demonstrated metamaterial exhibiting negative index and negative refraction, [9].

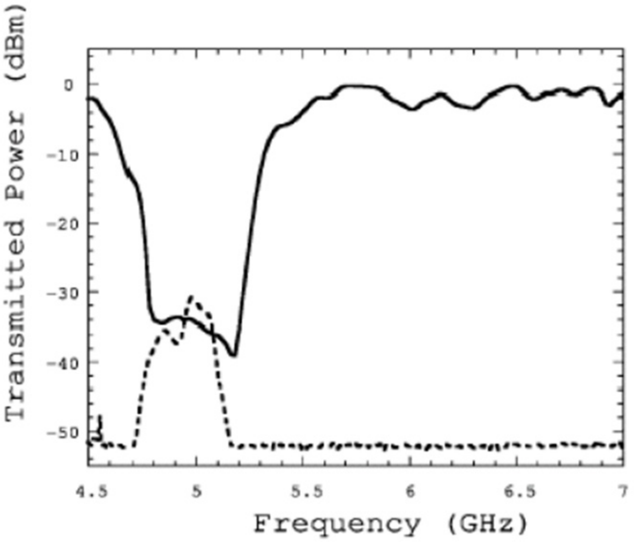

Figure 3.3: The measured transmission through an array of SRRs (solid line), and the left-handed metamaterial composed of metal rods and SRRs. (dashed line), [9].

The meta-atoms of this metamaterial were introduced before. Pendry et al. first proposed the metal rods medium as a structure with a plasma cutoff frequency at microwave, [10]. The array of metal wires exhibits a negative real effective permittivity with low loss and is a potential candidate to be implemented in designs to achieve a double negative index metamaterial. On the other hand, split ring resonators were reported to show a negative real effective permeability, [11]. It should be noted that to excite these mediums the incident wave should have certain polarizations, such as a polarization along the metal wires, or perpendicular polarization on the plane of SRRs for the magnetic field of the incident wave.

To verify the negative index region, they measured the transmission through the metamaterial. A peak in transmission magnitude confirmed the existence of a negative index at a frequency range in which both negative ε and μ were expected to be negative. Figure 3.3 illustrates the transmission for an array of only SRRs and the metamaterial with metal rods and SRRs. For the frequencies where SRRs, with negative μ, has a band gap, the composite metamaterial of wire rods and SRRs allows propagation of wave to confirm the negative index frequency range. It should be noted that the reason of low transmission magnitude in the LHM metamaterial is due to the loss and multiple scattering in the structure. An evidence of transmission through the metamaterial slab where ε_{eff} and μ_{eff} are expected to have negative real values is not sufficient to prove an actual negative index. The same group presented later an experiment to demonstrate the negative refraction [9]. Later on, newly designed structures were proposed to show a negative index of refraction at microwave [55]–[59], infrared [60], and optical regions [61]–[63].

The early realizations of such metamaterials had some limitations in their exotic characteristics including omnidirectional and polarization dependent properties, operating over a very narrow bandwidth, and limited functional frequency ranges due to constraints on building block materials and limitations in fabrication technologies [63]–[65]. To address these limitations and achieve structures with more flexibility regarding their functions, later efforts in designing metamaterials with more efficient performance led to interesting results such as all angles incident negative index metamaterials [66], and polarization independent negative index metamaterials [67]. Figure 3.4 shows some examples of such negative index metamaterials operating at different frequencies.

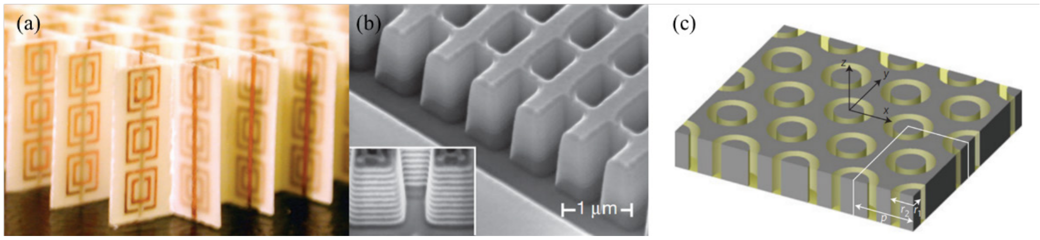

Figure 3.4: Some negative index materials designs, a) The first realization of NIM using SRR arrays with metallic wires at microwave frequencies [68], b) a SEM image of a fishnet metamaterial with negative index at near-IR frequencies [69], c) A polarization independent negative index metamaterial based on a single layer coaxial waveguide design [67].

A significant feature of negative index medium is the backward wave. In this case, the electric and magnetic field vectors, and the wave vector form a left-handed coordination. On the other hand, assuming in a plane wave, the relationship between Poynting vector, $\boldsymbol{S}$, and field vectors is,

$$\boldsymbol{S} = \frac{1}{2} Re(\boldsymbol{E} \times \boldsymbol{H}) \tag{3.10}$$

which is a right-handed rotation. Therefore, wave vector $\boldsymbol{k}$, and Poynting vector $\boldsymbol{S}$ are anti-parallel in a negative index medium which is also an isotropic medium. Hence, negative index of refraction implies existence of backward wave.

The above condition for the backward wave is also restricted to a lossless medium. By considering the presence of loss in the system, the condition of $\mu(\omega), \varepsilon(\omega) < 0$ have to be modified, [70], and to include the complex permittivity and permeability we have,

$$\sqrt{\varepsilon\mu} = \pm\frac{1}{2\sqrt{(\varepsilon' + |\varepsilon|)(\mu' + |\mu|)}}\big[(\varepsilon' + |\varepsilon|)(\mu' + |\mu|) - \varepsilon''\mu'' + i\{\mu''(\varepsilon' + |\varepsilon|) + \varepsilon''(\mu' + |\mu|)\}\big] \tag{3.11}$$

To have a negative phase velocity and backward wave, the real part of $\sqrt{\varepsilon\mu}$ must be negative and it implies,

$$(\varepsilon' + |\varepsilon|)(\mu' + |\mu|) < \varepsilon''\mu'' \tag{3.12}$$

multiplying sides of Equation (3.12) by $(\varepsilon' - |\varepsilon|)(\mu' - |\mu|)$, we conclude,

$$(\varepsilon' - |\varepsilon|)(\mu' - |\mu|) > \varepsilon''\mu'' \tag{3.13}$$

considering the complex wave number form as,

$$k = -\frac{\omega}{c}\frac{1}{\sqrt{2}}\left[\sqrt{\varepsilon'\mu' - \varepsilon''\mu'' + |\varepsilon\mu|} - i\left(\varepsilon'\mu'' + \varepsilon''\mu'\right)\sqrt{\frac{1}{\varepsilon'\mu' - \varepsilon''\mu'' + |\varepsilon\mu|}}\right] \tag{3.14}$$

the imaginary part of k must be positive to have the backward wave and it results in [71],

$$\varepsilon'\mu'' + \varepsilon''\mu' < 0 \tag{3.15}$$

Also, the power flow direction must be positive, and it requires the conditions of,

$$\varepsilon'|\mu| + |\varepsilon|\mu' < 0 \tag{3.16}$$

Equations (3.14) and (3.15) define the requirements for the existence of backward wave in a medium with negative phase velocity and index.

Although the presence of negative index implies negative refraction, it is not a valid statement the other way, and one should not associate negative refraction completely with a negative index. To support this statement, there is evidence that anisotropic crystals might exhibit negative refraction [72]–[75]. For instance, calcite which is an anisotropic crystal shows amphoteric refraction which means displaying positively or negatively refraction [76]. These anisotropic crystals only support forward wave and positive phase velocity but still demonstrate negative refraction.

Also, negative refraction can occur as a result of phase discontinuity over the scale of the wavelength [77]–[79]. Spatially varying sub-wavelength resonators lead to an abrupt phase change. The consequence is a correction to the Snell's law to represent this additional freedom in refraction theory. The general refraction law is obtained as,

$$n_t \sin\theta_t - n_i \sin\theta_i = \frac{\lambda}{2\pi}\frac{d\phi(x)}{dx} \tag{3.17}$$

with n_i and n_t as refractive indices of input and output media respectively, and $\phi(x)$ is the phase shift which is a linearly function of x on the plane of the interface.

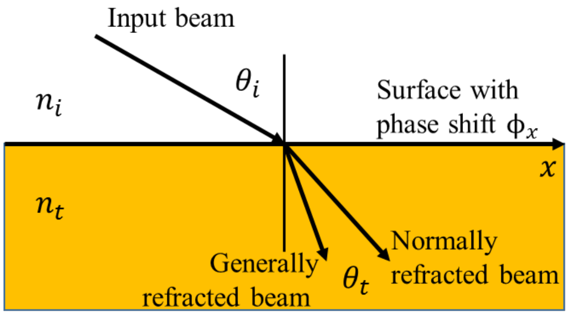

Figure 3.5: Schematic illustration of generalized refraction law. The phase shifts introduced on the surface between two media cause the beam refracted at an angle different than the classical Snell's law.

We can also consider the origin of these several physical phenomena from multiple scatterings due to interactions of the exciting field and the bulk structure with its array of meta-atoms. To have a better picture of periodicity effect on bulk properties of metamaterials, we can divide the total transmitted field ψ into different main terms by assumption of periodicity Λ being smaller than effective wavelength λ_{eff};

$$\begin{gathered}\psi_{transmitted} = \psi_{incident} + \psi_{scattered} \\ \psi_{scattered} = \psi_{dispersion+diffraction} + \psi_{weak\ scattering} + \psi_{refraction}\end{gathered} \tag{3.18}$$

A strongly scattering component that does not lend itself to interpretation by one of the above three terms describing the total scattered field, i.e. a $\psi_{strong\ scattering}$, leads to a very complicated output field that might not be possible to interpret in a useful way. If one is interested in enhancing the role of particular terms in above formula, then adjusting periodicity with respect to effective wavelength becomes crucial. For instance, $\psi_{dispersion}$ requires strong scattering in the structure and it can be realized when periodicity Λ becomes of the order of the wavelength λ. Choosing the structure periodicity in a way that metamaterials can be assumed to be well represented by a homogenized or averaged quantity requires no k-dependence except that dictated by inherent symmetries in the bulk structure. Usually the metamaterial community accepts periodicity of λ/6 as sufficiently small enough for metamaterials to be considered homogenous and an effective medium model can be applied defining classical constitutive parameters such as refractive index. Constitutive parameters are distinctly averaged quantities and it could be appropriate to consider them when the bulk structure is away from system resonances, but these effective parameters are less reliable close to resonances, especially strong resonances which have a large Q factor. In highly temporally dispersive regions, in contradistinction from highly spatially dispersive media, the energy transport can be very difficult to describe and the simple input-output, model from which an effective index can be inferred might not be reliable. However, it is precisely close to strong resonances that the more extreme parameter values, e.g. a negative index, are likely to be realized. Therefore, the credibility of an effective medium model can be increased by studying the fine structure of the ω-k dispersion diagram.

3.1. Negative Index and Negative Refraction in S-resonators

We consider bulk properties of the metamaterial such as negative refraction where the periodicity of, and scattering from subwavelength elements contribute. To confirm that our designed mirrored S-resonator metamaterial exhibits double negative properties, we simulate refraction experiment using a prism made out of the S-resonators. As we saw previously, the extraction methods are only an approximate approach in anticipating effective parameters, and it is possible that they fail in predicting accurate parameters due to fundamental restrictions based on their assumptions, for instance, the size of meta-atoms which have to be in sub-wavelength scale.

In the previous chapter, the retrieved parameters for the mirrored S-resonator metamaterial show a negative refractive index which implies overlapping negative real values for effective permittivity and permeability. As Equation (3.15) indicates, there is a modified condition in the presence of loss in the structure which determines the relation of complex effective parameters in a negative refractive index regime. This condition is mathematically evaluated for our S-resonator metamaterial, Figure 3.6. The $\varepsilon'\mu'' + \varepsilon''\mu'$ term is negative in the frequency range which extracted refractive index is negative, therefore confirming the retrieval procedure to anticipate effective parameters.

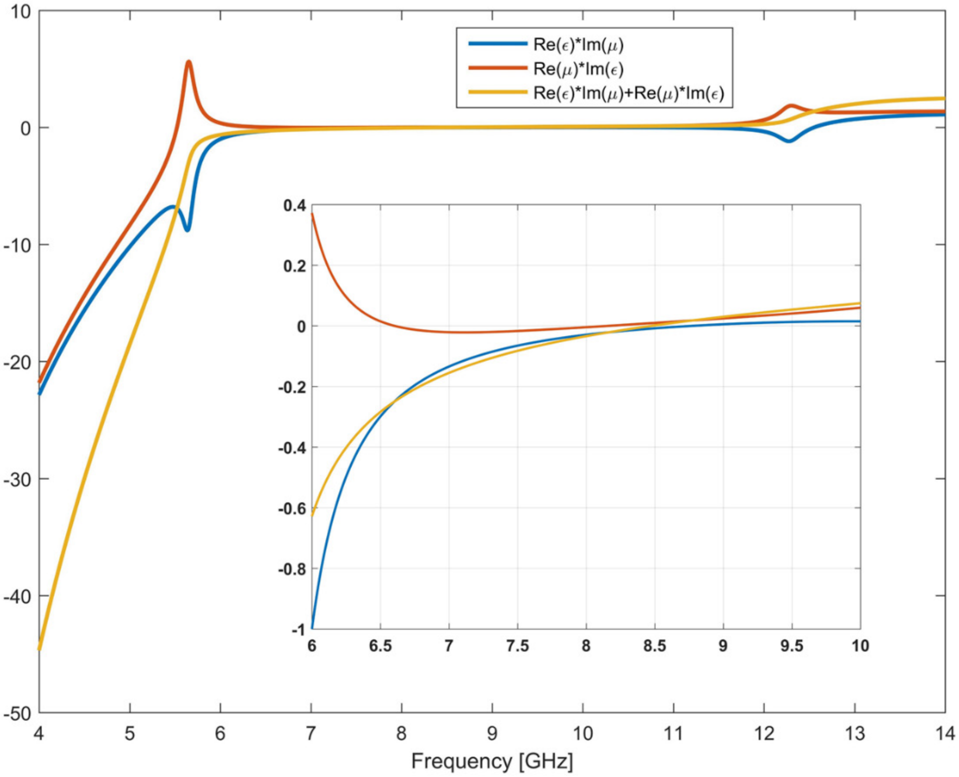

Figure 3.6: Representation of the condition in Equation (3.15) for mirrored S-resonator metamaterial as the requirement to realize a negative refractive index in a metamaterial with the loss.

To further understand the behavior of the S-shaped resonators structure, we simulate a prism made out of the unit cell which was shown before and illuminate the structure with a plane wave that is normally incident and has a p-polarization. The simulation output would be able to validate the results of extracted refractive index for frequency regions where we expect a valid physical meaning. Since the approach in this numerical refraction experiment is a full-wave simulation of a bulk structure, the calculated fields are a direct consequence of interactions of electromagnetic fields with the materials and the geometry of the structure. So, the results are independent of any extracting method results and are an effective tool to compare with extracted effective parameters. Figure 3.7 illustrates the simulation setup of the prism enclosed in an air box which has periodic boundaries in the XY faces to have the structure extended infinitely along the z-direction. The rest of faces are set as absorption boundaries to eliminate any back reflection and scattering off these faces. The prism is composed of 9 unit cells of the S-resonators along its X and Y faces and is filled with complete unit cells and partial unit cells on its exit face. It should be stated that following simulation results are all conducted for a steady state with a continuous wave illumination.

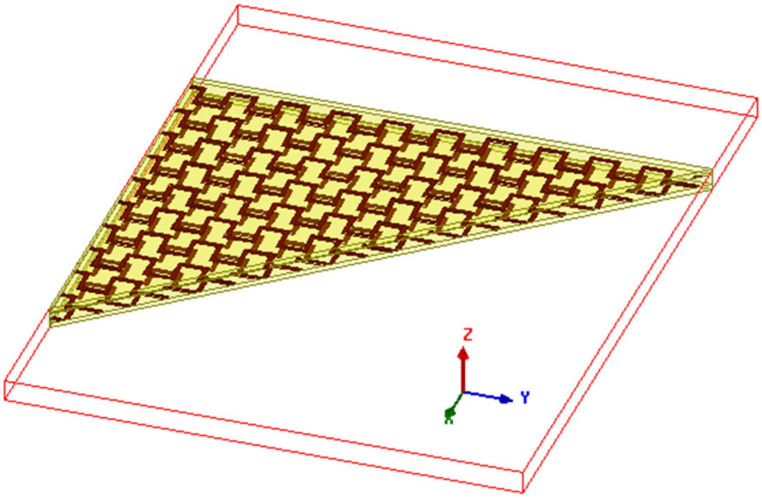

Figure 3.7: Simulation setup of a prism made with S-resonators. All faces of XY are periodic boundaries to have the structure extended infinitely in the z-direction. Absorption boundaries are set on the XZ, and YZ faces.

The E-field magnitudes of different frequencies are shown in Figure 3.8. As can be seen, a negative refraction is obtained at 7.2GHz. Increasing the frequency of the incident plane wave, the refracted wave from the exit face of prism tilts toward the normal vector of the exit face and then enters the positive refraction region. So, the refracted wave is closer to the normal vector at 8GHz, and it is away from the normal vector and is a positive refraction at 9.4GHz. By comparing the observed refraction angle over the same range of frequencies shown in Figure 3.8 to Figure 2.14, we conclude that they match relatively well with the refractive index values extracted from S-parameters. The reasons behind differences between refraction results and extracted index values come from the numerical approximation in both methods; the increasing number of unit cells along propagation direction which would slightly change the effective parameters of the bulk structure in these regions, and presence of boundaries which their minimum interference with total fields would make it extremely difficult to measure the refracted wave quantitatively.

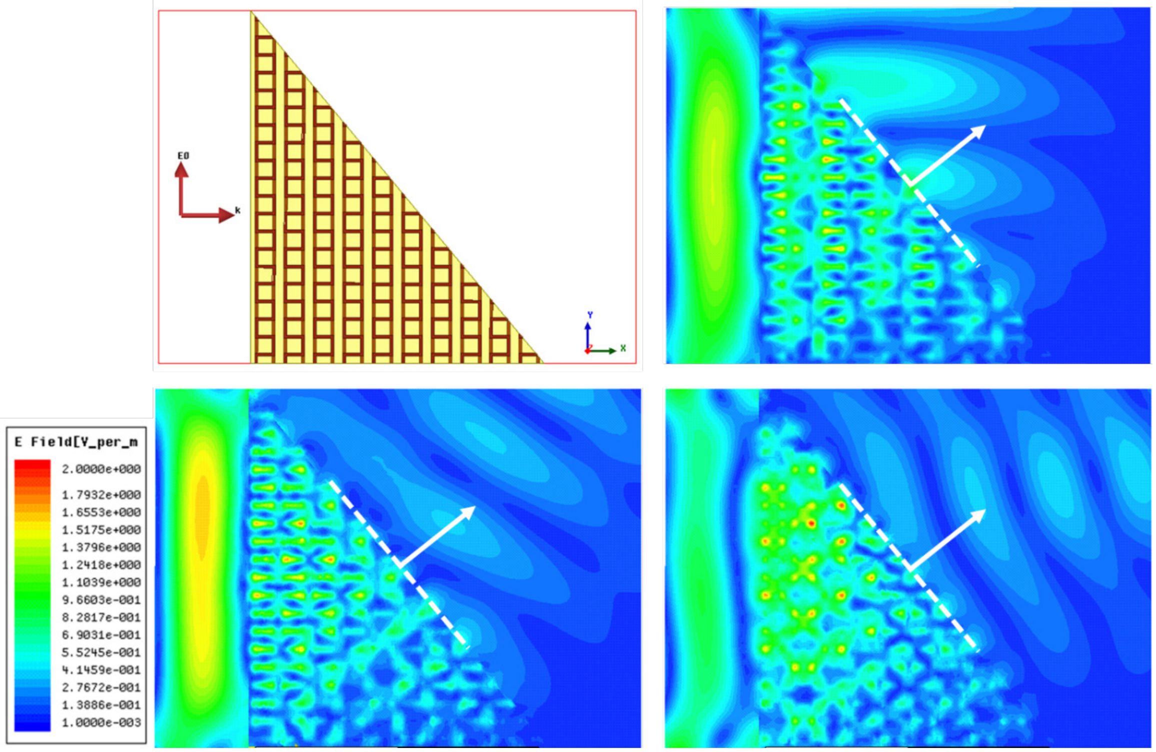

Figure 3.8: Refraction of the incident plane wave by a prism made out of S-shaped resonators. The incident plane wave propagates along x-direction with polarization along the y-direction. The dashed line represents exit interface of the prism while the dashed arrow indicates the normal vector to the exit face. Different frequencies of (top-right) 7.2GHz, (bottom-left) 8GHz, and (bottom-right) 9.4GHz are shown.

To examine that the seen negative refraction is due to an effective negative refractive index, and it is not arising from multiple side lobes, diffraction phenomena, or band gap phenomenon in photonic crystals, we simulated a prism which has defects in its structure. To represent defects, metal strips from two unit cells are removed, Figure 3.9. Although the exit face has a jagged pattern, we do not expect to see a change in the behavior of the effective bulk properties since the patterns are in sub-wavelength scale. An interesting observation is that by introducing defects, the prism loses its ability to exhibit negative refraction. Moreover, it does not represent the expected behavior of a bulk structure obtained through extraction method.

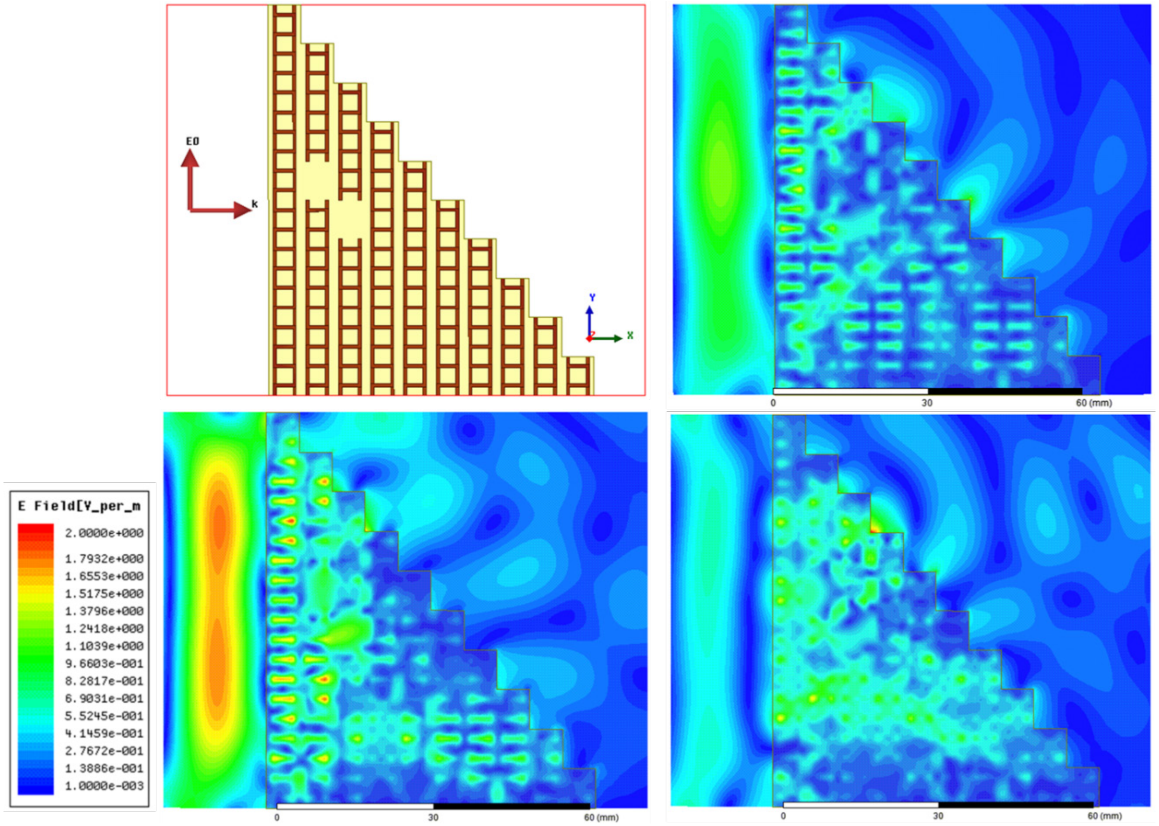

Figure 3.9: Refraction of the incident plane wave by a prism with defects. The incident plane wave propagates along x-direction with polarization along the y-direction. Different frequencies of (top-right) 7.2GHz, (bottom-left) 8GHz, and (bottom-right) 9.4GHz are shown.

Another concern is that the negative refraction arises from the phase discontinuity on the plane of the exit surface. There are no subwavelength features which are varying over the scale of the wavelength at the interface to introduce spatially phase variation, but actually, all resonators are the same on the exit face. However, to inspect the effect of phase discontinuity on the surface caused by resonators, we conduct additional simulations with only unit cells on the surface. Figure 3.10 shows the simulation setup and results with two unit cells on the exit face; the simulation of only one unit cell was also exhibiting the same trend, and we only include following figures as a demonstration of the effect. It is clear that the prism which only has sub-wavelength resonators on the exit surface is not displaying the refraction we see in the bulk structure. This is another confirmation that the negative refraction observed in the complete bulk metamaterial arise from the negative refractive index.

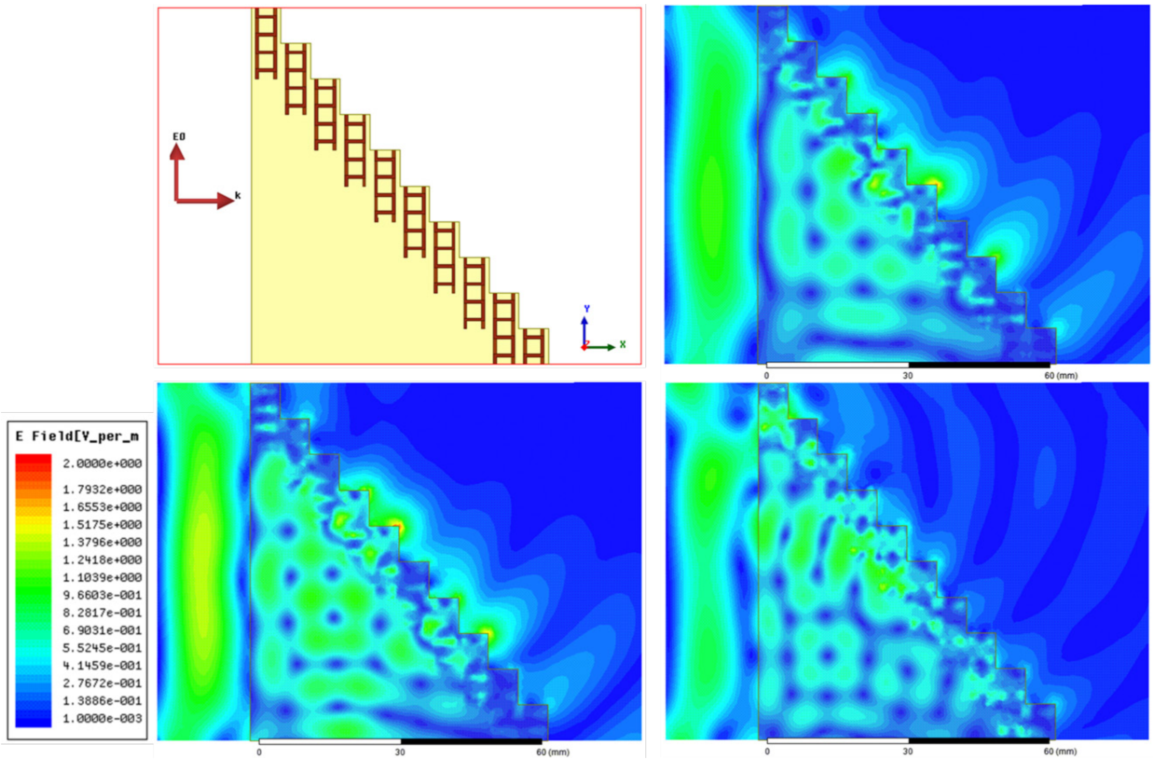

Figure 3.10: Refraction of the incident plane wave by a prism with S-resonators on the exit surface. The incident plane wave propagates along x-direction with polarization along the y-direction. Different frequencies of (top-right) 7.2GHz, (bottom-left) 8GHz, and (bottom-right) 9.4GHz are shown.

Although a negative refraction effect can be a direct consequence of negative refractive index, the question is whether the observed negative refraction in the prism is definitely due to an effective negative refractive index or arise from the shape of the associated equifrequency surface in wave vector space which would be a consequence of spatial dispersion derived from the periodicity of meta-atoms. The alternative approach to justify this concern is through investigating the nature of dispersion in the structure. Plotting dispersion diagrams can be helpful here, Figure 3.11. Based on these plots, we can conclude that homogenization works for frequencies blow 15GHz when the incident angle is between normal and about 65-degree oblique. For frequencies above 15GHz, homogenization fails; where the effective wavelength in the FR4 substrate is about 10mm. At these high frequencies, there are more complex interactions arising from Bragg-like diffraction effects. On the other hand, at lower frequencies, a Faraday Cage effect appears blocking incoming field. The relatively large size of the meta-atoms in this case, with respect to the effective size of the wavelength in the FR4 substrate, might suggest that we should not have homogenization. However, presumably due to the very strong interactions between the meta-atoms, it appears that we have homogenization as a result of the strong couplings between the S-shaped resonators leading to a contribution to the bulk behavior of the metamaterial. Under these conditions, the scattering parameters also seem to be reliable in specifying the effective medium properties of the metamaterial, such as refractive index.

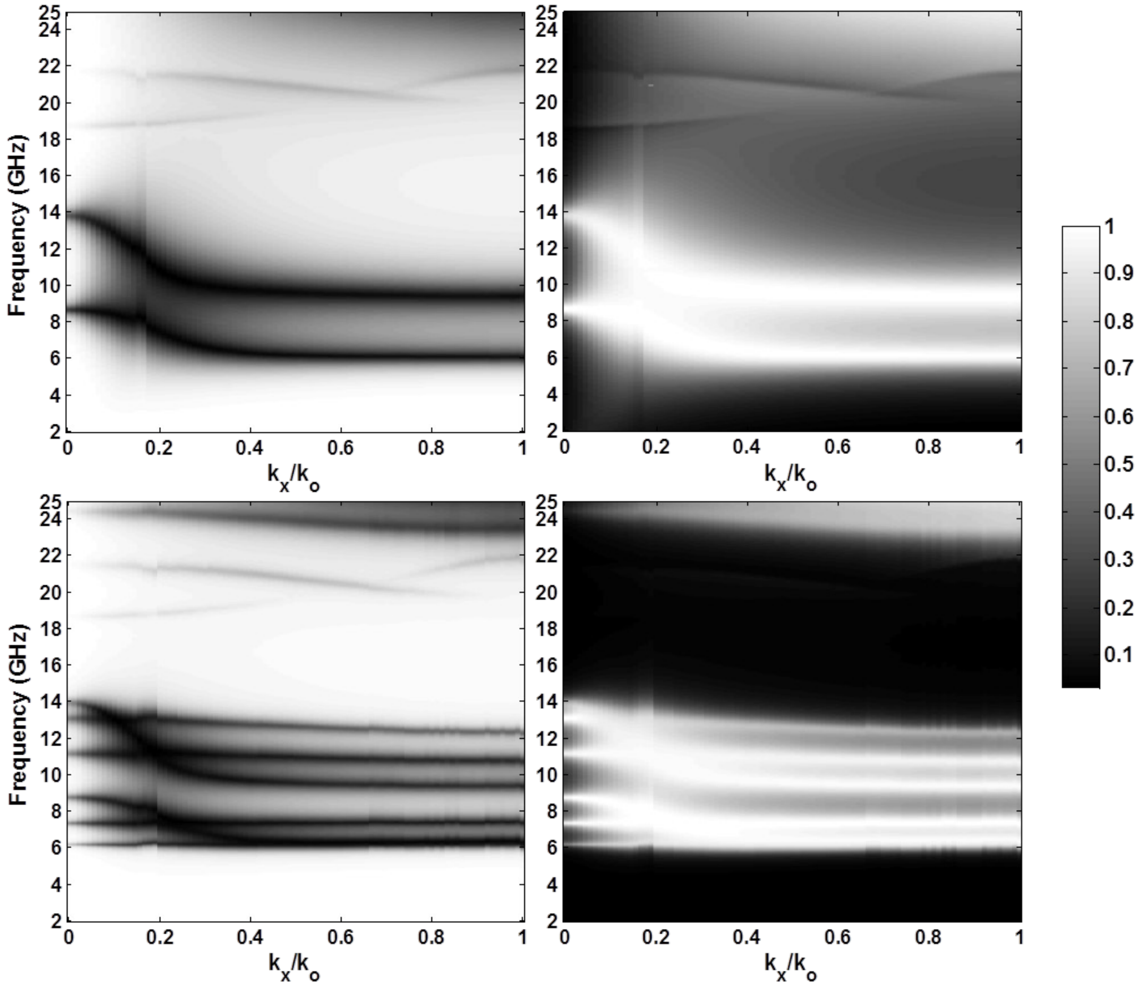

Figure 3.11: Dispersion diagrams for (top) single, and (bottom) triple S-resonators along the propagation direction, x. (left) corresponds to reflectivity and (right) to transmissivity.

The relatively large size of the meta-atoms in this case, with respect to the effective size of the wavelength in the FR4 substrate, might have suggested that we should not expect homogenization and that,

$$\psi_{scattered} \approx A\psi_{dispersion+diffraction} + B\psi_{weak\ scattering} + C\psi_{refraction} \qquad (3.19)$$

However, presumably due to the strong coupling between the S-resonators, it appears that we do have quite good homogenization and $C \gg A$ & B which leads to background clutter. The latter appears to lead to the contribution of the bulk behavior of the metamaterial because of the associated distributed or non-local response of highly coupled clusters of meta-atoms. This presumably supports the observation that we can use scattering parameters to calculate the effective medium properties of the metamaterial such as refractive index in the 5.5-15GHz band, based on these numerical simulations.

In summary, we have investigated the scattering in metamaterials where the periodicity of meta-atoms is only slightly less than the effective wavelength inside the structure. We also studied how this contributes to the bulk effective parameters, scattering, and refraction and properties of the metamaterial. Scattering and diffraction from the periodic arrangement of the meta-atoms could explain apparent refracted wave outputs as a result of Bragg-like behavior. However, strong coupling between the S-resonators is shown to lead to effective media models remaining valid even when the effective wavelength of the radiation inside the metamaterial is comparable to the period of the meta-atoms. Therefore, we can conclude that the observed negative refractive index is due to a negative index and that the index value is consistent with that derived from a scattering parameter analysis when we are in this scattering regime.

3.2. Conclusion

We reviewed the origin of the negative index and negative refraction and their correlation. Following then, we investigated the scattering in metamaterials where the periodicity of meta-atoms is only slightly less than the effective wavelength and studied how this contributes to the bulk scattering, refraction and transmission properties of the metamaterial. Scattering and diffraction from the periodic arrangement of the meta-atoms could explain apparent refracted wave outputs as a result of Bragg-like behavior even if adjacent or, for example, every other meta-atom were to mimic a grating-like structure. However, strong coupling between resonant meta-atoms, here S-shaped resonators is shown to lead to a dominating homogenization phenomenon. This in turn justifies as effective medium model remaining valid even when the effective wavelength of the radiation inside the metamaterial is only greater than the unit cell length of ~ 0.8cm. We can conclude that the observed negative refractive index is due to a negative index and that the index value is consistent with that derived from a scattering parameter analysis when we are in this scattering regime. For the shown example, this statement appears to be the case even when the period is about the length of an effective wavelength, but it is not true for higher spatial frequencies. In the higher frequency band, above 15GHz, homogenization fails; where the wavelength in FR4 is about 1cm.

CHAPTER 4: ADDRESSING BANDWIDTH AND POLARIZATION CONCERNS

Narrow operating bandwidth and polarization dependency of metamaterials have hampered exploiting resonances for unusual bulk refractive indices. Metamaterials, in particular, need to improve their performance on these concerns to find a path toward real world application. For instance, invisibility cloaking requires metamaterials with broad bandwidth, polarization-independent performance, and lower loss and dispersion [80]–[85]. Various approaches have been considered to tackle these issues in GHz, THz, and optical frequencies. A negative index metamaterial with polarization-independent parameters was proposed in microwave regime using metal-dielectric-metal multilayered fishnet structure [86]. Fishnet structures have received significant attention due to the feasibility of fabrication in smaller scales for optical frequency ranges; suggested designs promise to alter resonances and offer independent polarization response [87], [88]. Some proposed designs deliver bandwidth and polarization control for only one of the fundamental electromagnetic parameters such as polarization-independency for permittivity [89], or high bandwidth in magnetic response for a metasurface [90].

To address these concerns, we numerically study the role of a metamaterial substrate on the refractive index bandwidth of an otherwise homogenized metamaterial. Also, we explore modified designs to build a polarization dependent metamaterial which still exhibits negative refractive index. As expected there is a trade-off between loss and bandwidth but with some significant and useful features.

4.1. Bandwidth Control

The S-shaped resonator design has two distinct magnetic and electric resonances arising from a split loop and metallic bar in the unit cell for an incident wave with a polarization component along the bar. To modify the resonances, we add a resonator to the design which has a resonance close to the S-element resonances resulting in the mutual coupling of resonators, enhancement of interaction between meta-atoms and therefore modifying the effective parameters of the design.

4.1.1. Conducting Wire Medium

It has been shown that a conducting wire medium with certain periodicities and dimensions has a negative effective permittivity [41], where the effective plasma frequency depends on the wire radius and spacing of the medium.

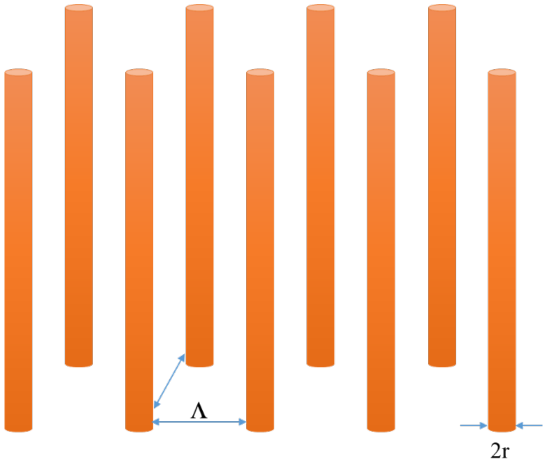

Figure 4.1: Geometry of an infinite periodic array of conducting wires

Using periodically loaded transmission line model, we can estimate the effective permittivity of the medium [91],

$$\frac{\varepsilon}{\varepsilon_0} = \frac{1}{(k\Lambda)^2}\left\{\cos^{-1}\left(\cos(k\Lambda) + \frac{\pi}{k\Lambda\log\left(\Lambda/(2\pi r)\right)}\sin(k\Lambda)\right)\right\}^2 \tag{4.1}$$

where ε_0 is the vacuum permittivity, k is the wave number of the incident field, Λ is the lattice constant, and r is the wire radius.

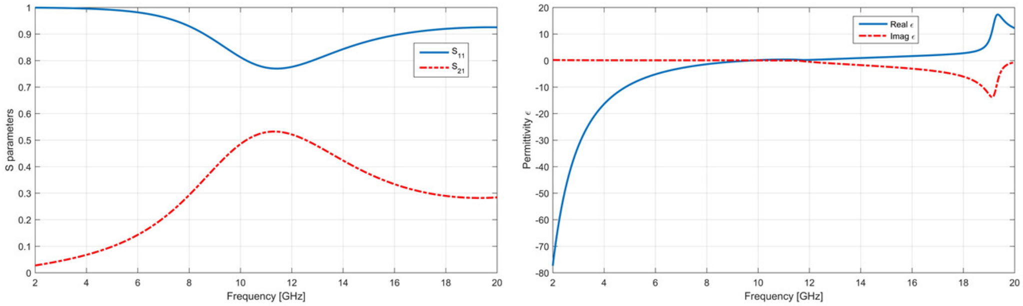

Figure 4.2: Simulated S parameters of a wire medium made of copper with rods radius of 0.3mm and lateral periodicity of 3.3mm (left), and extracted effective permittivity (right).

A wire medium consisting of copper rods in a host dielectric medium with ε=4.4 was simulated with an incident propagating wave perpendicular to wires and polarization along them. The radius of wires assumed as 0.3mm and the lateral lattice constant was set as 3.3mm. There was only one row of wires along propagating direction. Figure 4.2 shows the calculated S-parameters as well as extracted effective permittivity. The S-parameters show a resonance around 11 GHz, and consequently, the frequencies below plasma frequency correspond to negative effective permittivity.

4.1.2. Meta-Substrate

We can use the natural resonance of wire medium to provide an additional significant electrical resonance to the S-shaped resonator to broaden the bandwidth of negative permittivity. Although composite metamaterials that are consisting wire medium (electric resonator) and split-ring resonators (magnetic resonator) are well-known for quite a long time [9], there is very limited literature on combining a self-consistent design like S-resonator, possessing both electric and magnetic resonances, with another resonator. It is worth mentioning that a composite design of S-resonators and closed rings, as magnetic metamaterials, has been suggested to control the bandwidth [92].

We introduce copper rods into the already established metamaterial design that leads to strong couplings and scatterings of elements and hence a modified effective permittivity will be delivered compared to the case without rods. The copper wires are inserted in the center of the unit cell and aligned along the polarization of the incident wave, so the exciting field causes an electrical resonance in wires, Figure 4.3. The substrate then can be interpreted as an inhomogeneous electrical substrate.

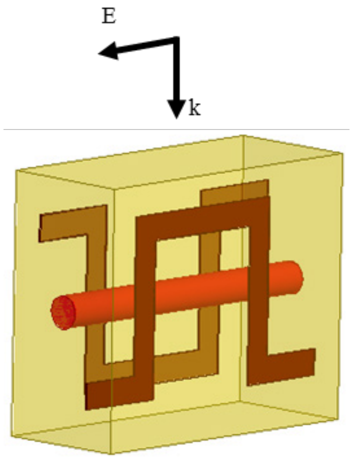

Figure 4.3: The metamaterial unit cell of mirrored S-elements and rod with respect to incident wave polarization. (images are from our published paper [93])

By changing the radius of rods, we can interpret the mutual couplings between the S-elements and the wires. As it can be seen in Figure 4.4, by only inserting rods in the structure of S-elements, there is a blue-shift for electrical resonance, and the magnetic resonance remains almost without any change. Increasing the radius of rods (from 0.2mm to 0.6mm) induces a larger blue-shift for electrical resonance. Also, the impedance amplitude corresponding to electrical resonance increases which are in accordance with a stronger scattering of incident wave by a larger cross section of wires when their radius increases.

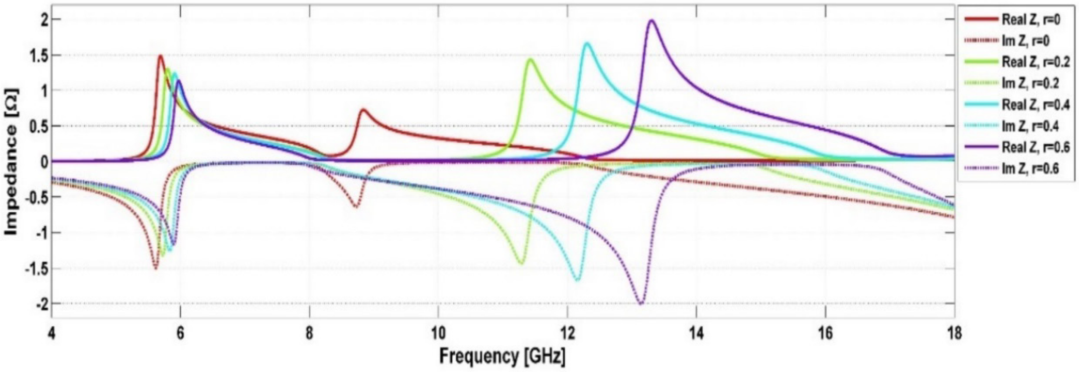

Figure 4.4: Directly calculated impedance from S-parameters. Increasing the radius of rods results in a blue-shift in electrical resonance while the magnetic one almost remains constant; Λ is 3.2mm.

To understand the impact of adding wires on refractive index, a comparison is made between the refractive index of S-resonators and S-resonators with wires, Figure 4.5. The negative index region in the original S-resonator structure sees a blue-shift less than 0.2GHz when wires are added to the design, whereas the positive region is shifted about 3GHz toward higher frequencies.

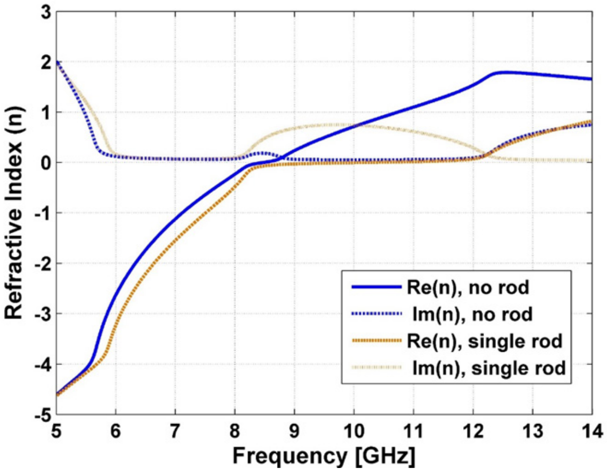

Figure 4.5: Comparison of effective refractive indices of metamaterial structure with and without rods of diameter 0.8mm and Λ of 3.2mm. (images are from our published paper [93])

From retrieved values for index we calculated permittivity, and as we were expecting, there is a broadening in the bandwidth of negative permittivity by inserting wire medium.

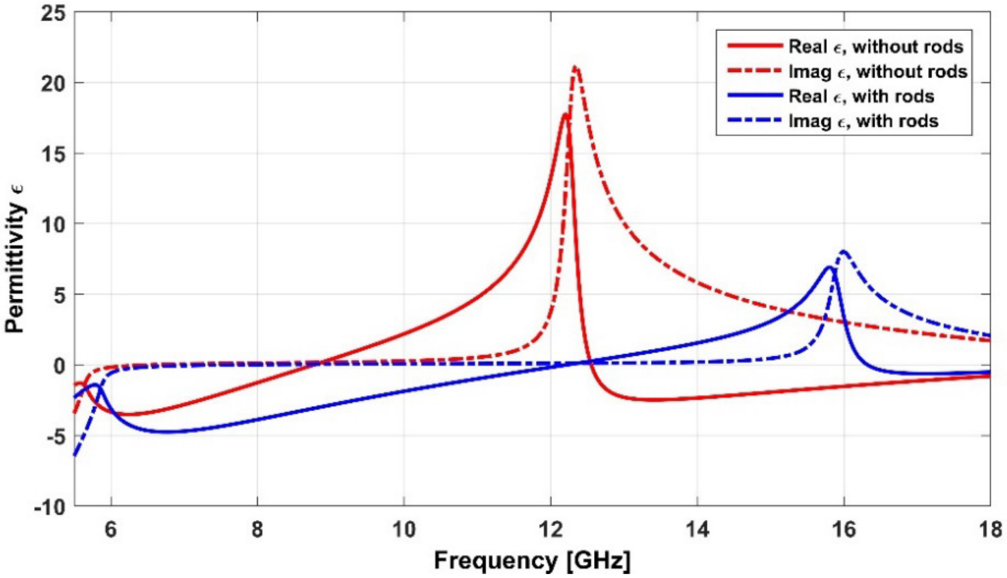

Figure 4.6: Comparison of effective permittivity metamaterial structure with and without rods of diameter 0.8mm and Λ of 3.2mm. (images are from our published paper [93])

To verify the numerical results obtained through FEM using Ansys HFSS, we performed the simulations in FDTD method using Lumerical FDTD software. Although simulation procedures and approaches are different but having very similar results ensures that there are no numerical artifacts in calculated data, Figure 4.7.

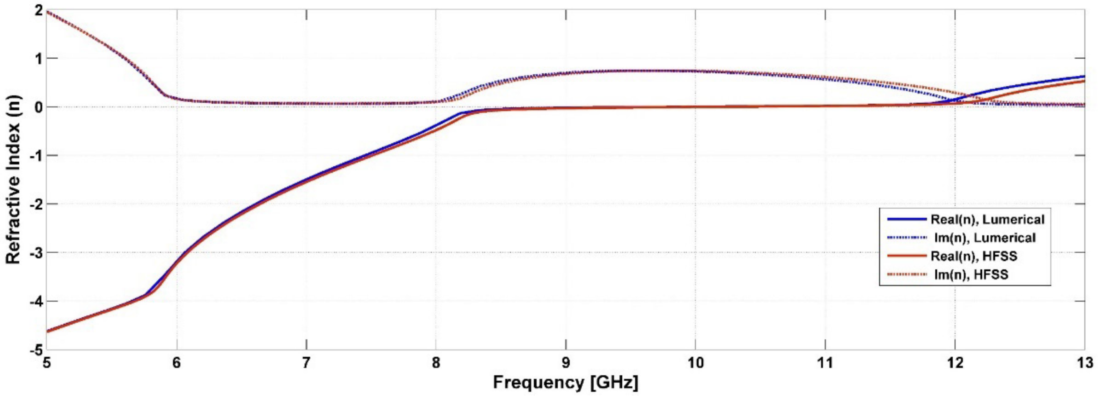

Figure 4.7: Comparison of extracted effective refractive indices using HFSS and Lumerical for metamaterial structure with rods of diameter 0.8mm and Λ of 3.2mm.

So far we only investigated the effect of adding one rod in the propagation direction. By inserting multiple rods along the propagation direction, we can manipulate magnetic resonance of S-resonators as a result of stronger magnetic effect and coupling arising from mutual inductance in multiple rods.

Figure 4.8(a) illustrates the unit cell with multiple rods inserted along the propagation direction. We see an adamant blue-shift in both magnetic and electric resonances compared to the original structure; this has been shown in Figure 4.8(b) with a comparison of impedance for the original mirrored S-resonators and its composite with inserted wire medium with multiple rods along the propagating wave. Therefore, by introducing the capability of controlling the magnetic resonance through additional rods, one would be able to monitor and control the bandwidth of effective bulk parameters efficiently.

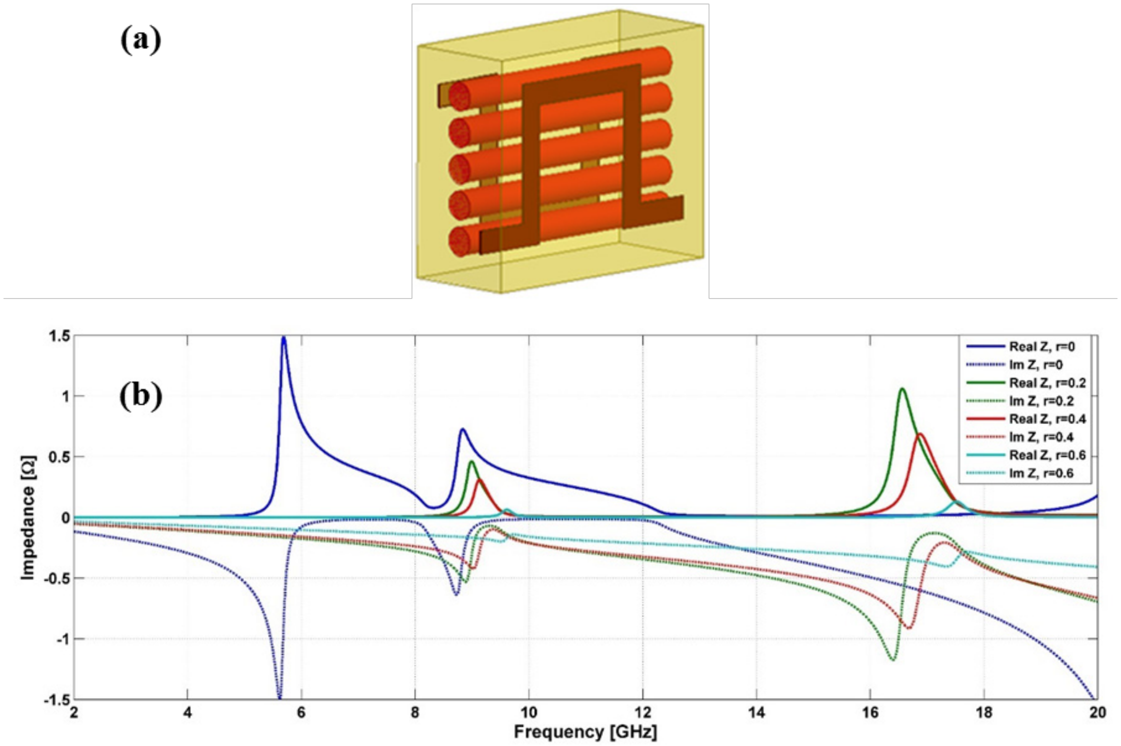

Figure 4.8: (a) Unit cell design with multiple rods along propagating wave. (b) Calculated Impedance for simulations of original design without wire medium and when multiple rods are inserted, geometry parameters are the same as before. (image (a) is from our published paper [93])

We conducted further studies on bulk properties of the metamaterial design with wire medium by simulating a prism made out of the desired structure. Through this simulation, we can verify the credibility of extracted indices by inspecting the refraction via exit face of the prism. In Figure 4.9, the incident wave travels along z-direction with a polarization along the x-axis. The prism is extended infinitely in y-direction that is applied by periodic boundaries on XZ planes; the rest of planes are set as field absorbing boundaries.

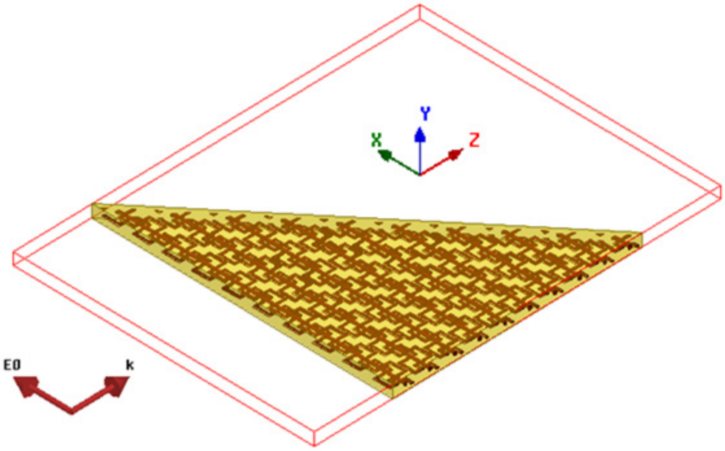

Figure 4.9: Simulation setup of a prism made with S-resonators and copper rods between them. Wave vector and polarization of the incident wave are depicted.

The results, Figure 4.10, show that extracted values for refractive index follow the refraction behavior of the bulk structure at all desired frequency ranges. For instance, at a frequency range that we expect both metamaterials to exhibit negative refractive index, we observe negative refractions, Figure 4.10(a). At a frequency of 9 GHz, the S-resonator metamaterial approaches zero index values, so the refraction is tilting toward the normal axis of prism exit face; on the other hand, this frequency for S-resonator and wire medium relates to the band gap according to the retrieved index curve, Figure 4.10(b). Moreover, at a higher frequency of 12.5 GHz, the incident wave can pass through the exit face of prism for S-resonators with wire medium while S-resonator design shows a higher value for the index of refraction, Figure 4.10(c). It should be mentioned that the generated spherical waves in Figure 4.10(b) in prism made with S-resonators and wire medium corresponds to the penetration and diffraction of field through the thin part of the prism at top which goes to singularity at boundary point; and it doesn't represent the refraction of the whole prism as plotted fields in HFSS was normalized to view the fields more clearly.

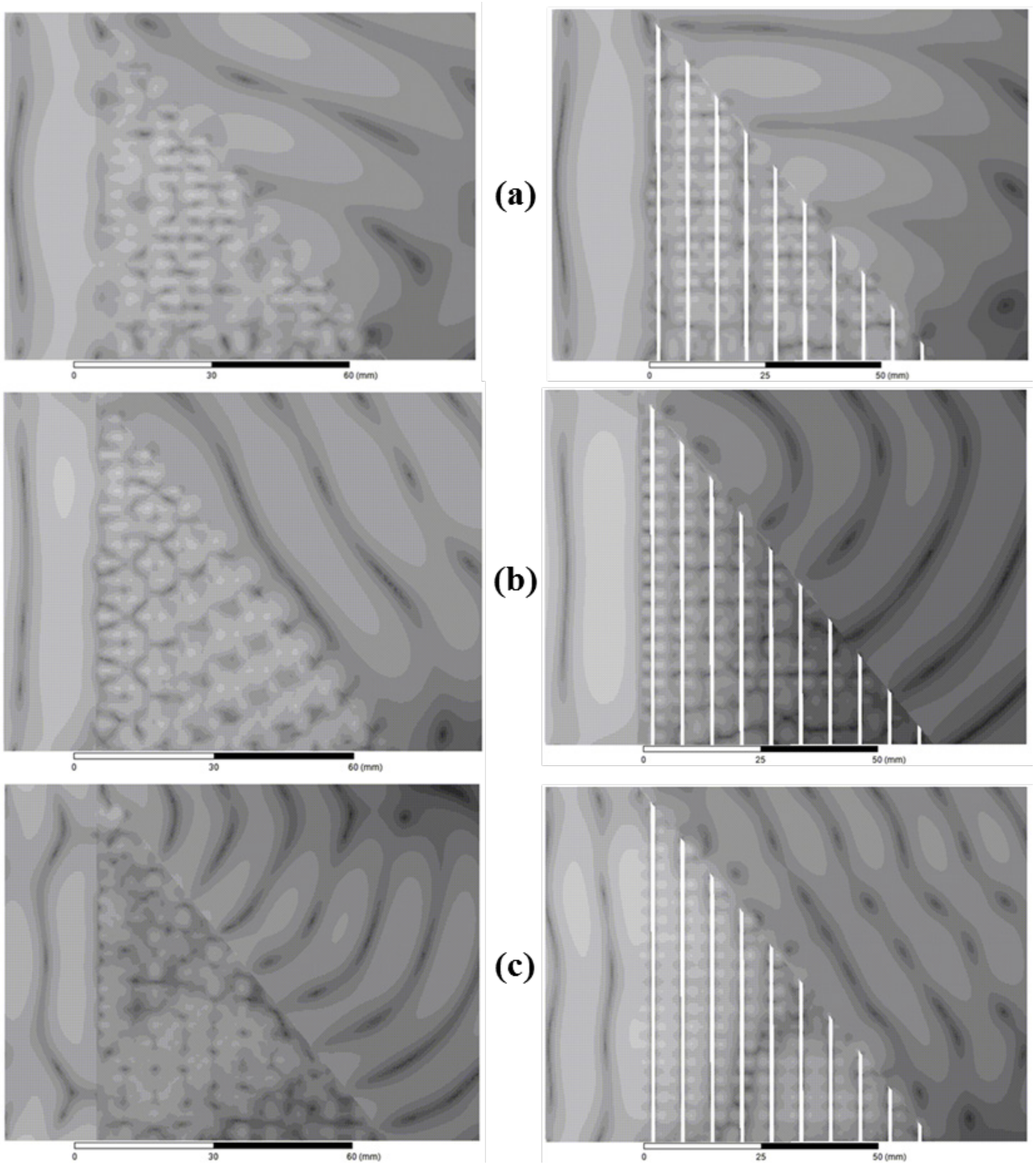

Figure 4.10: Comparison of refraction in prisms made out of only S-resonators and S-resonators with rods. (a) Incident wave frequency=7.5GHz; (b) 9 GHz; and (c) 12.5 GHz.

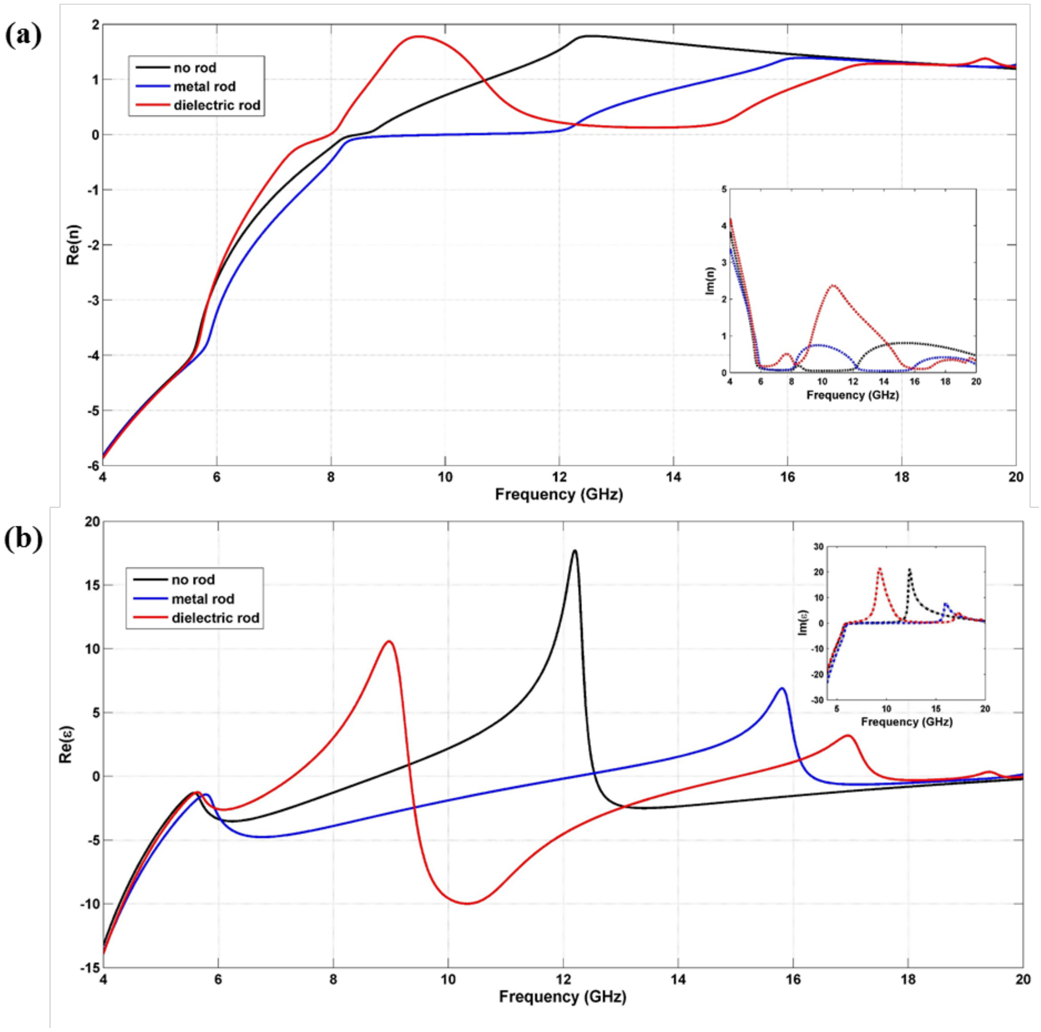

Figure 4.11: Comparison of effective parameters between different metamaterial structures. Black lines represent the original mirrored S-resonators, blue lines refer to insertion of metal wires, and red lines are for insertion of high dielectric rods (ε=80). The diameter of rods is 0.8mm, and their lateral lattice constant is 3.2mm. (a) Effective refractive index, (b) Effective permittivity.

Metal rods with their free electrons can follow the incident field variations and therefore the phase of their polarization is very close to that of metal traces in the S-shaped resonator. Thus we expect significant mutual coupling between these metamaterial elements which results in a broadening of negative effective permittivity or shifting effective electrical resonance toward higher frequencies. Besides, one can implement high dielectric rods (without intrinsic magnetic properties) instead of metal wires. For this configuration, localized displacement currents in the high dielectric rods cannot follow thoroughly the field variations imposed by incident field affecting the coupling efficiency between S-resonators. In other words, the strong capacitance in a high permittivity dielectric would act against mutual coupling of S-resonators. As a result, a red-shift is seen in effective parameters, Figure 4.11.

We proposed a composite metamaterial design composed of a conventional metamaterial and a meta-substrate that is capable of broadening or narrowing the bandwidth of effective parameters. In particular, inserting a conductive rod into the unit cell will increase the bandwidth of the negative permittivity. The addition of more metal rods can eventually shift and suppress the magnetic resonance while shifting the bulk plasma frequency to higher frequencies. Also, high dielectric rods will cause a blue-shift in effective electrical resonance frequency hence narrowing the bandwidth. This combination of effects, now understood, to some extent allows one to design an index value with a prescribed bandwidth [94].

4.2. Polarization Independent Metamaterial

One of the needs in the practical use of metamaterials has been designing a polarization insensitive structure. Here, we propose a 3D metamaterial design which has a polarization-independent transmission spectrum [95]. We start from our conventional S-resonator design and study its respond to change in polarization of normal incident excitation, Figure 4.12.

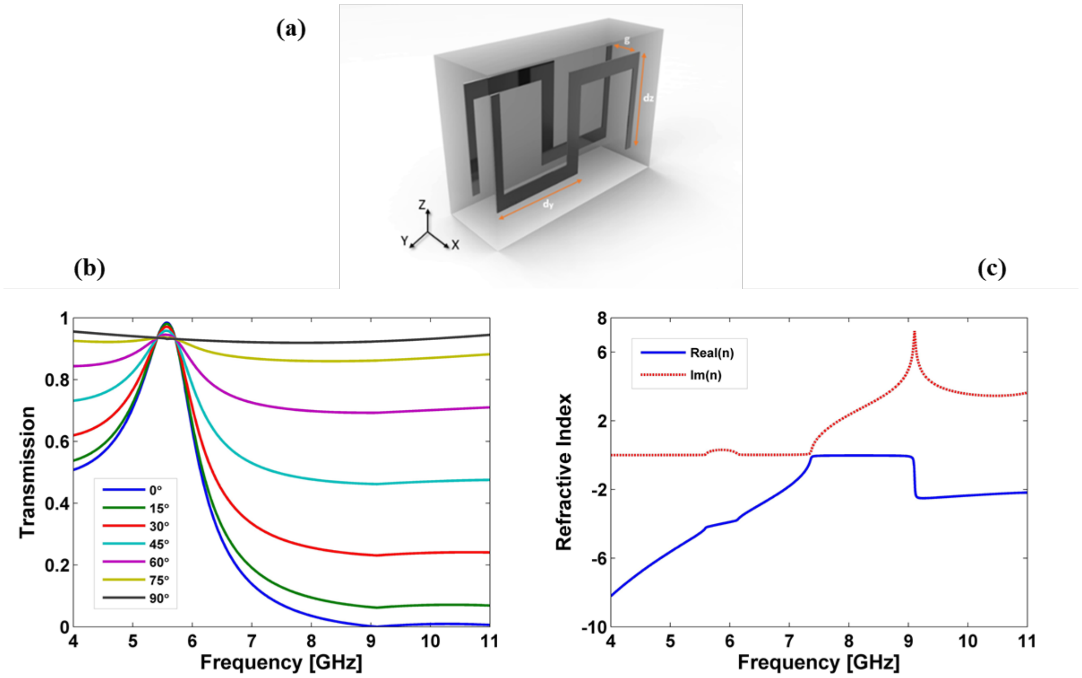

Figure 4.12: (a) Original unit cell design of mirrored S-resonator metamaterials. (b) Transmission spectrum for different angles of linearly polarized normal incident wave (propagation in z) for the case where g=1.5mm. (c) Extracted refractive index of the normal incident for polarization along y. (images are from our published paper [95])

One can achieve negative effective parameters using a double mirrored S-shaped resonator as depicted in Figure 4.12(c), where aluminum is used to make S-features, and they are embedded in a dielectric spacer of polyethylene with ε=2.25. The S-shaped resonator has dimensions of dy=4.18 mm, dz=4.48 mm, g=1.5 mm. The trace width is 0.34 mm for side arms and 0.64 mm for elsewhere, and it has a thickness of 0.04 mm. The mirrored S-resonator is in the center of the dielectric unit cell with dimensions of 3 mm, 8.9 mm, and 6.4 mm in x, y, and z directions. The transmission spectrum of the bulk metamaterial constructed with this unit cell is shown in Figure 4.12(b); a strong magnetic resonance is observed at frequency 5.7 GHz for p-polarization of normal incident excitation propagating along the Z direction, and it disappears gradually by changing the polarization of the incident beam from P to S polarization. Therefore, the constructed structure is birefringent and only exhibits strong left-handed properties for p-polarization of the incident wave; consequently, its spectra depends on the polarization of incoming wave. To improve the design to achieve polarization insensitivity, we can use crossed pairs of mirrored S-resonators to cover both orthogonal polarizations and hence all of their superpositions. To do that, we simulated a series of this element with different lateral periodicity, Λx, using a finite-element solver (Ansys HFSS), and retrieved effective parameters by following a commonly used retrieval process [23]. To design a crossed structure, an optimum lateral periodicity is found where the bulk medium exhibits acceptable negative index in the frequency range of 7.3-8 GHz according to criteria for choosing a correct interpretation of extracted effective parameters [23], Figure 4.13. As it can be seen in Figure 4.13(b), by increasing lateral periodicity of structure, a blue-shift occurs for its strong magnetic resonance which is at 7.3 GHz.

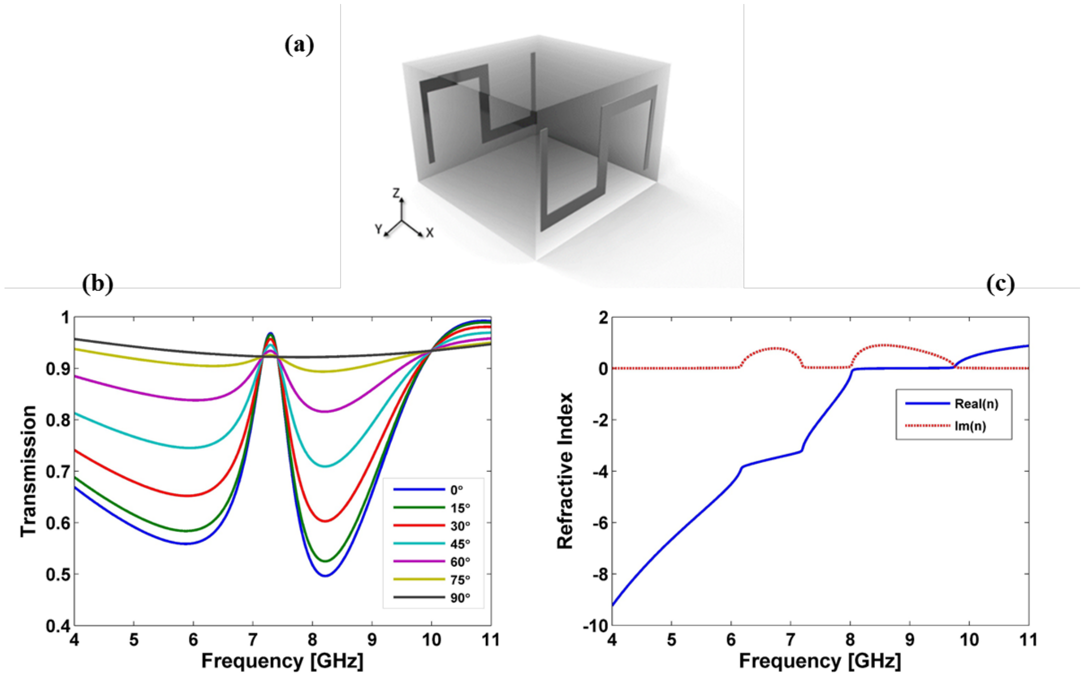

Figure 4.13: (a) Optimum design with a lateral periodicity of Λ_x=8.3 mm. (b) Transmission spectrum for a different angle of the linearly polarized normal incident wave. (c) Extracted refractive index of the normal incident for polarization along y. (images are from our published paper [95])

Arranging pairs of mirrored S-shaped resonators in crossed arrays with optimal lateral periodicity provides a solution to reach polarization insensitivity while maintaining the negative refractive index region. As shown in Figure 4.14(a), the cubic unit cell is embedded in a dielectric host, and its transmission spectrum is common for any linearly polarized normal incident wave, Figure 4.14(b). Also, it represents a negative index region in a frequency range which is physically acceptable, Figure 4.14(c).

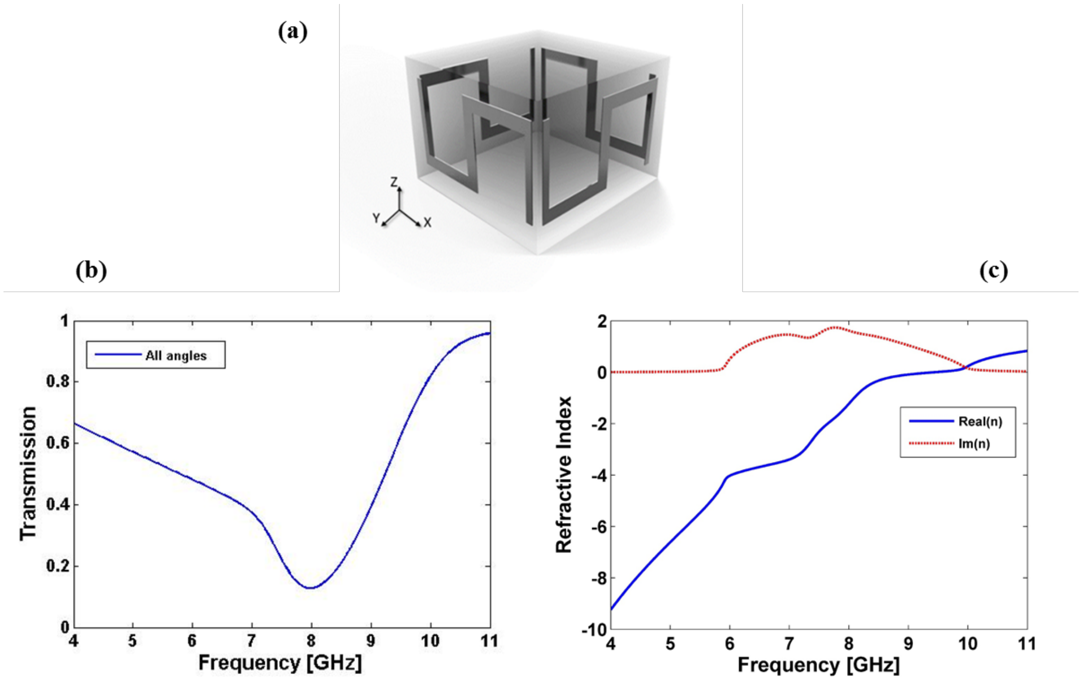

Figure 4.14: (a) Unit cell design of polarization insensitive metamaterial. (b) Transmission spectrum for any angle of the linearly polarized normal incident wave. (c) Extracted refractive index of the normal incident for any linear polarization; the frequency range of 7.2-8.4 GHz is representing valid index values. (images are from our published paper [95])

Fine tuning of the above cubic design shows a significant effect on the transmission spectra as well as the far-field radiation pattern. Here we compare results of two designs of cubic S-resonators with the slight difference in geometry of metal strips, Figure 4.15(a). One design has connected meander line around the cube, and the other one has gaps between the end of S-resonators. The change in the transmission spectra for a slab made of these cubs are displayed in Figure 4.15(b). These plots offer to pick frequencies less than 8 GHz to identify the source design. The method can be used as for various applications such as mechanically tunable filters or sensing applications. An array of a limited number of these cubes also can be used for remote sensing. We calculate the far-field radiation pattern of 4x4 arrays of the cubes, and results for frequencies less than 9 GHz show distinctive patterns for each design which suggest them as potential candidates for passive remote sensing.

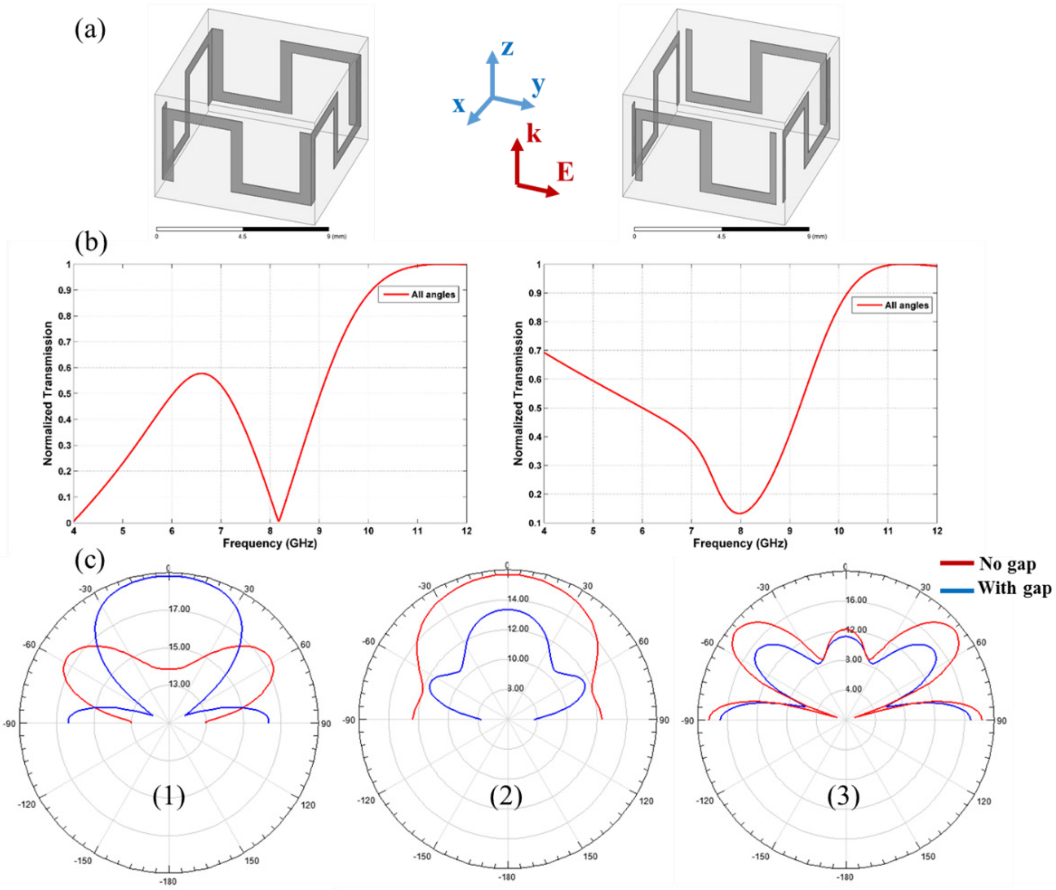

Figure 4.15: Comparison of two cubic designs. (a) connected S-resonators and disconnected designs. (b) Transmission spectra for connected design (left), and disconnected one (right). (c) Far-field radiation patterns for 4x4 arrays of cubes, (1) 7.1 GHz, (2) 8.2 GHz, and (3) 10.2 GHz.

Rapid prototyping using 3D printing technologies are quickly growing in the recent years. This technology offers a robust path to fabricate a lot of sophisticated designs including metamaterials, whereas conventional fabrication techniques are time-consuming and expensive. Our cubic design has interesting features and properties and can be a potential meta-atom for rapid prototyping. Following the interest, we modified the design to fit it within the 3D printing margins while still displaying left-handed properties of the original layout. The proposed designs consist liquid gallium injected in 3D printed dielectric host with a relative permittivity of 2.8 and loss tangent of 0.04. The mirrored S-resonator has a dimension of 7 × 5.5mm with trace cross section of 1.5 × 1.5mm and embodied in the center of the dielectric with a dimension of 11 × 7 × 10.3 mm. The scattering parameters and refractive index are shown in Figure 4.16(a). The cubic version has S-resonators with a dimension of 20.86 × 8.16 mm with trace cross section of 1.5 × 1.5 mm, in the center of a 22.86 × 22.86 × 10.16 mm dielectric cube.

We extract their effective refractive index from calculated S-parameters. These results show negative index regions for both designs with low loss. There are also multiple resonances in cubic design which offer advantages for various applications.

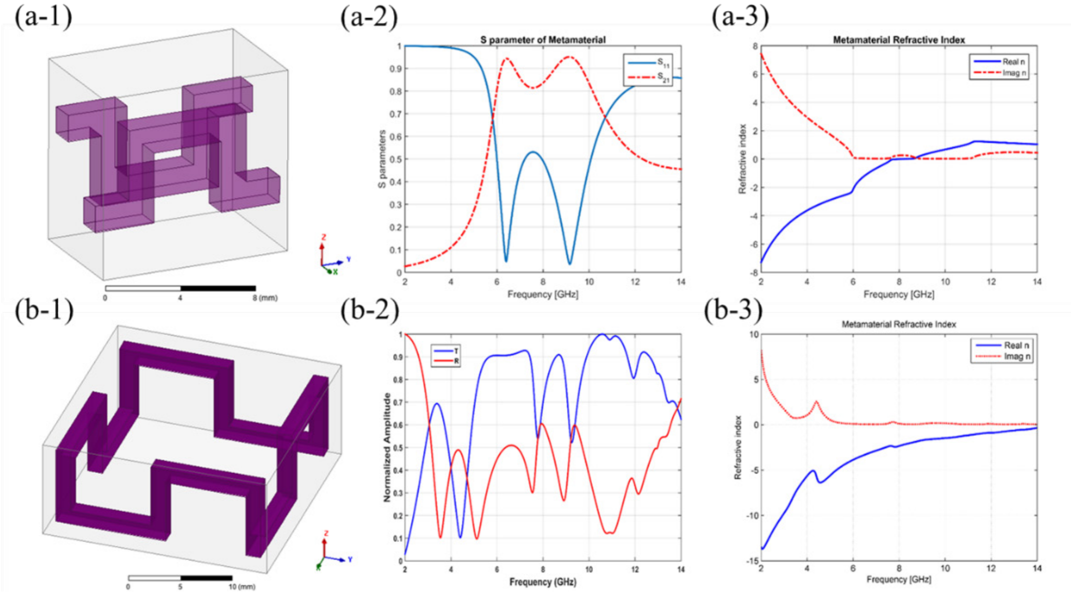

Figure 4.16: (a) mirrored S-resonator unit cell, (b) S-resonator cubic unit cell, (1) 3D printing metamaterials design, (2) their scattering parameters, and (3) extracted refractive index.

4.3. Conclusion

We explored the concept of a meta-substrate as a method for bandwidth engineering of metamaterials. The permittivity and permeability bandwidth can be controlled by inserting additional independent resonators to the design. We also proposed a design for a polarization-insensitive left-handed metamaterial based on conventional mirrored S-shaped resonators. Numerical simulations have been used to demonstrate polarization dependency of structures as well as extracting their effective refractive indices. Considering the materials and geometry, we can fabricate bulk metamaterials based on the design with 3D printing techniques from where it can find practical applications.

CHAPTER 5: NEGATIVE INDEX FOR NEAR-FIELD SUPERRESOLUTION

Conventional imaging systems have a resolution limit enforced by diffraction to half the wavelength of the light source in the imaging sample medium [96]. Despite this, optical microscopes are widely used in biological imaging. Numerous proposed methods are emerging to overcome the diffraction limit and to achieve super-resolved images such as advanced fluorescence microscopy [97]–[99], and super-oscillatory imaging [100].

When an incident wave illuminates the sample, its features with a size greater than the diffraction limit scatter the wave into propagating ones in all directions, and a microscope can collect them. On the other hand, fine features with sizes less than the diffraction limit scatter the wave as evanescent waves that decay exponentially within the scale of the wavelength. The information of sub-diffraction spatial features is included in evanescent waves (high transverse wavevectors) which conventional methods are unable to capture them, and we do not receive their information at the image domain even at the near-field. The evanescent waves or high spatial frequencies decay fast because conventional materials in nature have both positive permittivity and permeability or at least positive values for either of parameters.

However, if one could use a mechanism to transfer the evanescent waves from the object plane to the image plane by increasing their amplitude, diffraction limit could be overcome. To implement such phenomena in a lensing system, it also requires impedance matching between all media in which the light or electromagnetic waves are traveling from the object to the image, so the reflection off the interface boundaries would be removed or minimized. Such a lens is called a perfect lens and has been proposed and studied using metamaterials.

5.1. Pendry's Perfect Lens

A potential candidate material to build a perfect lens is negative index materials. We mentioned in previous chapters that Veselago was the first one who proposed the mathematical foundation for materials with negative refractive index [54]. He predicted negative refractive index in materials with simultaneously negative ε and μ. Subsequently, negative refraction occurs at the interface between positive index medium and negative index medium, and the energy and phase of the beam will flow in the opposite direction in the negative index medium. Later on, Pendry used the idea of negative refractive index metamaterials to propose the perfect lens for super-resolution imaging [101], [102]. However, further studies were limited to the theory since there was no material to build a perfect lens till Smith demonstrated the first negative index metamaterial using split-ring resonators with metallic wires [9], [68]. Following then, other works used SRR structures to realize negative refractive index at microwave frequencies [16], [103], [104]. Thanks to these improvements in metamaterials, a wider range of applications have emerged using metamaterials including spontaneous emission enhancement [105], transformation optics [106], novel waveguides [107], and super-resolution imaging [108]–[110].

In his work, Pendry suggested that a negative index slab with $\varepsilon = \mu = -1$ in the air acts as a perfect lens. This lens of negative index material can amplify and transfer decaying high spatial frequencies from the object plane to the image plane, and therefore we can reach resolutions better than ones restricted by the diffraction limit. According to the theory, the lens slab has a perfectly uniform refractive index of -1, but in practice, it is not feasible to make such a perfect lens, and the question would be how much resolution we can achieve using the partially "perfect lens." Another characteristic of a perfect lens is the relation between the slab thickness and the distance between the object plane and the front face of the slab as well as the distance between the image plane and the exit face the slab. Assuming the lens slab has a thickness of d, the entire object, and image distance from the lens should be the same as slab thickness. Figure 5.1 illustrates this concept in a perfect lens where x is the object plane distance from the slab surface in object domain and $d-x$ is the image plane distance from the slab surface in the image domain. To meet the requirement mentioned before, $x+(d-x)$ should be equal to d.

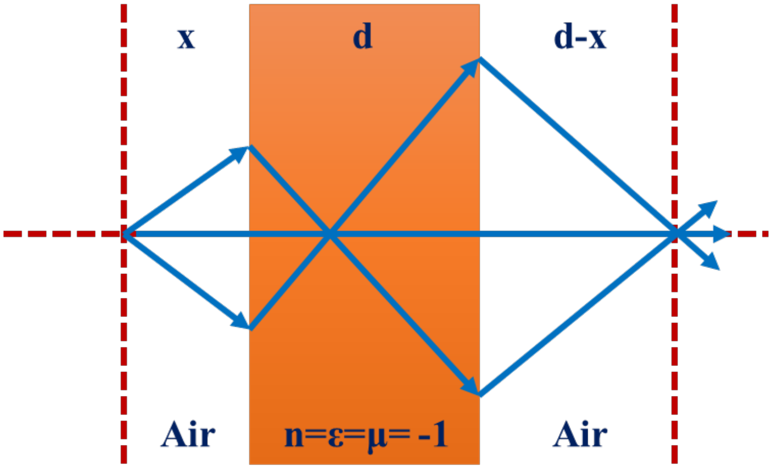

Figure 5.1: Schematic of a slab of a perfect lens.

To achieve a super-resolved image, the object must be located in the near field of the negative index material so the exponentially decaying evanescent waves which are carrying high spatial frequencies can couple through the negative index medium, and their amplitude becomes resonantly enhanced, Figure 5.2. It should be mentioned that this field enhancement could take a relatively long time when we are seeking higher resolutions [111]. A negative index metamaterial has a narrow bandwidth and is lossy which will truncate the transfer function of a metamaterial lens, and even a small amount of loss can decrease the amount of captured evanescent waves and eventually degrades the quality of the image [112]–[117]. However, an image with a resolution of around λ/5 would be useful in many applications such as in biological imaging. In general, a metamaterial couples high spatial frequencies information from the object domain to the image domain, and these high spatial frequencies contain information of the object in subwavelength scales [118].

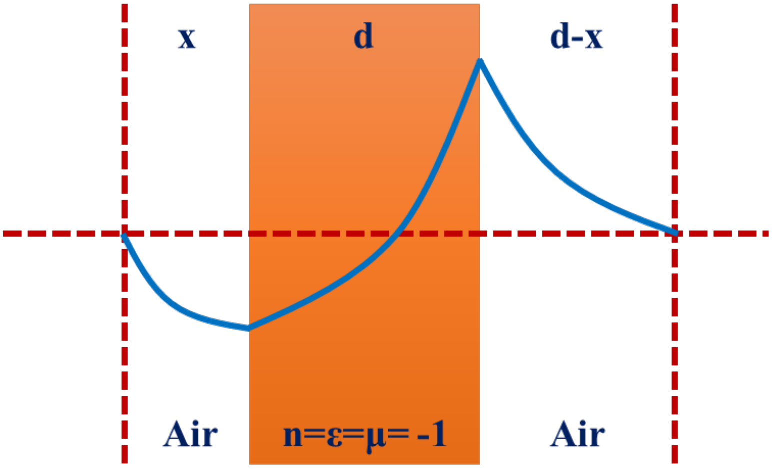

Figure 5.2: Fields of high spatial frequencies decay exponentially in object domain and resonantly enhanced in lens medium and can be transferred into image domain to construct the image.

The responsible phenomenon for this amplification of evanescent waves is surface resonances [101], [119]–[122]. Surface plasmons, oscillation of electron density, are generated when the incident waves enter an interface between media with opposite sign of permittivity. Now if wavevectors of evanescent waves and surface plasmons are matched, there will be resonances on the surface propagating along the interface while their amplitude decays exponentially. These surface waves, also called surface plasmon polaritons (SPPs), have shorter wavelengths than the incident wave and confine their energy to a subwavelength scale which can significantly enhance the localized field intensity. Now if the perfect lens slab is thin enough, these surface resonances couple from the front interface to the exit interface of the slab; then in the process, the evanescent wave are amplified, and they enter to the image domain.

We perform a simulation to represent this concept. A 2D negative index slab, 4x6 μm, is designed in Lumerical using Lorentz model, so it has a refractive index of -1 and a loss of 3.3e-5 at the wavelength of 512 nm, Figure 5.3(a). A point source, magnetic dipole, generating signals at 512 nm is placed in front of the slab at 2 μm from the front face of the slab.

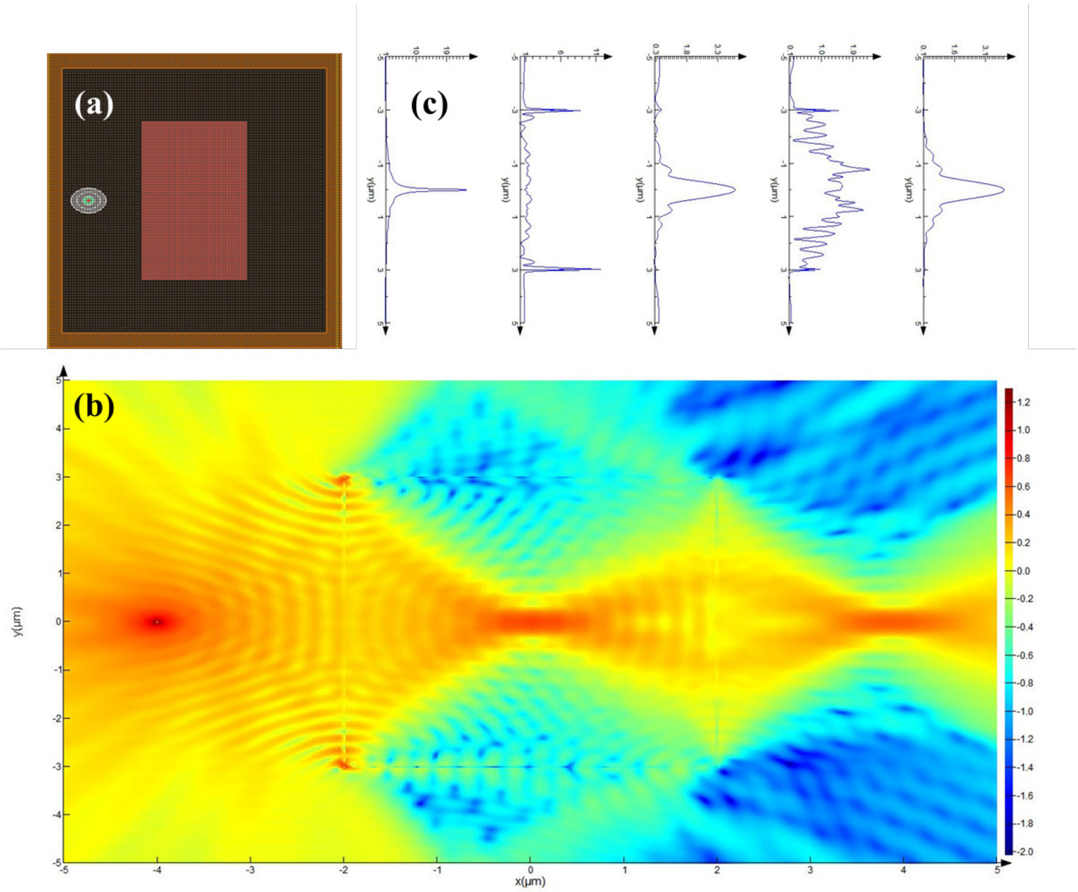

Figure 5.3: Surface resonances in a perfect lens. (a) Simulation setup of a perfect lens and point source as the object enclosed in PML boundary conditions; (b) Field magnitude distribution and existence of surface waves; (c) Field intensity plots along propagating direction at different locations, from left to right: in the point source plane, on the front face, in the middle, and on the exit face of the slab as well as in the image plane.

The field magnitude distribution is shown in Figure 5.3(b), where an image is constructed at the distance of 2 μm from the exit face of the slab. Here, we clearly notice the presence of the surface waves and their coupling to the exit face of the slab. In addition, the field magnitude is plotted at multiple locations in the simulation setup including the field at the source point plane, on the front face of the slab, in the middle of the slab, on the exit face of the slab, and at the image plane, Figure 5.3(b), the surface waves are observed in these plots at the front and exit face of the slab. The larger image spot compared to the point source is due to multiple reasons; one is that the source is not practically a single frequency source but rather a very narrow bandwidth wave source, and also the negative index slab is dispersive, so there is a chromatic aberration. Another similar reason is that different high spatial frequencies of evanescent waves originated from a single frequency are focused at multiple locations since the slab is dispersive.

We run some more simulations using this homogenous negative index slab setup to inspect surface waves. We change the setup dimension by increasing the slab height to 18 μm with a thickness of 2 μm, while the point source is at 0.5 μm distance from the front face of the slab. Figure 5.4(top) displays the field distribution for this case. We can observe the high concentration surface waves on the front interface, and how the evanescent waves have been amplified and coupled to the back interface. Reducing the slab thickness has a significant effect on improving surface waves and their couplings between interfaces, Figure 5.4(bottom). Here, the slab thickness is 0.5 μm, and the point source is moved to 0.25 μm of the front face.

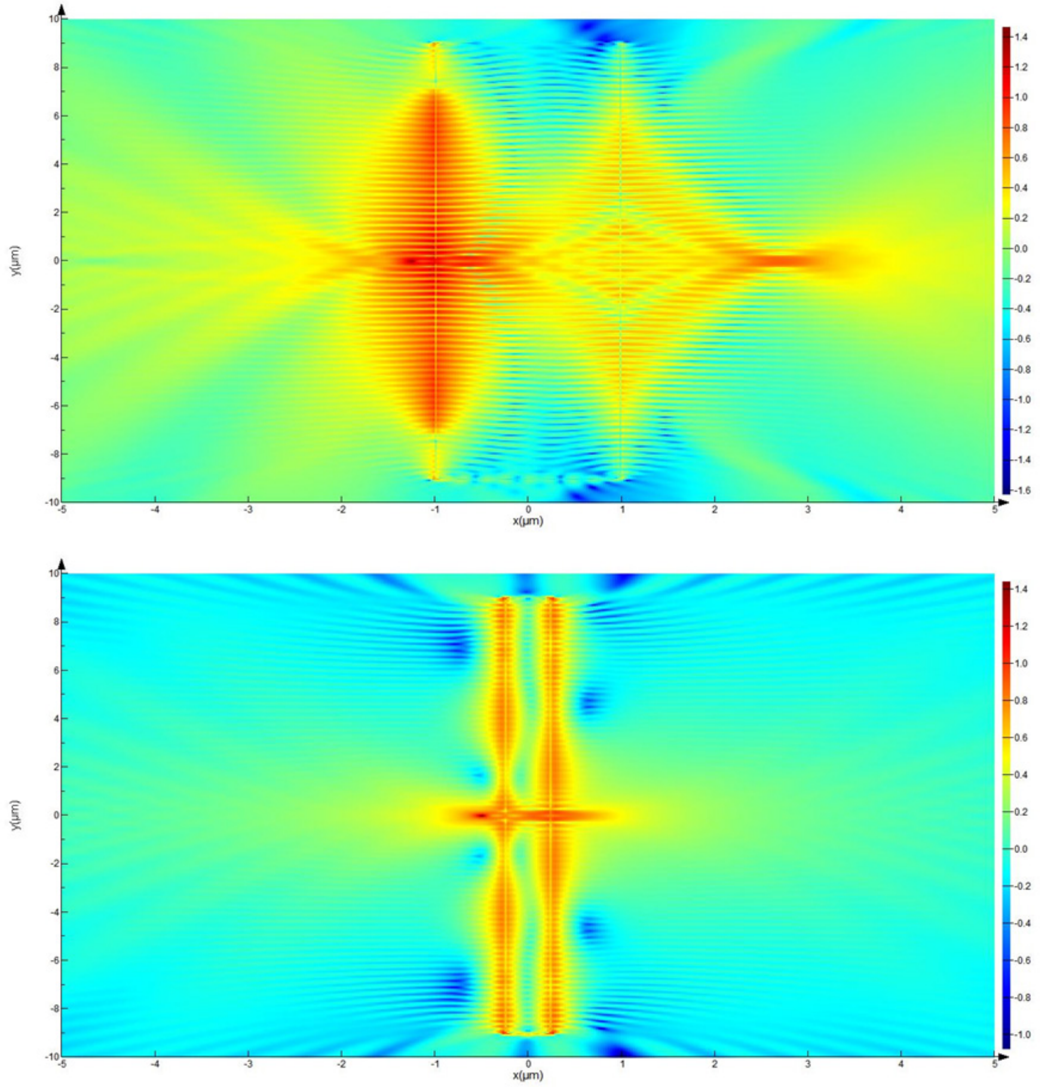

Figure 5.4: Field magnitude distribution of a point source in front of a negative index lens.

5.2. Debates on Pendry's Perfect Lens and Alternatives

There are ongoing discussions on whether the phenomenon of perfect lensing is possible in theory [123]–[126]. The arguments are on the possibility of achieving such super resolutions with the presence of loss in the slab as well as the fundamental restrictions caused by causality which prevent to achieve a perfect lens from super-resolution imaging [127], [128]. In reality, there are many complexities in fabricating a super resolution imaging system using a negative index slab. One of the major obstacles is that building a low loss metamaterial to transfer evanescent waves into the image domain is very challenging. These issues have been addressed thoroughly in [129], where the sensitivity of image resolution comes from the granularity of the meta-atoms, the finite dimensions of structures, and optical isotropy of the array. When working with finite sized structures, the arrangement of the meta-atoms, their mutual couplings, and scattering between them can make designing an effective homogenized refractive index close to the desired value of n = -1 very difficult [43], [130]. Therefore the image quality would not be sufficient enough, but still by having transfer matrix of the metamaterial lens, one can use computational image reconstruction to have a better image quality [131]. It also has been shown that using only random medium instead of a lens can improve image resolution through the scattering process [132]. Another significant problem arising in the near field is the evanescent waves couplings between the object, metamaterial lens, and the detector which degrade the image quality [133]. Likewise, the periodicity of meta-atoms and lens surface roughness will also contribute to the generation and scattering of evanescent waves [134].

Engineering evanescent waves and transferring them to the near-field is still a significant challenge at visible frequencies due to difficulties in nanofabrication technologies as well as limitations in properties of available optical materials. Researchers are working to find alternative materials with desired properties such as low loss at visible frequencies, implementing smarter designs, and improving fabrication techniques to achieve a better super-resolved image at optical frequencies using metamaterials.

Beyond Pendry's perfect lens, in recent years there have been other approaches to achieving a perfect lens. One method uses a pair of phase-conjugating interfaces to produce the boundary conditions of a negative index slab [135]–[138], this approach requires the existence of nonlinearity in the system to generate negative refraction [139], [140]. Another technique is based on parity-time symmetry; here a pair of metasurfaces are used to obtain super-resolution imaging while the gain is introduced in the metasurfaces to avoid the nonlinearity requirement [141], [142]. A more recent work introduces a double-interface lens composed of a dielectric and a passive lossy metamaterial to obtain super-resolution imaging [143].

5.2.1. Super Lens

Although an ideal perfect lens requires both $\varepsilon = \mu = -1$, under certain conditions a super-resolution lens can be realized with either only $\varepsilon = -1$ or $\mu = -1$. This quasi-perfect lens is called a superlens. The reason that super lens works is that at the near-field when scales are in the subwavelength region, the electric and magnetic fields are decoupled and evolve independently. Therefore, a specific polarization from the object domain can be transferred and super-resolved in the image domain with either negative permittivity or permeability for the perfect lens slab. Because metals have negative permittivity at frequencies less than their natural plasma frequency, researchers used very thin silver films at the UV frequencies to achieve super-resolution imaging [144]. However, yet the relatively high loss in metals at visible frequencies substantially degrades the quality of the image. There are multiple approaches to managing this problem such as methods to reduce losses in metals [145][146], using alternative materials instead of metals such a graphene or semiconductors [147]–[150], or introducing gain in the lens to compensate for losses [151]. Another issue in obtaining super-resolved images in near-field super lensing is the slight gap between the superlens and the image plane due to practical difficulties in retrieving the image at such short distances. A solution to this is converting the evanescent waves into propagating ones at the exit face of the superlens using techniques such a patterned grating on the superlens surface [152][153][154].

5.2.2. Hyperlens

Hyperlens as a highly anisotropic structure with hyperbolic dispersion is another tool to reach sub-diffraction imaging. Hyperbolic metamaterials or anisotropic meta-atoms can be used to make a hyperlens. In a hyperlens, incoming waves encounter permittivity (or permeability) with opposite signs depending on the propagation direction. In other words, the permittivity along the perpendicular and parallel direction on the anisotropic axis has opposite sign. A structure with such an anisotropic permittivity tensor behaves like a dielectric in one direction (positive permittivity), and metal in the other direction (negative permittivity).

Hyperbolic metamaterials have a hyperbolic dispersion [155], [156]. This characteristic of them allows distinctive applications such as enhancement of spontaneous emission [157], [158], high photonics density of states [105], thermal engineering [159], [160], and of course super-resolution imaging [161].

Hyperlens was first theoretically analyzed in 2006 [162]–[164], where multilayer stacks of dielectric and metal are designed in a cylindrical shape, so the evanescent waves in the near field are collected in the object domain and transferred into propagating wave toward the far-field in the image domain. Following the theory proposal of hyperlens, their experimental realizations were shown in different frequency ranges such as the UV [165], [166], visible [167], [168], or microwave [169].

5.3. Evanescent Waves in Negative Index Materials

In this section, we explain the evolution of evanescent waves in a negative index material in more detail. We assume that the interface between air ($z < 0$) and the negative index slab ($z > 0$) is parallel to the x-axis, and the XZ plane is the principal plane containing the propagation vector $k=(k_x,k_z)$ and the normal to the interface. When $k_x<|k|$, k_z is a real number, and the plane waves of $\exp[i(k_x x+k_z z-\omega t)]$ are propagating waves. When $k_x>|k|$, k_z is an imaginary number, and the plane waves of $\exp[i(k_x x+k_z z-\omega t)]$ are evanescent waves. To proceed, we can limit our argument to only S-polarized incident waves since the treatment of P-polarization is similar and its conclusion is identical. Using the same notation for electric fields as in [101], it leads to the electromagnetic field boundary conditions,

$$\begin{gathered} 1 + r = t \\ -\mu k_z + \mu k_z r = -k_z' t \end{gathered} \tag{5.1}$$

where r and t are field reflection and transmission coefficients. From above equations we can conclude that,

$$\begin{gathered} t = \frac{2\mu k_z}{\mu k_z + k_z'} \\ r = \frac{\mu k_z - k_z'}{\mu k_z + k_z'} \end{gathered} \tag{5.2}$$

For an ideal metamaterial slab of n=-1, with ε=μ=-1, k_z=k_z', Equation (5.1) leads to,

$$\begin{gathered} 1 + r = t \\ 1 - r = -t \end{gathered} \tag{5.3}$$

which appears self-contradictory and leads to infinite transmission and reflection coefficients in Equation (5.2). Pendry resolved this singularity by finding a sum to the diverging infinite series. The results describe that the transmission of evanescent waves through the perfect lens is amplified with the gain exp($|k_z|d$), where d is the slab thickness. However, assuming that the negative index material is necessarily dispersive and lossy, $\varepsilon^" \neq 0$ and/or $\mu^" \neq 0$, we can conclude that,

$$k_z'^2 = \left(\varepsilon' + i\varepsilon^"\right)\left(\mu' + i\mu^"\right)\left(\frac{\omega}{c}\right)^2 - k_x^2 \tag{5.4}$$

where ε' and ε'' are real and imaginary parts of ε, and μ' and μ'' are real and imaginary parts of μ. Since k_z' is now different from k_z, the singularity in the transmission and reflection coefficients is removed. In addition, to satisfy causality, the imaginary part of k_z' is positive. Therefore,

$$\mathrm{Re}(k_z')\mathrm{Im}(k_z') = \frac{(\varepsilon'\mu'' + \varepsilon''\mu')}{2}\left(\frac{\omega}{c}\right)^2 \tag{5.5}$$

When the imaginary parts of ε and μ are not simultaneously zero, then both real and imaginary parts of k_z' are non-zero and, the evanescent waves in air are transformed into decaying propagating waves with the propagation direction given by

$$\theta = \tan^{-1}\left(\frac{k_x}{\mathrm{Re}(k_z')}\right) \tag{5.6}$$

where θ is the angle between he propagation direction and the normal to the interface. As a result, evanescent waves with different spatial frequencies k_x will have different propagation direction in the negative index medium. But sill we have to keep in mind that if the thickness of the metamaterial slab is in the order of several wavelengths, then these decaying propagating waves in the metamaterial will still be lost.

In the case of our S-resonator structures, we study how evanescent waves transfer through. A finite size bulk metamaterial composed of two successive rows of S-resonators in the propagation direction and 15 of them in the transverse direction is excited by an incident purely evanescent wave with E_0 field along the z-direction. Figure 5.5 shows the E-Field magnitude plots for different frequencies. As it can be seen in the frequencies in which a negative index for the metamaterial was calculated, evanescent waves excite the S-resonators, and they have been converted to propagating waves via resonances and mutual couplings inside the bulk metamaterial. For frequencies which refractive index is closer to -1, there are stronger interactions between evanescent waves and S-resonators. Simulations suggest that the mechanism of converting the evanescent waves into propagation ones is similar to the antenna mechanism.

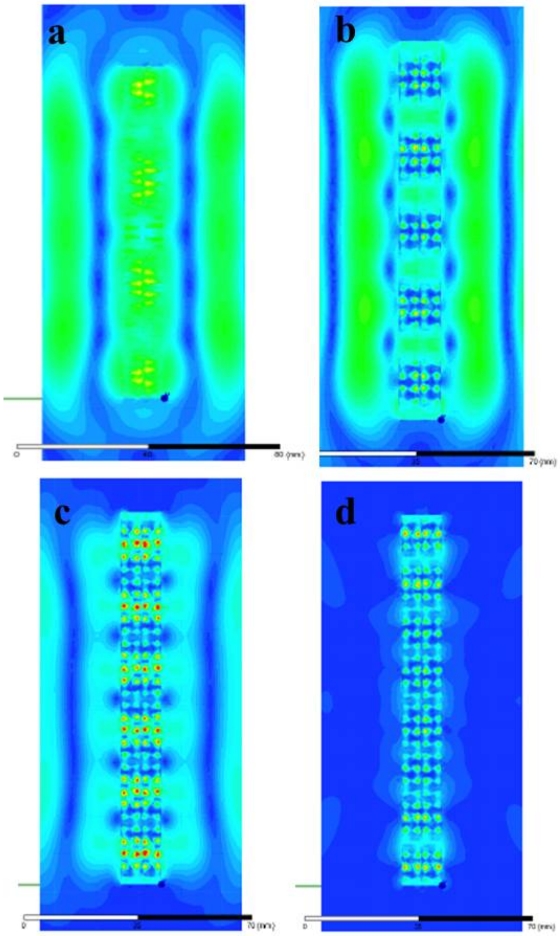

Figure 5.5: Side view from middle of the S-resonators slab while an incident evanescent wave illuminated the structure; a) 7.6 GHz, b) 8.4 GHz, c) 9 GHz, d) 9.6 GHz

5.4. Compressive sampling

Since it is very challenging to analytically describe a finite size metamaterial slab and its imaging properties; therefore, we have studied numerically and experimentally the fields obtained in the image domain from a series of slits in a metal mask, positioned close to the surface of a negative-index metamaterial composed of subwavelength S-resonators. We employed only two columns of S-elements in the propagation direction to minimize the loss effect in the structure, and also 15 rows in the transverse directions. Figure 5.6 illustrates the metamaterial lens and the aluminum double-slits mask which is the object used to simulate the system. In experiments and simulations, we inserted FR4 dielectric sheets between S-resonators sheets, so we expect the negative index n=-1 to be around 7.3 GHz as previous calculations suggest. Also, the mask is thin enough compared to the incident wavelength that we can consider the mask as a 2D object, and therefore we do not need to concern the effect of object size along the propagation direction. The whole system is enclosed in an air box which the perfect boundary condition applies to its sides, so then all incoming electromagnetic waves would be absorbed on air box sides and make the lens and the metal mask as a stand-alone system. A plane wave with wave vector along +x-direction (green axes) and has E_0 field along z-direction is used to excite the system. Also, the size of air box has been chosen in a way to satisfy HFSS requirement for an accurate simulation.

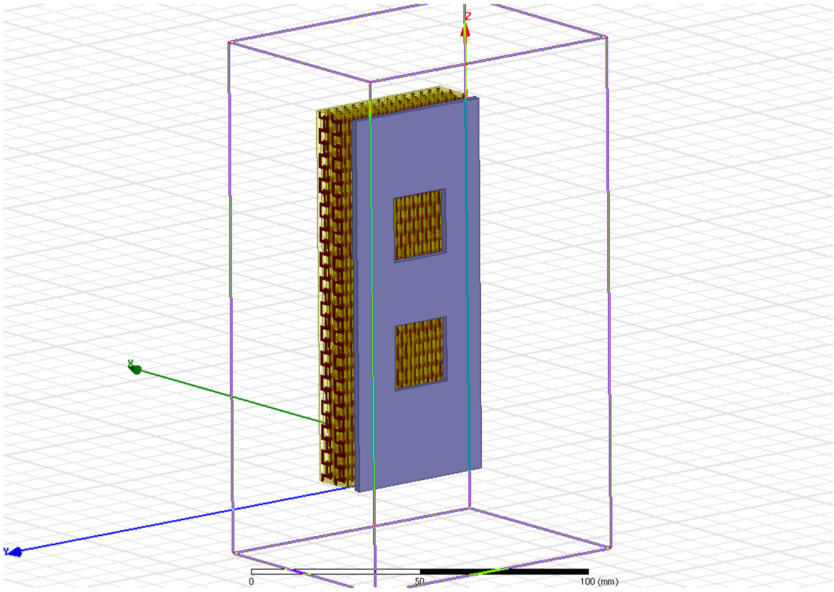

Figure 5.6: Metamaterial lens slab and the double-slit metal mask enclosed by an air region box.

On the left of Figure 5.7, it shows a simulation of the scattered field, and on the right, there is a plot of a measured field amplitude in the image plane if n = -1. Because the image has been influenced by finite-size consequences of lens slab, one might use computational image processing as a necessary tool to determine the structure of the mask by addressing the associated inverse scattering problem [170]. Because of fabrication and positional tolerances, and also the fact that the S-resonators are only approximately λ/5 in size, we cannot expect a better than λ/5 resolution even assuming no losses in metamaterial structure. From experiments, the evanescent wave transfer appears to lead to features in the measured image down to this resolution and possibly smaller, but the metamaterial loss has modified the phase (as well as the amplitude) of these higher spatial frequencies.

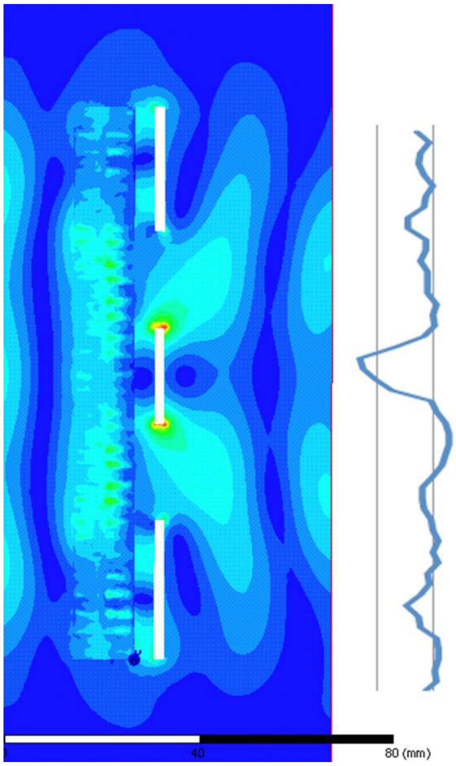

Figure 5.7: Simulation of incident wave onto a double-slit mask and metamaterial lens where incident wave is from right (left) and measured field on the image plane (right)

5.5. Conclusion

We studied the transfer of evanescent waves through mirrored S-resonators metamaterial. Although in simulations and experiments there is some evidence of subwavelength imaging up to λ/5, we cannot expect better resolution due to the size of meta-atoms and the existence of losses which significantly degrades the quality of images. To overcome this obstacle, one can use image processing tools such a compressive sampling to obtain the super-resolved image.

CHAPTER 6: RECIPROCITY SENSING AND IMAGING

Retrieving an image from scattered fields is a complex and nonlinear process, and scattering approximation techniques can be used to simplify it such as Born or Rytov approximations. Type of illumination and the number of scattered fields measurement control the quality of the reconstructed image. Even in this case, the resolution is limited to about λ/2 where λ is the wavelength of the illumination source. However, through multiple scattering phenomena, one can achieve better resolutions [171]. On the other hand, increasing number of measurements by a finite amount results in an infinite uncertainty in the image reconstruction, and to avoid the ambiguity; different inverse scattering algorithms have been proposed to choose the optimal image according to embedded criteria. These methods use prior information about the scattering object to modify degrees of freedom in the system to enhance the quality of the output where a significant amount of effort has been delivered toward super-resolution over the last half century [172]. The proposed approaches are for achieving super-resolution information in the near field, but it would be more practical to drive it with far-field data.

The trade-off mechanism in the inverse scattering algorithms is between the calculated number of degrees of freedom in the scattering experiment [173] and the ultimate resolution [174]. The trade-off mechanism in the inverse scattering algorithms is between the calculated number of degrees of freedom in the scattering experiment and the ultimate resolution. These constraints, in a similar fashion, are essential in the design of metamaterials with subwavelength structures, and when these subwavelength features are in the scattering medium, one can calculate effective material properties and then far-field scattering patterns. Following this idea, there is a connection between super-resolution using time reversal and negative index metamaterials [137]. We further extend this argument to incorporate generalized reciprocity principles to design complementary scattering metamaterial structures that might allow super-resolution through direct far-field information without field computing techniques such as time reversal.

Fink et al. performed one of the promising experiments using time reversal, obtaining a super-resolution of λ/30 for two sources of λ which were separated by λ/30 and surrounded by a subwavelength strongly scattering structure [175]. In their setup, the propagating scattered field was detected in the far-field using an array of antennas. Then a time reversal procedure was performed on collected signals, and the result was emitted back through the antennas toward the sources embedded in the strong scattering medium composed of subwavelength wires. High spatial frequencies or evanescent waves were recreated in this event within the subwavelength-wire structure ultimately confining the returning waves to their origin sources. Inspired by this experiment, we considered a similar setup with removing the need for time reversal computing process which includes detection of the signal and rebroadcasting after time reversal. A subwavelength metamaterial structure serving as a strong scattering medium would convert evanescent waves into propagating ones and encode high spatial frequency information in far-field waves. With having the design of the metamaterial encoder, one would be able to design a complementary structure to decode the propagating waves in the far-field. We study the necessary properties of such structure to achieve this direct method for image reconstruction. Assuming to conduct the experiment in free space, we need a metamaterial structure with an effective index close to unity, positive and negative, to avoid Fresnel reflections which disturb the multiple scatterings essential for evanescent modes conversion. The role of losses would be significant. Therefore there needs to be a distinction between reciprocity, time reversal and phase conjugation with and without losses. We will emphasize on this concern in the next section.

6.1. Reciprocity in Electromagnetism

In the propagation of waves, reciprocity means the symmetry of the propagation under the interchange of the observer and the source [176]. To expand this definition, assume a time-invariant and linear electromagnetic system with a source at S and a detector at P where EM field is measured. According to reciprocity, by switching the location of the source and the detector, the received electromagnetic field at S should be closely related to the previous measurement at P. We have studied applications of the generalized reciprocity theorem to design complementary metamaterial structures with strong scattering. To realize reciprocity, the dielectric tensors of the structure have to satisfy certain symmetry conditions. When only lossless media is involved, time reversal and reciprocity are equivalent, and they are related to CPT symmetry and the Lorentz invariance of EM fields, [177], [178]. According to Lorentz's theorem, we can drive reciprocity relations in a medium with complex dielectric tensors, i.e. with the presence of loss. Therefore, time reversal process would be realized. On the other hand, S-matrix techniques demonstrate reciprocity with or without evanescent modes, and this is equivalent to the case of time reversal when there is no loss, [179], [180]. Hence, reciprocity in the presence of losses is possible, but it would not be invariant under time reversal.

In magneto-optic materials with the loss, the constitutive tensors are not symmetric or Hermitian. However, we can still realize Lorentz reciprocity by having ($\mathbf{J}_1$, $\mathbf{E}_1$) and ($\mathbf{J}_2$, $\mathbf{E}_2$) in separate systems whenever ($\mathbf{J}_1$, $\mathbf{E}_1$) holds Maxwell's equations at ω with material tensors of ε_1 and μ_1, and ($\mathbf{J}_2$, $\mathbf{E}_2$) satisfies the EM equations at ω with material tensors of ε_1^T and μ_1^T, where T represents transpose [181]. As it was mentioned before, there is a close connection between the negative index and time reversal [137], and this link has been demonstrated experimentally by Katko's group [182]. Superresolution imaging with a negative index lens can be described with multiple scattering of a phase conjugate wave including time reversal [183]. By introducing gain in this system to compensate for losses, all evanescent and propagating waves remain unchanged under reciprocity. However, in practice, sufficient gain is hard to hold to obtain the reflectivity of unity. Also, fabrication of a metamaterial with a negative index of -1 is tedious.

In the following sections, we introduce some metamaterial designs to generate scattered propagating fields which are phase conjugates of each other and link them to reciprocal scattering and time reversal. Moreover, their applications for remote imaging are investigated.

6.2. Metamaterial Encoder & Decoder

The creation of evanescent waves, high spatial frequencies, due to multiple scattering and their effects on far-field radiation has been studied for some time [184], and been considered as a means for obtaining high-resolution images assuming a reliable inverse scattering algorithm can be applied. To involve properties of metamaterials in such scattering systems for super-resolution, we relate to the link between negative index metamaterials and phase conjugation which was proposed by Pendry [137]. As we stated before, phase conjugate is equivalent to time reversal in the general condition, and from this concept, multiple high-resolution experiments were conducted based on measuring far-field information following time reversal of signal and sending them back to the source they were emitted [175].

According to our approach, a carefully designed metamaterial can act as a strong scattering medium to convert high spatial information within evanescent waves into propagating ones which will be measured at far-field. Then this metamaterial serves as an encoder. In the measurement site, a complementary structure of the first metamaterial serves as a decoder which converts the waves into near-field information. In this case, there is no requirement in the intermediate detection of the field and numerically calculating its time reversal. The complementary structure remotely delivers reconstruction of scattered waves to recover high-resolution data. A generalized reciprocity theorem is used to design the complementary metamaterial structures [185]. To realize reciprocity, the dielectric tensors of structures must satisfy certain symmetry including the presence of negative values for permittivity and permeability, and this explains our interests in negative index metamaterials for this purpose.

Our previously designed S-resonators structure is a potential candidate metamaterial for this task. It contains discrete subwavelength structures which are strongly scattering due to their resonant properties. These tiny antennas have close electrical and magnetic resonant frequencies giving an effective negative index at a specified frequency. The retrieved effective refractive index of this structure shows an index of n=-1 at about 7.5 GHz, Figure 2.8. The S-elements couple to the incident near field and scatter them strongly resulting in the generation of evanescent waves and consequently conversion of them into propagating waves. The possibility of generated evanescent waves with highest spatial frequencies depends on inherent losses of resonant behavior in the metamaterial which ultimately determines the possible high-resolution to achieve.

The general scattering theory can describe the process of this complex scattering as shown in Equation (6.1),

$$\begin{aligned}\Psi_{scattered\,field} &= k^2 \int_D V(\acute{\boldsymbol{r}}) e^{-ik\hat{\boldsymbol{r}}.\acute{r}} \Psi(\acute{\boldsymbol{r}}, \hat{\boldsymbol{r}}_{inc}) d\acute{\boldsymbol{r}} \\ &= \Psi_{weak\,scattering} + \Psi_{refraction} + \Psi_{dispersion+diffraction}\end{aligned} \tag{6.1}$$

the scattered waves in far-field, $\Psi_{scattered\ field}$, respresented as an integral of the scattering function expressed in the far field as the integral of the scattering function, $V(\boldsymbol{r})$, over the total field in the medium volume. The general description on scatetring icludes separte componens which each are relavant to distinct scattering phenomena. Each single meta-atom contributes to scattering of the incident field with different output due to fabrication tolerance. This is shown as the weak scattering term. Then a portion of scattering arises from the effective proprties of the structure leading to negative index refraction in this case. The last rem corresponds to dispersion and diffraction phenomena caused by periodicity in the strucutre when the periodicity is in the order of incident wavelength, $\Lambda \sim \lambda$. Even though subwalength meta-atoms and their priodicity implies a $\Lambda < \lambda$, still there can be significant scattering arising from the priodicity in the medium. This is because diffraction is strong when $1/k = \lambda_{\mathrm{eff}}/2\pi$ which this condition can be determined by plotting the dispersion diagram (ω vs. k) to find any band area [44].

Although negative index metamaterial is promising in achieving super-resolution from far-field information, realizing such structure with negative constitutive parameters needs a high resonant energy storage which takes a significant amount of time to build up and is very sensitive to losses in the structure [186]. However, they present a reconstruction of scattered fields through phase conjugation and without physical or numerical time reversal process only by the right design of structure compared to holographic or nonlinear processes to achieve phase conjugation [187]. Metamaterial designs which generate scattered fields, phase conjugates of each other, are intimately associated with Babinet's principle where a 2D diffracting surface and its complement design produce scattering radiation patterns which by summing together yield the original incident beam, in other words, the radiation patterns from each surface scatterer have the same magnitude but opposite in phase [53], [188], [189].

6.3. Numerical Simulation of Reciprocity

Figure 6.1(a) illustrates the concept of reciprocity with a metamaterial and its complementary design. The metamaterial structure **M** converts high-resolution field **a** to **b,** and the reverse happens when **b** propagates through and is scattered by $\mathbf{M}^{C}$, as a complementary metamaterial, to reproduce **a**. A simulation of the ideal condition regarding field patterns is shown in Figure 6.1(b).

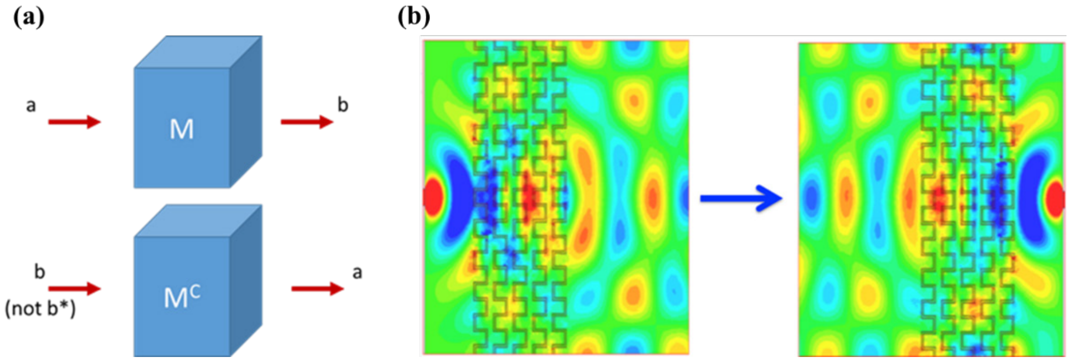

Figure 6.1: a) Encoder medium M and decoder medium Mc. b) Propagation through n = -1 and then n = +1 S-element metamaterials.

There is a challenge to choose a metamaterial design that converts the highest spatial frequencies into propagating waves. However, if the complementary structure has the negative index of the original index with the same thickness along propagation direction, then the pair together form an effective “negative space” which means the combination of the metamaterial and its complementary design, if perfect in their properties, would produce a wavefront identical to the original incident field [137].

To find the proper metamaterial design, we need a structure which its small-scale scattering terms, $\Psi_{weak\ scteering} + \Psi_{dispersion+diffraction}$, are similar to the complementary design, but they exhibit different refraction, $\Psi_{refraction}$. For this purpose, tuning the freuqency at which the metamaterial has a negative/positive refractive index is essential. In the S-resonators design, we can tune this frequency by changing the permittivity of the substrate while the physical size of the S-elements are unchanged. A demonstration of this idea is shown in Figure 2.16. A problem of this technique is the change in the effective wavelength, λ_{eff}, when the permittivyt of the substrate is altered. This prevents to achieve a perfect reciprocity, but perhaps the margine would be close enough to extract useful high-resolution infromation.

A simulation was conducted with a pair of adjacent perfect metamaterial slabs, and results are illustrated in Figure 6.2, on the left. The slabs are homogenized mediums with indices of n = +1 (top slab) and n = -1 (bottom slab), and with the same thickness to demonstrate a negative space in free space. We notice that the emerging field at the lower face of the bottom slab is identical to the field entering at the front face which is an indication of negative space. The similar simulation setup was performed with S-resonators which is shown in Figure 6.2, on the right. This illustrates the approximation of the perfect negative space using finite-sized S-resonators. Although there is no phase change seen, the same behavior is observed qualitatively.

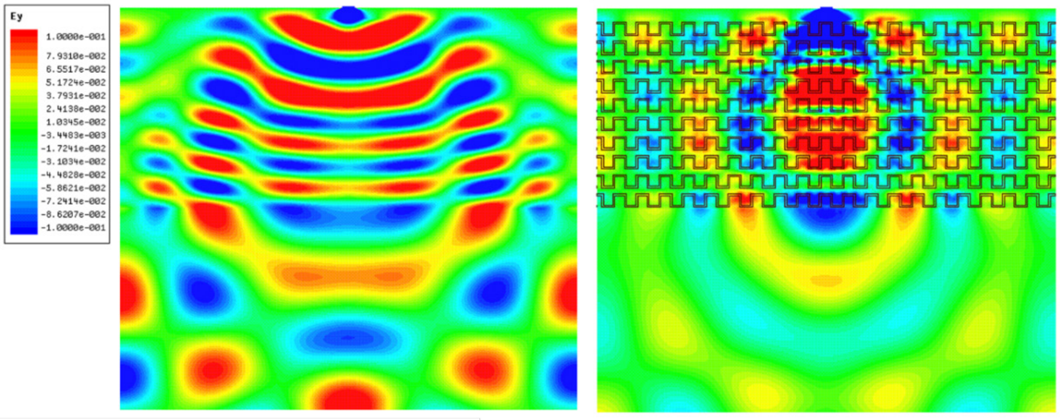

Figure 6.2: A comparison of the negative space with substrate materials alone (left) and S-resonators slabs (right) in front of a point source. The substrate slabs on the left have indices of n=+1 (top slab) and n=-1 (bottom slab). The same configuration for effective indices is applied for the S-resonator slabs. The similarity between wavefronts at front and exit face are clear. Also, the image of the point source is formed on the right with S-resonator slabs.

In Figure 6.3, an attempt is made to investigate the effect of negative space while its consisting slabs are moved apart. On the left, a combination of two slabs with n=-1 and n=+1 stacked above each other are set in front of a point source, and on the right, the same slabs are separated by multiple wavelengths. The fields at the bottom of the figures in the image site are identical. This similarity between exit wavefronts demonstrates that negative space is maintained despite the separation of metamaterial slabs.

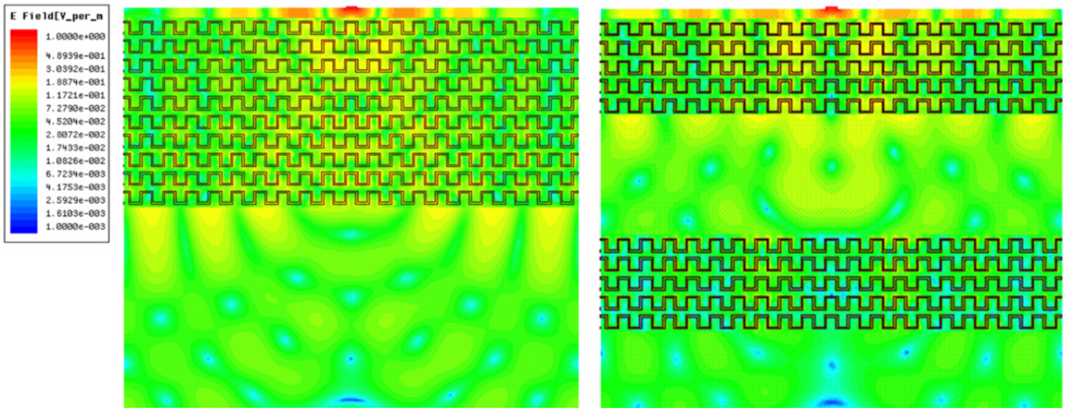

Figure 6.3: The positive and negative effective index metamaterial slabs are moved apart on the right to show that an image of the original point source still forms at the bottom of the figure.

As discussed before, we can use Babinet’s principle is the design of a 2D metasurface and its complementary design to produce phase conjugates of scattered fields and drive time reversal and reciprocity imaging from the effect. In Figure 6.4, this idea is evaluated using a metasurface composed of a double concentric rings metasurface and its complementary surface according to Babinet’s principle to produce scattering radiation patterns from each surface with the same magnitude, and the measured phase of these metasurfaces are opposite in sign.

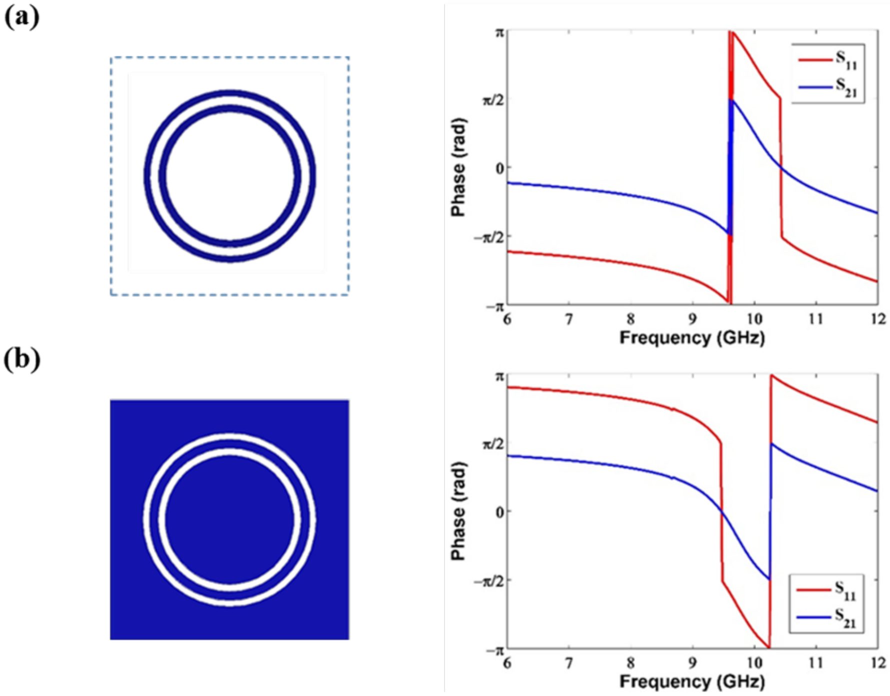

Figure 6.4: Double concentric rings metasurface unit cells and their corresponding phase diagram. The unit cells have dimensions of 15mm by 15mm where the inner ring and outer ring radii are 4.25mm and 5.25mm respectively with a trace width of 0.4mm. (a) Metasurface, (b) Complementary-Metasurface.

6.4. Conclusion

We investigated the possibility of integrating a complex metamaterial design in a scattering system as encoder and decoder of fields to achieve high-resolution data of scattering objects. The metamaterial structure would convert high spatial frequencies, evanescent waves, from scattering site to propagating wave toward far-field. This metamaterial would be the encoder component. A complementary design of the metamaterial could be used to recover the subwavelength resolution information at a remote location. For this purpose, we considered two metamaterial slabs which strongly interact with free space radiation. The effective refractive indices of slabs were n = +1 and n = -1 where the negative index slab operates as a time reversal or phase conjugation of incident fields. This performance is closely limited to the losses in the structure. The reciprocity that is responsible for the reconstruction of scattered object arises from the encoding and decoding of high spatial information through metamaterial structures. There is a need to understand the mechanism in which scattered field data is transferred over long distances while maintaining the option to recover evanescent waves and therefore high-resolution information. Also, the finite size limitation in the transverse direction in the metamaterial slabs might significantly restrain the conversion of evanescent waves to propagating ones. One possible solution could be to design a graded index metamaterial slab which has a unity refractive index at the scattering object but then the index changes to zero adiabatically to increase the efficiency of transferring the waves from encoder to decoder.

CHAPTER 7: APPLICATION OF METAMATERIALS TO SENSING

In recent years, metamaterials have found applications in sensing technologies, and they are offering unique opportunities for creating a new generation of sensors. Metamaterials are very sensitive to any change in their design and environment which leads to an ability to use them as high Q-sensors [190], [191].

Recently, metamaterials have also been the center of attention in biosensing applications in microwave, terahertz, and optical frequency. For instance, metamaterials are used as cost-efficient detection of label-free bio-agents; an electrically small SRR-based biosensor was proposed to detect binding of certain biomolecules at microwave frequencies [192]. In optical frequencies, the surface plasmons are extremely sensitive to the refractive index of the medium which the evanescent field penetrates to. This sensitivity to small changes in refractive index has been used significantly in biosensors. Because of the strong resonances in plasmonic structures and coupling between photons and surface plasmon polaritons, a detection limit of beyond 10^{-5} refractive index units (RIU) has been reported [193].

Another area that metamaterials have found applications is thin-film sensing. The interaction between EM fields and unidentified thin-film can offer key information and applications in chemistry and biology [194], [195]. Since frequency selective surfaces

(FSSs) can be designed to be small and their resonant frequency is tunable by modifying their design, they can be a potential tool for detection of highly sensitive chemical or biological thin films [196]. Thin-film sensors have to exhibit a sharp shift in their frequency response to detecting small amounts of sample substances. Also, to enhance the sensitivity of the sensor, the electric field should be confined in the sensing area that the sample is deposited. A tip-shaped SRR metamaterial was introduced to decrease the device size and its resonance frequency while improving the Q-factor of the sensor [197]. This design has shown sharper resonance dip in their transmission spectra delivering a sensitivity level of 16.2 MHz/μm with a nonlinear error less than 2 μm.

Metamaterials can be implemented to measure strain and temperature remotely in real time. Compared with traditional RF strain and temperature sensors, metamaterials offer some advantages including higher Q-factors, and sharper and deeper resonance dip in their spectra which lead to higher sensitivity and better sensor response linearity [198]–[201]. A double negative (DNG) metamaterial sensor was proposed at microwave frequencies with higher sensitivity over conventional RF sensors [202]. Moreover, sophisticated designs are emerging as multichannel sensors in metamaterials, such as a flexible metamaterial based device was reported to have applications in strain, chemical and biological sensing in the near-IR regime [203].

7.1. S-resonators as Frequency Based Sensors

For S-resonators, we have shown that by changing the refractive index of its substrate, the shift in main resonant frequencies are all following a linear trend which suggests the design can be implemented as a potential sensing tool for various applications, Figure 7.1.

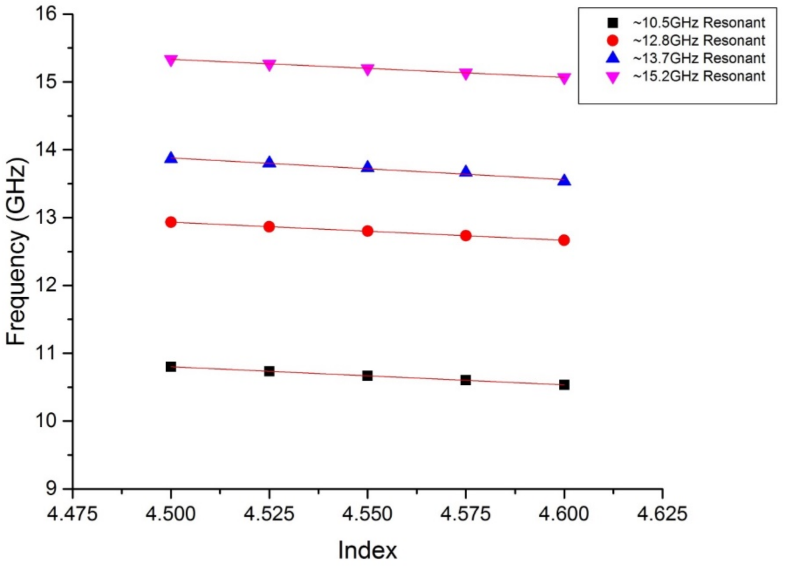

Figure 7.1: Simulation results (Lumerical FDTD) for observing a shift in resonant frequencies by changing the refractive index of S-resonator substrate.

To obtain above result, we conducted a series of simulations with S-resonators in the time domain using Lumerical FDTD, Figure 7.2. Referring to these figures, an infinitely extended mirrored S-resonator slab was designed using periodic boundary conditions and immersed in a dielectric substrate. A pulsed wave used as excitation incident wave to obtain transmission spectra of the metamaterial slab. The properties of this pulse with a 0.3ns time bandwidth is shown in Figure 7.2, which is a broadband frequency signal of about 18.63 GHz bandwidth with central frequency at 9.32 GHz. Frequency power point monitor was used to obtain calculated transmitted spectra at spatial locations after the slab.

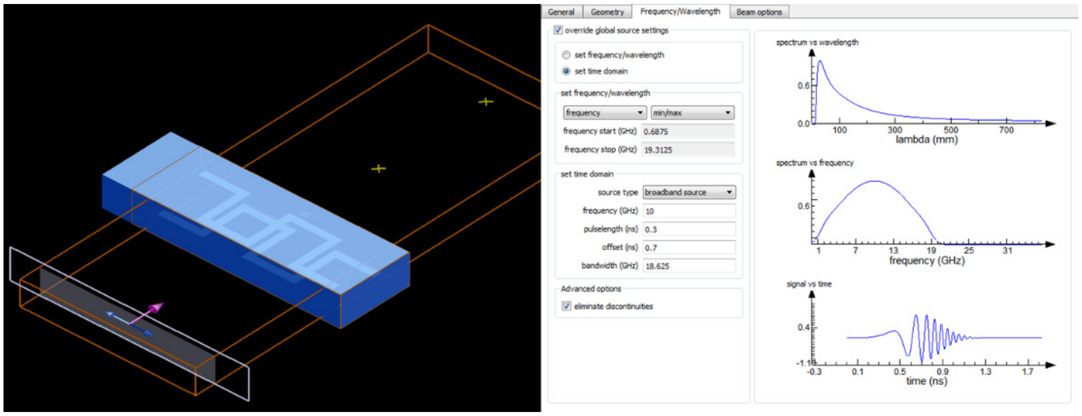

☑ override global source settings

○ set frequency/wavelength
● set time domain

set frequency/wavelength
frequency
min/max
frequency start (GHz) 0.6875
frequency stop (GHz) 19.3125

set time domain
source type broadband source
frequency (GHz) 10
pulselength (ns) 0.3
offset (ns) 0.7
bandwidth (GHz) 18.625

Advanced options
☑ eliminate discontinuities

Figure 7.2: Simulation setup for an infinitely extended mirrored S-resonators (left); and the excitation time signal properties (right).

A sample of transmitted spectrum is shown in Figure 7.3. This spectrum belongs to the metamaterial slab which the dielectric substrate has a refractive index of 4.5. The transmission peaks are dominant enough that we can use linearly scaled measurement to locate them.

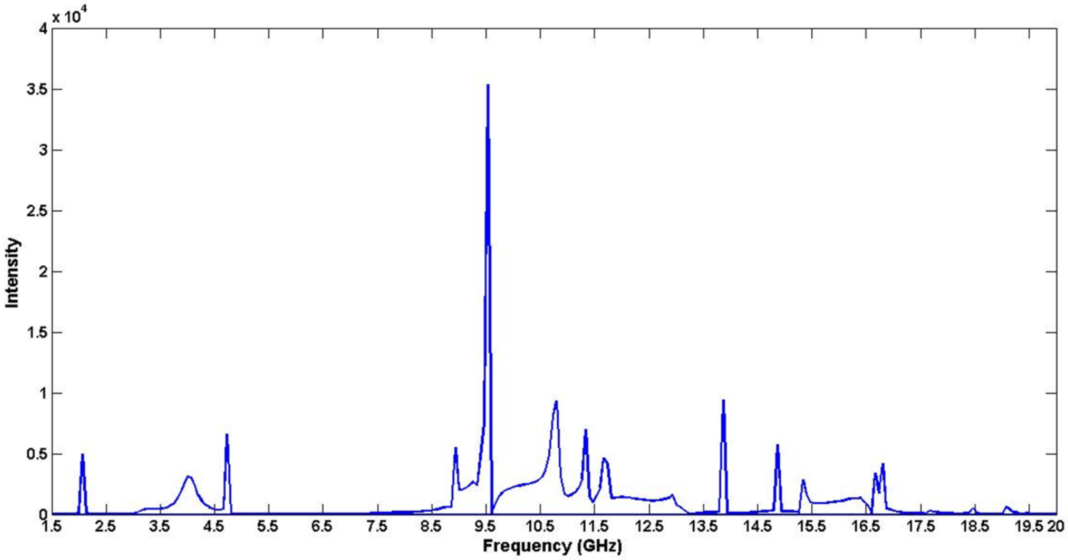

Figure 7.3: Transmitted spectrum of the metamaterial slab with a dielectric substrate of 4.5 refractive index.

To explore the sensing performance of the metamaterial, we change the substrate refractive index and calculate the transmitted spectra. Following then, we can trace the shift in the transmission peaks when the refractive index of the substrate varies. Figure 7.4 describes these shifts in frequency of transmission peaks when the refractive index of the substrate changes from 4.5 to 4.6 in 0.025 steps. The optimal sample rates were chosen in the simulation to extract the frequency of the peak accurately. Higher sample rates may cause longer simulation times considering limited available computation resources.

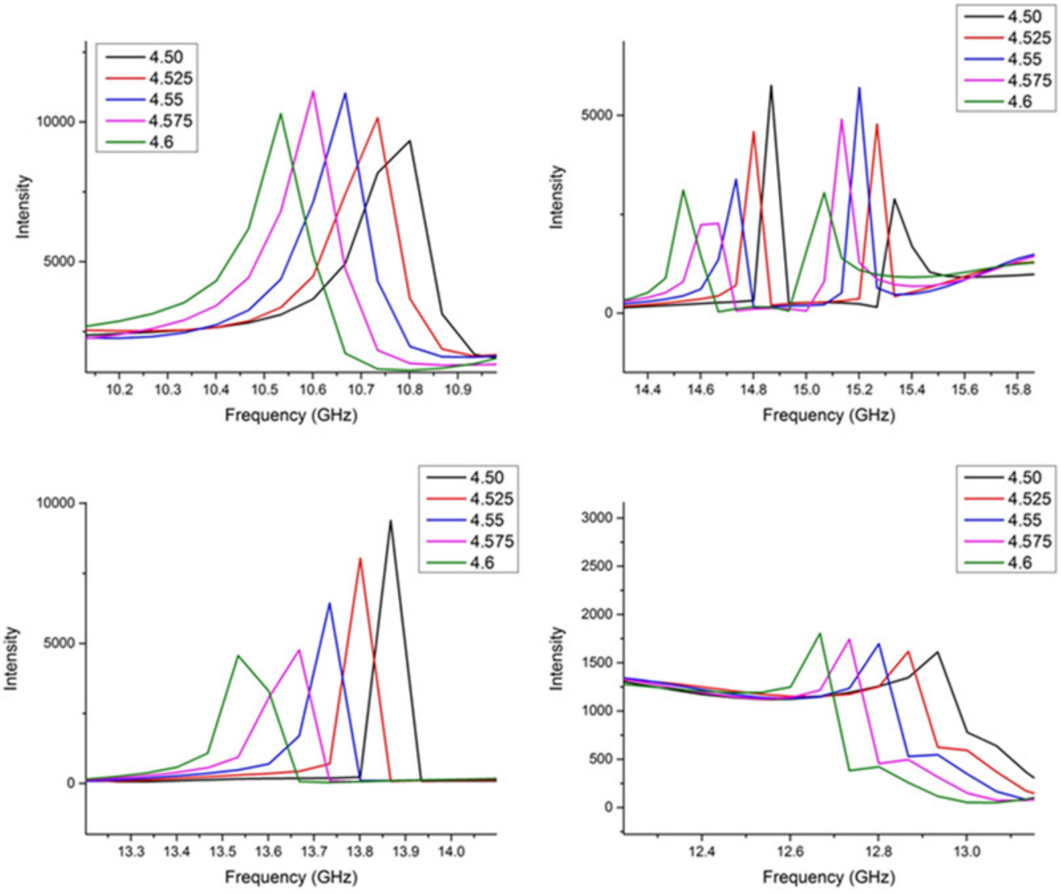

Figure 7.4: Frequency shifts in transmission peaks when the substrate's refractive increases from 4.5 to 4.6 in 0.025 steps.

Referring to notice a red shift in transmission spectra above when the refractive index of the substrate increases which is intuitive by considering the relation of the wavelength in the medium as $\lambda=\lambda_0/n$, where λ_0 is the free space wavelength while λ and n are the wavelengths and the refractive index of the medium respectively. Therefore, an increase in the refractive index of the substrate increases the effective refractive index of the metamaterial shortening the effective wavelength in the structure; and this is the reason we see a red shift in the response of the metamaterial. Observing this respond, we conclude that the metamaterial can act an effective refractive index sensor with a linear response as the nonlinear error is less than 50 KHz for 10^{-3} change in the refractive index.

7.2. S-resonators as Intensity Based Sensors

Beyond the metamaterial sensitivity to the refractive index of its surrounding, it is also very sensitive to any change in its original design. This shift can be a very little modification of the geometry which is caused by external forces such as strain, pressure or temperature [204]–[206]. Also, it can be a chance in properties of the materials in the metamaterial such as conductivity of the metal part [207]. To investigate the latter approach in our design, we calculate transmission spectra of a mirrored S-resonators metamaterial while the conductivity of a section of the metal strip is subject to change, Figure 7.5. All simulation setup is identical to the previous sensing simulation except there are two rows of S-resonators along propagation direction to enhance the mutual couplings between meta-atoms. While the refractive index of the substrate remains unchanged at 4.5, the conductivity of the red arm in Figure 7.5 takes multiple different values of 0, 500, 1000, 2000 and 3000 $\Omega^{-1}m^{-1}$. As it can be seen in the figure, for the conductivity of 0, as the segment blocks current from flowing through it with its infinite resistance, the resonance spectrum is dramatically unlike other spectra with finite conductivities. Apart from this extreme case, by changing the conductivity, we notice a change in intensity of the transmission peaks as an increase in their magnitude. One could expect such result considering the interaction of the incoming field with metals of different conductivity. However, we see the metamaterial still represent stability over its frequency spectra, and only intensity can be measured. By activating a small part of the S-resonator, one can use this approach to design passive remote sensors for chemical sensing applications.

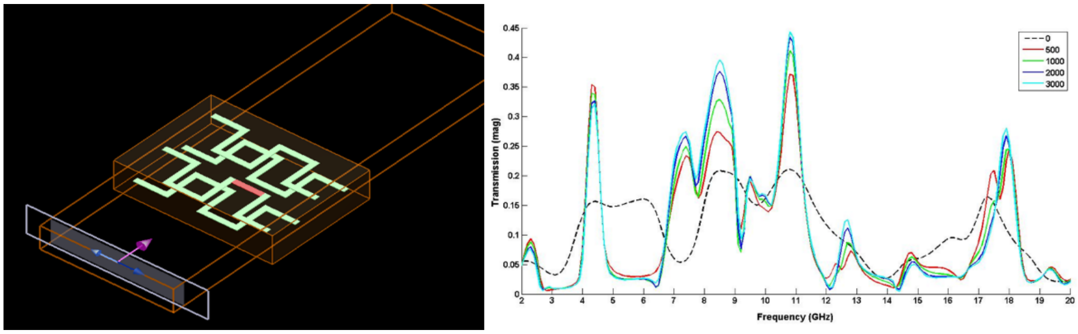

Figure 7.5: The simulation setup where the red arm on the metal strip indicates the part with variable conductivity (left). Transmission spectra are calculated for the different conductivity of the red arm (right).

7.3. Conclusion

We explored the sensing characteristics of S-resonator metamaterial considering its high Q-factor. It was shown that the spectra of the structure are sensitive to changes in refractive index of its host as well as minor variations in the conductivity of meander lines. The metamaterial acts as a frequency based sensors when the refractive index of its substrate changes. It shows multiple frequencies sensing signatures, and they have a linear response. It also behaves as an intensity based sensor when the conductivity of a section of the S-element strip changes. Future work can include fabricating metamaterial-based sensors, particularly using our design, for various applications such a chemical and remote sensing.

CHAPTER 8: NONLINEAR METAMATERIALS

The main reason that metamaterials have managed to obtain attention in optics and electromagnetism is that they are artificial materials with desirable properties. We can benefit from this freedom in design using any structural components, meta-atoms. By considering the limitations of fabrication technologies, we can still deliberately arrange meta-atoms to achieve the envisioned bulk material properties. As mentioned before, the negative refractive index is one of the most well-known examples of novel features of these engineered mediums.

With emerging all unique properties of metamaterials, nonlinear optics also found a new playground. Where conventional nonlinearities in natural materials are limited to particular ranges, metamaterials can construct or enhance a desired nonlinear response depending on specific needs. As early in 90's, it was suggested that an artificial structure could exhibit phase conjugation which is a nonlinear process [208]. At the end of that decade, the resonant enhancement was predicted using split-ring resonators as one of the most famous meta-atoms [209]. Later, a wide range of nonlinear phenomena introduced by different groups implementing metamaterials toward novel applications [210],[211],[212].

We would like to understand the impact of the local electric field on the effective nonlinear polarizability of certain nanomaterials and ultimately on their nonlinear far field properties. The understanding of this behavior should help to develop a new class of metamaterials whereby we can enhance nonlinear properties while minimizing linear absorption at the same time.

The control of higher order nonlinearities as a result of nanostructuring has been studied for some time [213], and their essential parameters have been investigated experimentally for various metals and dielectrics [214]. Analytical modeling of nonlinear phenomena in the material systems has been proposed [215] which is the fundamental tool for numerical approaches to evaluate and study similar systems.

Regarding optimizing the metamaterial design to enhance nonlinear absorption while reducing linear absorption, there is a need which we investigate to model and verify a better approach. Earlier models only studied time independent nonlinearities which would not be accurate for situations with higher local field coupling [216]. In this work, by using an advanced formalism, we can achieve optimal designs to describe nonlinear properties of structured systems properly.

To connect the near field properties to the far field nonlinear behavior, we are modifying the FDTD method appropriately to describe intrinsic nonlinearities of materials, such as real and imaginary parts of the $\chi^{(3)}$ permittivity. It is important that this modification is performed for a robust commercial software platform, such as Lumerical FDTD, through the use of the material plugin. The Lumerical software would allow us to perform large scale, parallelized structure optimization studies.

8.1. Calculation Method

To begin with, the nonlinear polarizability in the following equation has to be extracted,

$$\boldsymbol{D} = \varepsilon_0 \boldsymbol{E} + \boldsymbol{P} \tag{8.1}$$

where $\boldsymbol{D}$ is the electric displacement, ε_0 is the permittivity of the vaccum, $\boldsymbol{E}$ is the electric field, and $\boldsymbol{P}$ is the polarization. Different models for polarizaation is avaialble to account nonlinearties. We proceed with the following terms along our interests,

$$\boldsymbol{P} = \varepsilon_0 \chi_\infty \boldsymbol{E} + \boldsymbol{P}_{Kerr} + \boldsymbol{P}_{TPA} \tag{8.2}$$

with $\varepsilon_0 \chi_\infty \boldsymbol{E}$ as nondispersive polarization, the Kerr effect term $\boldsymbol{P}_{Kerr} = \varepsilon_0 \chi_{Kerr} \boldsymbol{E}$, and $\boldsymbol{P}_{TPA} = \varepsilon_0 \chi_{TPA} \boldsymbol{E}$ for Two Photon Absoprtion effect.

The Kerr susceptibility χ_{Kerr} satifies the following equation [217],

$$\frac{\partial \chi_{Kerr}}{\partial \boldsymbol{t}} + \frac{\chi_{Kerr}}{\tau_{Kerr}} = \frac{1}{\tau_{Kerr}} \varepsilon_2 |E|^{\boldsymbol{2}} \tag{8.3}$$

where ε_2 is the Kerr permittivity, and τ_{Kerr} is the response time**.** For TPA susceptibility we can use the below equation [215],

$$\chi_{TPA} = i \frac{c_0 n_0 \beta_{Kerr}}{\omega} I = -\frac{c_0^2 \varepsilon_0 n_0^2 \beta_{Kerr}}{2i\omega} |E|^{\boldsymbol{2}} \tag{8.4}$$

with c_0 as speed of light in vaccum, n_0 as the linear refractive index of medium, ω as the frequecny, I as the intensity of the field, and β_{Kerr} as the TPA coefficent. To implement this term in FDTD calculation, we need the time dependency of formula. To drive the time domain format, we substitue $i\omega$ with $-\partial/\partial t$,

$$\begin{aligned}\chi_{TPA}{}^{(n+1)} &= \chi_{TPA}{}^{(n)} - \frac{c_0^2\varepsilon_0 n_0^2 \beta_{Kerr}\Delta t}{2i\omega}\left|E^{(n+1/2)}\right|^{\mathbf{2}} \\ &\cong \chi_{TPA}{}^{(n)} - \frac{c_0^2\varepsilon_0 n_0^2 \beta_{Kerr}\Delta t}{2i\omega}\left[\left|E^{(n+1)}\right|^{\mathbf{2}} + \left|E^{(n)}\right|^{\mathbf{2}}\right]\end{aligned} \tag{8.5}$$

where $(n+1)$ and (n) refers to time steps in the equation. Since $\chi_{TPA}{}^{(n+1)}$ depends on $E^{(n+1)}$ which is unknown at time step $(n+1)$, iterations in calculation is essential to obtain self-consistent $\chi_{TPA}{}^{(n+1)}$ and $E^{(n+1)}$.

Inserting above terms into Equation (8.1) and driving its time domain equation, we can write,

$$\frac{\partial D}{\partial t} = \varepsilon_0\varepsilon_\infty\frac{\partial E}{\partial t} + \varepsilon_0\frac{\partial(\chi_{Kerr}E)}{\partial t} + \frac{c_0^2{\varepsilon_0}^2 n_0^2\beta_{Kerr}}{2}|E|^{\mathbf{2}}E \tag{8.6}$$

finally, the difference equation can be driven from above as,

$$E^{(n+1)} = \frac{g_2\left(E^{(n+1)}\right)}{g_1\left(E^{(n+1)}\right)}E^{(n)} + \frac{D^{(n+1)} - D^{(n)}}{\varepsilon_0 g_1\left(E^{(n+1)}\right)} \tag{8.7}$$

where

$$g_1\left(E^{(n+1)}\right) = \varepsilon_\infty + \chi_{Kerr}^{(n+1)}E^{(n+1)} + \frac{c_0^2\varepsilon_0 n_0^2\beta_{Kerr}\Delta t}{8}\left[\left|E^{(n+1)}\right|^{\mathbf{2}} + \left|E^{(n)}\right|^{\mathbf{2}}\right] \tag{8.8}$$

and

$$g_2\left(E^{(n+1)}\right) = \varepsilon_\infty + \chi_{Kerr}^{(n)} - \frac{c_0^2\varepsilon_0 n_0^2\beta_{Kerr}\Delta t}{8}\left[\left|E^{(n+1)}\right|^{\mathbf{2}} + \left|E^{(n)}\right|^{\mathbf{2}}\right] \tag{8.9}$$

Equation (8.8) and (8.9) can be solved by iteration. Based on our analysis, no more than six iterations would be required for computations to achieve consistent results.

8.2. Simulation and Result Verification

Having the theoretical basis, we identified an appropriate algorithm for modifying conventional FDTD method to include nonlinearities of Kerr effect as well as Two-Photon Absorption (TPA). Moreover, we constructed nonlinear material plugins for Lumerical in Windows and Linux platforms, see Appendix B. To validate the material plugin against the prediction of both Kerr effect as well as Two-Photon Absorption (TPA) in simple material examples, various simulations were performed.

For instance, we replicated the results of 2D simulations of an optical switch [218]. In the original work, two-photon absorption effect is analyzed in an all-optical switch by a home-made FDTD engine specifically designed for the structure. In the proposed photonic crystal all-optical switch, a control beam exploits nonlinearity, and the intensity of the input signal is maintained constant. Figure 8.1 shows the schematic layout of the designed optical switch.

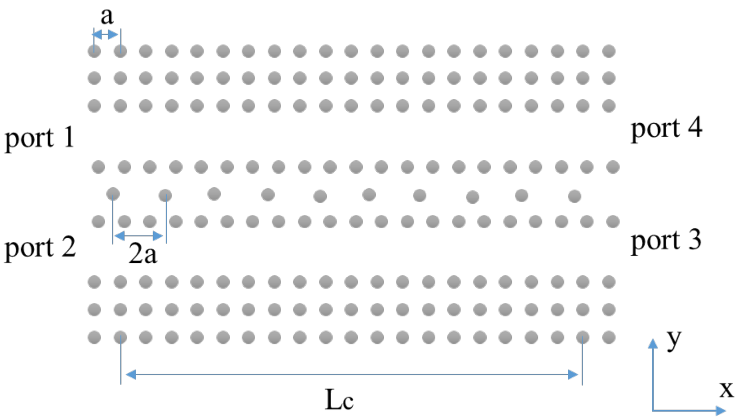

Figure 8.1: Schematic of the analyzed switch, the cross-section of rods which are along the z-direction.

The rods are made out of AlGaAs with nondispersive refractive index of $n_0 = 3.4$, Kerr susceptibility of $\chi_{Kerr} = 9.2 \times 10^{-19}(m^2V^{-2})$, and TPA coefficent of $\beta_{TPA} = 3.5 \times 10^{-11}(mW^{-1})$. The lattice constant is $a = 510nm$, and the raidus of rods is set as $r = 0.2a$. The design has 72 and 12 rods along x- and y-directions, respectively. In Lumerical, meshing was set to meet the equivalence computational resolution of the original simulation. The input signal is injected in Port 1 and based on the intrinsic parameter of material it is outputted to Port 3 or Port 4. The control beam of high intensity is injected to the waveguide in the middle of the device. Excitations are from point sources which their frequency and time domain parameteres are retrieved from the paper with central frequency of 193.5 THZ for signal beam and 170 THz for control beam. As mentioned before, the intesnity of the control beam should be very high to alternate intrinsic nonlinear effects of nanoparticles. Therefore, an intesity of around 300 GW/cm^2 was set for the control beam.

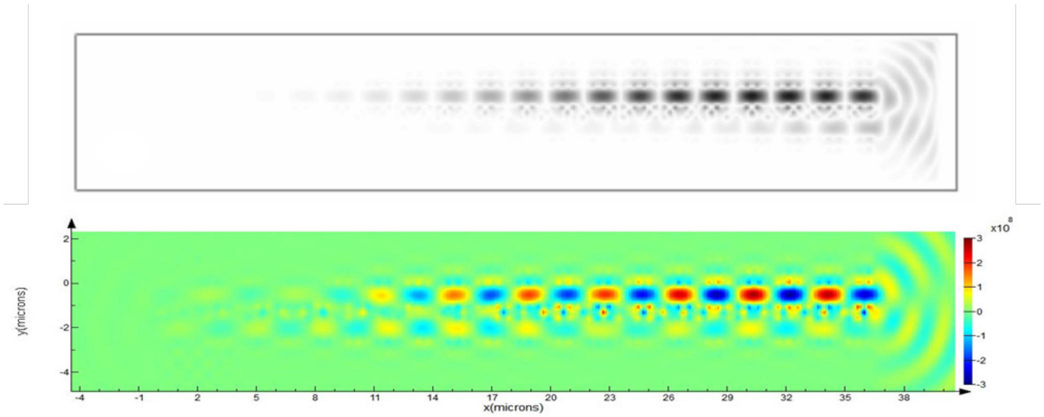

Figure 8.2: E-field distribution for the linear case; original simulation (top), Lumerical simulation (bottom).

As we can see in Figure 8.2, when the nonlinear terms are not significant in the simulations due to the low intensity of control beam, the input signal from Port 1 will be outputted at Port 4. However, when the control beam intensity goes very high, nonlinear terms in the material become significant, and this in return results in an increase in the refractive index of the rods in the waveguide region where control beam propagates. Consequently, the coupling in the photonic crystal increases and the switch functions in the cross state. As depicted in Figure 8.3, in this case of nonlinear regime the signal beam which is inputted at Port 1 will be outputted at Port 3.

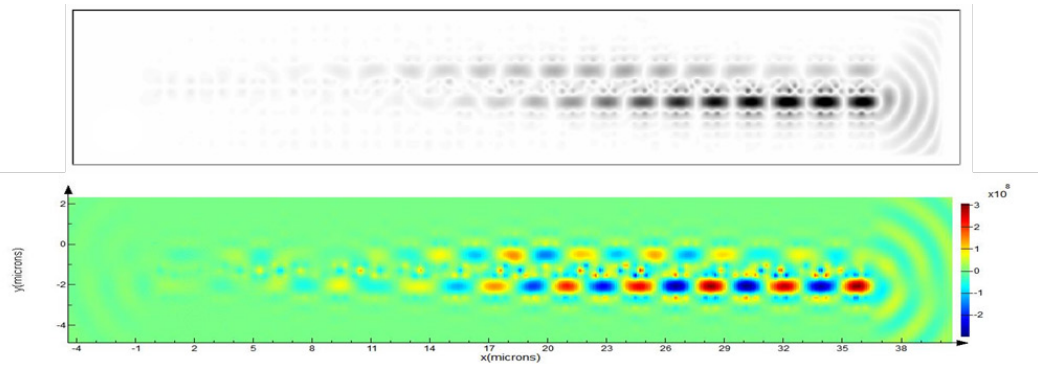

Figure 8.3: E-field distribution for the nonlinear case; original simulation (top), Lumerical simulation (bottom).

To investigate the effect of each nonlinearity term, specially TPA, we can look at the transmission spectrum of the control beam. The original paper has used a method to calculate the spectrum whereas we have used monitoring tools in Lumerical to extract the real-time data representing field at the points of interest. As we can see from Figure 8.4, compared to the linear case, transmission curves of nonlinear cases are red-shifted. As stated in [218], the reason is due to shift of the waveguide mode which lies within the forbidden photonic band gap. However, when the TPA is strong, a portion of the electric field will be dissipated within the rods, and the nonlinear effect will be weaker. By studying the impact of TPA for various frequencies of the control beam, an optimized frequency can be chosen to have a stronger nonlinear effect.

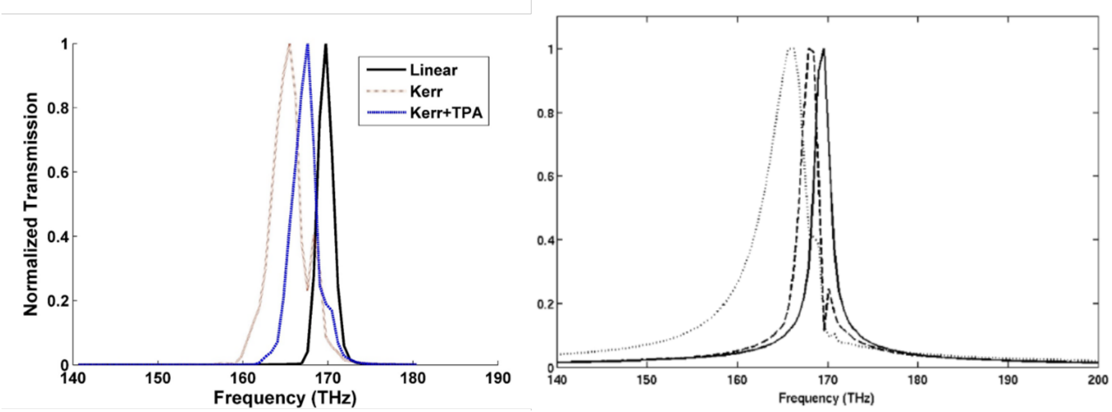

Figure 8.4: Normalized transmission spectra of control beam for each case; Lumerical simulations (left), calculated results from original work (right).

Further investigations were performed using the developed plugins for comparison with already published data. The results were adequate to release the application for internal use. The next phases of the project including applying developed plugin to study target material systems with known intrinsic nonlinear properties and following experiments are conducting at MIT Lincoln Lab.

8.3. Conclusion

Designing metamaterial structures at optical frequencies in the presence of high power fields requires considering nonlinear effects at light-matter interaction level. Most of the available commercial EM simulation packages have limited nonlinear phenomena support. Therefore we developed additional plugins for the desired software, Lumerical FDTD, to include TPA effect for the design of nanostructures. We tested and successfully validated the accuracy of the developed plugin. The following experiments are conducting at MIT

Lincoln Lab using the plugin to design and fabricate nanostructured metamaterials. One can use the platform of this work to develop additional plugins to include other nonlinear effects based on their design and need.

CHAPTER 9: CONCLUSION

We explored some fundamental properties of metamaterials and their novel applications for several purposes. A bianisotropic metamaterial consisting of subwavelength mirrored S-resonators was our primary design in simulations and experiments. An essential step toward understanding the behavior of metamaterial is to evaluate and determine the bulk electromagnetic properties of the structure. Usually, an analytical retrieval procedure uses measured scattering parameters to calculate effective parameters such as permittivity and permeability. We employed a well-known retrieval technique which was optimized for our proposed metamaterial design. The S-parameters were obtained numerically in both frequency-domain simulations as well as time-domain ones to validate final calculation. The results show an overlapping negative effective permittivity and permeability over a range of 2.4 GHz bandwidth, and this delivers a practical negative refractive index metamaterial within frequencies of 5.8 GHz to 8.2 GHz with left-handed electromagnetic properties.

We discussed the connection between a negative index metamaterial and negative refraction and confirmed that the seen negative refraction in our proposed design is due to real negative index. The validation was through studying scattering in the metamaterial structure for frequencies at which the periodicity of S-resonators was in the same order of effective wavelength. The total scattering and diffraction behavior can explain the origin of negative refraction and if Bragg-like scattering or an effective negative index medium is responsible for seen effects. Since the meta-atoms are strongly resonant, there is a high coupling between S-resonators resulting in a bulk medium with homogeneous electromagnetic properties.

Metamaterials are limited to a narrow bandwidth for exhibiting left-handed properties, and there is a need in tunable metamaterial structures for applications such as radiation filters, modulators, or sensing. Therefore, we introduced the idea of a meta-substrate for our S-resonators design as an approach for bandwidth engineering. The bandwidth tuning of effective parameters is through adding independent resonators to the substrate which would modify and shifts the overall resonance response by coupling to S-resonators. Further progress in future would be to introduce real-time tunability by changing electrical properties of the additional resonators. In addition to meta-substrate design, we proposed a polarization-insensitive design with a left-handed response based on original mirrored S-shaped resonators. Using numerical simulations, we demonstrated that the structure is polarization independent, and for a specific design, criteria had a negative refractive index frequency range. Next steps could be the fabrication of bulk metamaterials with 3D printing methods considering the materials and geometry to extend the range the applications.

An interesting use of metamaterials is for subwavelength imaging. In the vicinity of the object, metamaterials can couple to the evanescent waves and transfer them to the image space. We investigated this transfer function in metamaterial slab made out of mirrored S-resonators. We were able to achieve some evidence of subwavelength imaging up to λ/5, but further resolution might be restricted because of the relative size of meta-atoms to an incident wavelength that prevents to achieve better resolutions. Above that, losses in the metamaterial structure significantly degrade the quality of constructed images. After all, to reach further improvements, we can apply image processing techniques such as compressive sampling to attain higher subwavelength resolution images. Another approach in sub-resolution imaging is through reciprocity. We introduced the concept of remotely encoding and decoding the subwavelength information of scattering objects using a complex metamaterial design and without any signal processing in between. The metamaterial structure, encoder, would convert high spatial frequencies, evanescent waves, to propagating ones which would be detected at far-field with a complementary metamaterial structure, decoder. The complementary metamaterial would recover the subwavelength resolution information at a remote location. For this purpose, we considered two metamaterial slabs which strongly interact with free space radiation. The effective refractive indices of slabs were n = +1 and n = -1 where the negative index slab operates as a time reversal or phase conjugation of incident fields, and losses in the structure constrain the efficiency of conversion. There is a need to understand the mechanism in which scattered field data is transferred over long distances while maintaining the option to recover evanescent waves and therefore high-resolution information. Also, the finite size limitation in the transverse direction in the metamaterial slabs might significantly restrain the conversion of evanescent waves to propagating ones. A possible solution is designig a graded index metamaterial slab which has a unity refractive index at the scattering object but then the index changes to zero adiabatically to increase the efficiency of transferring the waves from encoder to decoder.

Metamaterials are generally composed of high Q-factor resonators, and this would make them as ideal sensors. We demonstrated that the spectral response of the S-resonator metamaterial is sensitive to variations in the refractive index of the substrate. There would be a dominant shift in the spectra of metamaterial when the refractive index of metal resonators surrounding changes, hence we can use use the metamaterial as a frequency-based sensor. Our results show that the mirrored S-resonator metamaterial is a linear refractive index sensor with a nonlinear error of less than 50 KHz spectral frequency shift for 10^{-3} change in the refractive index. In addition, we can use the metamaterial as intensity-based sensors by modifying the conductivity of the S-resonator metal trace. For further investigation, we can fabricate and characterize metamaterial-based sensors for various applications such a chemical and remote sensing.

Nonlinear effects in metamaterials are essential to understand particularly at optical frequencies to optimize the structure design. Usually, famous electromagnetic simulation tools do not offer implemented nonlinear effects thoroughly. We developed additional plugins for Lumerica FDTD to apply Two-Photo Absorption nonlinear effect in the simulations. The built-in plugin was validated through extensive numerical calculations. Further metamaterial structure design and optimization followed at MIT Lincoln Lab. One can use the developed platform to include more nonlinear effects according to their need.

REFERENCES

[1] J. Ramsay, “Microwave Antenna and Waveguide Techniques before 1900,” *Proc. IRE*, vol. 46, no. 2, pp. 405–415, Feb. 1958.

[2] H. Lamb, “On Group - Velocity,” *Proc. London Math. Soc.*, vol. s2-1, no. 1, pp. 473–479, Jan. 1904.

[3] A. Schuster, *An introduction to the theory of optics*. E. Arnold, 1904.

[4] L. I. Mandel’shtam, “Group velocity in a crystal lattice,” *Zh. Eksp. Teor. Fiz*, vol. 15, no. 9, pp. 475–478, 1945.

[5] L. I. Mandel’shtam, “The 4th lecture of LI Mandel’shtam given at Moscow State University (05/05/1944),” *Collect. Sci. Work.*, vol. 2, 1994.

[6] Pafomov and V.E., “ON TRANSITION RADIATION AND THE VAVILOV-CHERENKOV RADIATION,” *Zhur. Eksptl’. Teoret. Fiz.*, vol. Vol: 36, 1959.

[7] V. M. Agranovich, V. L. Ginzburg, V. M. Agranovich, and V. L. Ginzburg, *Spatial dispersion in crystal optics and the theory of excitons*. Interscience New York, 1966.

[8] V. G. Veselago, “THE ELECTRODYNAMICS OF SUBSTANCES WITH SIMULTANEOUSLY NEGATIVE VALUES OF ϵ AND μ,” *Sov. Phys. Uspekhi*, vol. 10, no. 4, pp. 509–514, Apr. 1968.

[9] D. Smith, W. Padilla, D. Vier, S. Nemat-Nasser, and S. Schultz, “Composite Medium with Simultaneously Negative Permeability and Permittivity,” *Phys. Rev. Lett.*, vol. 84, no. 18, pp. 4184–4187, May 2000.

[10] J. B. Pendry, A. J. Holden, W. J. Stewart, and I. Youngs, “Extremely Low Frequency Plasmons in Metallic Mesostructures,” *Phys. Rev. Lett.*, vol. 76, no. 25, pp. 4773–4776, Jun. 1996.

[11] J. B. Pendry, A. J. Holden, D. J. Robbins, and W. J. Stewart, “Magnetism from conductors and enhanced nonlinear phenomena,” *Microw. Theory Tech. IEEE Trans.*, vol. 47, no. 11, pp. 2075–2084, 1999.

[12] P. M. Valanju, R. M. Walser, and A. P. Valanju, “Wave Refraction in Negative-Index Media: Always Positive and Very Inhomogeneous,” *Phys. Rev. Lett.*, vol. 88, no. 18, p. 187401, Apr. 2002.

[13] J. Pacheco, T. M. Grzegorczyk, B.-I. Wu, Y. Zhang, and J. A. Kong, “Power Propagation in Homogeneous Isotropic Frequency-Dispersive Left-Handed Media,” *Phys. Rev. Lett.*, vol. 89, no. 25, p. 257401, Dec. 2002.

[14] J. B. Pendry and D. R. Smith, “Comment on ‘Wave Refraction in Negative-Index Media: Always Positive and Very Inhomogeneous,’” *Phys. Rev. Lett.*, vol. 90, no. 2, p. 29703, Jan. 2003.

[15] C. G. Parazzoli, R. B. Greegor, K. Li, B. E. C. Koltenbah, and M. Tanielian, “Experimental Verification and Simulation of Negative Index of Refraction Using Snell’s Law,” *Phys. Rev. Lett.*, vol. 90, no. 10, p. 107401, Mar. 2003.

[16] A. A. Houck, J. B. Brock, and I. L. Chuang, “Experimental Observations of a Left-Handed Material That Obeys Snell’s Law,” *Phys. Rev. Lett.*, vol. 90, no. 13, p. 137401, Apr. 2003.

[17] J. Huangfu *et al.*, “Experimental confirmation of negative refractive index of a metamaterial composed of Ω-like metallic patterns,” *Appl. Phys. Lett.*, vol. 84, no. 9, p. 1537, 2004.

[18] H. Chen *et al.*, “Left-handed materials composed of only S-shaped resonators,” *Phys. Rev. E*, vol. 70, no. 5, p. 57605, Nov. 2004.

[19] J. C. M. Garnett, “Colours in Metal Glasses and in Metallic Films,” *Philos. Trans. R. Soc. A Math. Phys. Eng. Sci.*, vol. 203, no. 359–371, pp. 385–420, Jan. 1904.

[20] D. A. Bruggeman, “Effective medium model for the optical properties of composite material,” *Ann. der Phys. Ser.*, vol. 5, no. 24, pp. 636–664, 1935.

[21] A. M. Nicolson and G. F. Ross, “Measurement of the Intrinsic Properties of Materials by Time-Domain Techniques,” *IEEE Trans. Instrum. Meas.*, vol. 19, no. 4, pp. 377–382, 1970.

[22] R. W. Ziolkowski, “Design, fabrication, and testing of double negative metamaterials,” *IEEE Trans. Antennas Propag.*, vol. 51, no. 7, pp. 1516–1529, Jul. 2003.

[23] X. Chen, T. Grzegorczyk, B.-I. Wu, J. Pacheco, and J. Kong, “Robust method to retrieve the constitutive effective parameters of metamaterials,” *Phys. Rev. E*, vol. 70, no. 1, p. 16608, Jul. 2004.

[24] D. R. Smith, D. C. Vier, T. Koschny, and C. M. Soukoulis, “Electromagnetic

parameter retrieval from inhomogeneous metamaterials," *Phys. Rev. E*, vol. 71, no. 3, p. 36617, Mar. 2005.

[25] G. Lubkowski, R. Schuhmann, and T. Weiland, "Extraction of effective metamaterial parameters by parameter fitting of dispersive models," *Microw. Opt. Technol. Lett.*, vol. 49, no. 2, pp. 285–288, Feb. 2007.

[26] V. V. Varadan and R. Ro, "Unique Retrieval of Complex Permittivity and Permeability of Dispersive Materials From Reflection and Transmitted Fields by Enforcing Causality," *IEEE Trans. Microw. Theory Tech.*, vol. 55, no. 10, pp. 2224–2230, Oct. 2007.

[27] T. Koschny, P. Markoš, E. N. Economou, D. R. Smith, D. C. Vier, and C. M. Soukoulis, "Impact of inherent periodic structure on effective medium description of left-handed and related metamaterials," *Phys. Rev. B*, vol. 71, no. 24, p. 245105, Jun. 2005.

[28] D. R. Smith, S. Schultz, P. Markoš, and C. M. Soukoulis, "Determination of effective permittivity and permeability of metamaterials from reflection and transmission coefficients," *Phys. Rev. B*, vol. 65, no. 19, p. 195104, Apr. 2002.

[29] S. Arslanagic *et al.*, "A Review of the Scattering-Parameter Extraction Method with Clarification of Ambiguity Issues in Relation to Metamaterial Homogenization," *IEEE Antennas Propag. Mag.*, vol. 55, no. 2, pp. 91–106, Apr. 2013.

[30] J. A. Kong, "Electromagnetic wave interaction with stratified negative isotropic media," *Prog. Electromagn. Res.*, vol. 35, pp. 1–52, 2002.

[31] P. Markos and C. Soukoulis, "Transmission properties and effective electromagnetic parameters of double negative metamaterials.," *Opt. Express*, vol. 11, no. 7, pp. 649–61, Apr. 2003.

[32] J. E. Sipe and J. Van Kranendonk, "Macroscopic electromagnetic theory of resonant dielectrics," *Phys. Rev. A*, vol. 9, no. 5, pp. 1806–1822, May 1974.

[33] P. A. Belov, S. A. Tretyakov, and A. J. Viitanen, "Nonreciprocal microwave band-gap structures," *Phys. Rev. E*, vol. 66, no. 1, p. 16608, Jul. 2002.

[34] C. R. Simovski, P. A. Belov, and S. Sailing He, "Backward wave region and negative material parameters of a structure formed by lattices of wires and split-ring resonators," *IEEE Trans. Antennas Propag.*, vol. 51, no. 10, pp. 2582–2591, Oct. 2003.

[35] C. Menzel, C. Rockstuhl, T. Paul, F. Lederer, and T. Pertsch, “Retrieving effective parameters for metamaterials at oblique incidence,” *Phys. Rev. B*, vol. 77, no. 19, p. 195328, May 2008.

[36] Z. Szabo, G.-H. Park, R. Hedge, and E.-P. Li, “A Unique Extraction of Metamaterial Parameters Based on Kramers–Kronig Relationship,” *IEEE Trans. Microw. Theory Tech.*, vol. 58, no. 10, pp. 2646–2653, Oct. 2010.

[37] M. Lapine, L. Jelinek, R. Marqués, and M. J. Freire, “Exact modelling method for discrete finite metamaterial lens,” *IET Microwaves, Antennas Propag.*, vol. 4, no. 8, p. 1132, 2010.

[38] M. Lapine, L. Jelinek, and R. Marqués, “Surface mesoscopic effects in finite metamaterials.,” *Opt. Express*, vol. 20, no. 16, pp. 18297–302, Jul. 2012.

[39] M. F. Khan and M. J. Mughal, “Modified single side paired S-ring resonators,” in *Proceedings of the 3rd International Congress on Advanced Electromagnetic Materials in Microwaves and Optics*, 2009.

[40] R. Marqués, F. Medina, and R. Rafii-El-Idrissi, “Role of bianisotropy in negative permeability and left-handed metamaterials,” *Phys. Rev. B*, vol. 65, no. 14, p. 144440, Apr. 2002.

[41] J. B. Pendry, A. J. Holden, D. J. Robbins, and W. J. Stewart, “Low frequency plasmons in thin-wire structures,” *J. Phys. Condens. Matter*, vol. 10, no. 22, pp. 4785–4809, Jun. 1998.

[42] H. Chen *et al.*, “MAGNETIC PROPERTIES OF S-SHAPED SPLIT-RING RESONATORS,” *Prog. Electromagn. Res.*, vol. 51, pp. 231–247, 2005.

[43] Y.-C. Chuang, R. Dudley, and M. A. Fiddy, “Optimal arrangement of meta-atoms composing metamaterials,” in *SPIE OPTO*, 2012, p. 82691D.

[44] M. Karami, S. Kitchin, and M. A. Fiddy, “Scattering and coupling between subwavelength resonators,” in *SPIE NanoScience + Engineering*, 2014, p. 91602O.

[45] E. F. Kuester, M. A. Mohamed, M. Piket-May, and C. L. Holloway, “Averaged transition conditions for electromagnetic fields at a metafilm,” *IEEE Trans. Antennas Propag.*, vol. 51, no. 10, pp. 2641–2651, Oct. 2003.

[46] C. L. Holloway, M. A. Mohamed, E. F. Kuester, and A. Dienstfrey, “Reflection and Transmission Properties of a Metafilm: With an Application to a Controllable

Surface Composed of Resonant Particles," *IEEE Trans. Electromagn. Compat.*, vol. 47, no. 4, pp. 853–865, Nov. 2005.

[47] P.-Y. Chen and A. Alù, "Mantle cloaking using thin patterned metasurfaces," *Phys. Rev. B*, vol. 84, no. 20, p. 205110, Nov. 2011.

[48] Y. Yang *et al.*, "A metasurface carpet cloak for electromagnetic, acoustic and water waves," *Sci. Rep.*, vol. 6, p. 20219, Jan. 2016.

[49] D. Sievenpiper, Lijun Zhang, R. F. J. Broas, N. G. Alexopolous, and E. Yablonovitch, "High-impedance electromagnetic surfaces with a forbidden frequency band," *IEEE Trans. Microw. Theory Tech.*, vol. 47, no. 11, pp. 2059–2074, 1999.

[50] Y. Zhao, X.-X. Liu, and A. Alù, "Recent advances on optical metasurfaces," *J. Opt.*, vol. 16, no. 12, p. 123001, Dec. 2014.

[51] B. Luk'yanchuk *et al.*, "The Fano resonance in plasmonic nanostructures and metamaterials.," *Nat. Mater.*, vol. 9, no. 9, pp. 707–15, Sep. 2010.

[52] N. Papasimakis, Y. H. Fu, V. a. Fedotov, S. L. Prosvirnin, D. P. Tsai, and N. I. Zheludev, "Metamaterial with polarization and direction insensitive resonant transmission response mimicking electromagnetically induced transparency," *Appl. Phys. Lett.*, vol. 94, no. 21, p. 211902, 2009.

[53] F. Falcone *et al.*, "Babinet Principle Applied to the Design of Metasurfaces and Metamaterials," *Phys. Rev. Lett.*, vol. 93, no. 19, p. 197401, Nov. 2004.

[54] V. G. Veselago, "THE ELECTRODYNAMICS OF SUBSTANCES WITH SIMULTANEOUSLY NEGATIVE VALUES OF ##IMG## [http://ej.iop.org/images/0038-5670/10/4/R04/toc_eps.gif] {ε} AND μ," *Sov. Phys. Uspekhi*, vol. 10, no. 4, p. 509, 1968.

[55] A. Grbic and G. V. Eleftheriades, "Experimental verification of backward-wave radiation from a negative refractive index metamaterial," *J. Appl. Phys.*, vol. 92, no. 10, p. 5930, 2002.

[56] G. V. Eleftheriades, A. K. Iyer, and P. C. Kremer, "Planar negative refractive index media using periodically L-C loaded transmission lines," *IEEE Trans. Microw. Theory Tech.*, vol. 50, no. 12, pp. 2702–2712, Dec. 2002.

[57] C. Caloz and T. Itoh, "Application of the transmission line theory of left-handed

(LH) materials to the realization of a microstrip "LH line"," in *IEEE Antennas and Propagation Society International Symposium (IEEE Cat. No.02CH37313)*, 2002, vol. 2, pp. 412–415.

[58] J. Zhou, L. Zhang, G. Tuttle, T. Koschny, and C. M. Soukoulis, "Negative index materials using simple short wire pairs," *Phys. Rev. B*, vol. 73, no. 4, p. 41101, Jan. 2006.

[59] J. Wang *et al.*, "Normal-incidence left-handed metamaterials based on symmetrically connected split-ring resonators," *Phys. Rev. E*, vol. 81, no. 3, p. 36601, Mar. 2010.

[60] M. S. Wheeler, J. S. Aitchison, and M. Mojahedi, "Coated nonmagnetic spheres with a negative index of refraction at infrared frequencies," *Phys. Rev. B*, vol. 73, no. 4, p. 45105, Jan. 2006.

[61] U. K. Chettiar, A. V. Kildishev, T. A. Klar, and V. M. Shalaev, "Negative index metamaterial combining magnetic resonators with metal films," *Opt. Express*, vol. 14, no. 17, p. 7872, 2006.

[62] S. Zhang, W. Fan, K. J. Malloy, S. R. J. Brueck, N. C. Panoiu, and R. M. Osgood, "Demonstration of metal-dielectric negative-index metamaterials with improved performance at optical frequencies," *J. Opt. Soc. Am. B*, vol. 23, no. 3, p. 434, Mar. 2006.

[63] V. M. Shalaev *et al.*, "Negative index of refraction in optical metamaterials," *Opt. Lett.*, vol. 30, no. 24, p. 3356, Dec. 2005.

[64] S. Zhang, W. Fan, N. C. Panoiu, K. J. Malloy, R. M. Osgood, and S. R. J. Brueck, "Experimental Demonstration of Near-Infrared Negative-Index Metamaterials," *Phys. Rev. Lett.*, vol. 95, no. 13, p. 137404, Sep. 2005.

[65] G. Dolling, C. Enkrich, M. Wegener, C. M. Soukoulis, and S. Linden, "Simultaneous Negative Phase and Group Velocity of Light in a Metamaterial," *Science (80-.).*, vol. 312, no. 5775, 2006.

[66] J. Yao *et al.*, "Optical Negative Refraction in Bulk Metamaterials of Nanowires," *Science (80-.).*, vol. 321, no. 5891, 2008.

[67] S. P. Burgos, R. de Waele, A. Polman, and H. A. Atwater, "A single-layer wide-angle negative-index metamaterial at visible frequencies," *Nat. Mater.*, vol. 9, no. 5, pp. 407–412, May 2010.

[68] R. A. Shelby, D. R. Smith, and S. Schultz, "Experimental verification of a negative index of refraction.," *Science*, vol. 292, no. 5514, pp. 77–9, Apr. 2001.

[69] J. Valentine *et al.*, "Three-dimensional optical metamaterial with a negative refractive index," *Nature*, vol. 455, no. 7211, pp. 376–379, Sep. 2008.

[70] M. W. McCall *et al.*, "The negative index of refraction demystified," *Eur. J. Phys.*, vol. 23, no. 3, p. 314, May 2002.

[71] A. D. Boardman, N. King, and L. Velasco, "Negative Refraction in Perspective," *Electromagnetics*, vol. 25, no. 5, pp. 365–389, Jul. 2005.

[72] E. Cubukcu, K. Aydin, E. Ozbay, S. Foteinopoulou, and C. M. Soukoulis, "Electromagnetic waves: Negative refraction by photonic crystals," *Nature*, vol. 423, no. 6940, pp. 604–605, Jun. 2003.

[73] P. V. Parimi, W. T. Lu, P. Vodo, J. Sokoloff, J. S. Derov, and S. Sridhar, "Negative Refraction and Left-Handed Electromagnetism in Microwave Photonic Crystals," *Phys. Rev. Lett.*, vol. 92, no. 12, p. 127401, Mar. 2004.

[74] A. Berrier *et al.*, "Negative Refraction at Infrared Wavelengths in a Two-Dimensional Photonic Crystal," *Phys. Rev. Lett.*, vol. 93, no. 7, p. 73902, Aug. 2004.

[75] M. Notomi *et al.*, "Manipulating light with strongly modulated photonic crystals," *Reports Prog. Phys.*, vol. 73, no. 9, p. 96501, Sep. 2010.

[76] Y. Zhang, B. Fluegel, and A. Mascarenhas, "Total Negative Refraction in Real Crystals for Ballistic Electrons and Light," *Phys. Rev. Lett.*, vol. 91, no. 15, p. 157404, Oct. 2003.

[77] N. Yu *et al.*, "Light propagation with phase discontinuities: generalized laws of reflection and refraction.," *Science*, vol. 334, no. 6054, pp. 333–7, Oct. 2011.

[78] F. Aieta, P. Genevet, N. Yu, M. A. Kats, Z. Gaburro, and F. Capasso, "Out-of-Plane Reflection and Refraction of Light by Anisotropic Optical Antenna Metasurfaces with Phase Discontinuities," *Nano Lett.*, vol. 12, no. 3, pp. 1702–1706, Mar. 2012.

[79] S. Larouche and D. R. Smith, "Reconciliation of generalized refraction with diffraction theory," *Opt. Lett.*, vol. 37, no. 12, p. 2391, Jun. 2012.

[80] J. B. Pendry, D. Schurig, and D. R. Smith, "Controlling electromagnetic fields.," *Science*, vol. 312, no. 5781, pp. 1780–2, Jun. 2006.

[81] D. Schurig *et al.*, "Metamaterial electromagnetic cloak at microwave frequencies.," *Science*, vol. 314, no. 5801, pp. 977–80, Nov. 2006.

[82] A. Alù and N. Engheta, "Achieving transparency with plasmonic and metamaterial coatings," *Phys. Rev. E*, vol. 72, no. 1, p. 16623, Jul. 2005.

[83] H. Chen, Z. Liang, P. Yao, X. Jiang, H. Ma, and C. T. Chan, "Extending the bandwidth of electromagnetic cloaks," *Phys. Rev. B*, vol. 76, no. 24, p. 241104, Dec. 2007.

[84] S. Xu *et al.*, "Experimental Demonstration of a Free-Space Cylindrical Cloak without Superluminal Propagation," *Phys. Rev. Lett.*, vol. 109, no. 22, p. 223903, Nov. 2012.

[85] P.-Y. Chen, C. Argyropoulos, and A. Alù, "Broadening the Cloaking Bandwidth with Non-Foster Metasurfaces," *Phys. Rev. Lett.*, vol. 111, no. 23, p. 233001, Dec. 2013.

[86] K. Aydin, Z. Li, L. Sahin, and E. Ozbay, "Negative phase advance in polarization independent, multi-layer negative-index metamaterials," *Opt. Express*, vol. 16, no. 12, p. 8835, Jun. 2008.

[87] C. Helgert *et al.*, "Polarization-independent negative-index metamaterial in the near infrared," *Opt. Lett.*, vol. 34, no. 5, p. 704, Mar. 2009.

[88] N. Liu, H. Guo, L. Fu, S. Kaiser, H. Schweizer, and H. Giessen, "Three-dimensional photonic metamaterials at optical frequencies," *Nat. Mater.*, vol. 7, no. 1, pp. 31–37, Jan. 2008.

[89] C.-Y. Chen *et al.*, "Control of polarization-dependent permittivity in split-ring resonators under electric excitation," *J. Phys. D. Appl. Phys.*, vol. 42, no. 18, p. 185402, Sep. 2009.

[90] T. J. Yen *et al.*, "Terahertz magnetic response from artificial materials.," *Science*, vol. 303, no. 5663, pp. 1494–6, Mar. 2004.

[91] S. I. Maslovski, S. A. Tretyakov, and P. A. Belov, "Wire media with negative effective permittivity: A quasi-static model," *Microw. Opt. Technol. Lett.*, vol. 35, no. 1, pp. 47–51, Oct. 2002.

[92] H. Chen *et al.*, "A meta-substrate to enhance the bandwidth of metamaterials.," *Sci. Rep.*, vol. 4, p. 5264, Jan. 2014.

[93] M. Karami and M. A. Fiddy, “Effect of metamaterial substrates on bandwidth,” pp. 1–2.

[94] M. Karami and M. A. Fiddy, “Controlling the bandwidth of metamaterial properties,” in *SPIE Nanoscience + Engineering*, 2015, p. 954432.

[95] M. Karami, C. Rosenbury, S. Kitchin, and M. A. Fiddy, “Negative-index Polarization-independent Metamaterial,” in *CLEO: 2015*, 2015, p. JTu5A.107.

[96] E. Abbe, “Beiträge zur Theorie des Mikroskops und der mikroskopischen Wahrnehmung,” *Arch. für Mikroskopische Anat.*, vol. 9, no. 1, pp. 413–418, Dec. 1873.

[97] S. W. Hell, “Far-Field Optical Nanoscopy,” *Science (80-.).*, vol. 316, no. 5828, 2007.

[98] L. Schermelleh, R. Heintzmann, and H. Leonhardt, “A guide to super-resolution fluorescence microscopy,” *J. Cell Biol.*, vol. 190, no. 2, 2010.

[99] D. S. Lidke and K. A. Lidke, “Advances in high-resolution imaging – techniques for three-dimensional imaging of cellular structures,” *J. Cell Sci.*, vol. 125, no. 11, 2012.

[100] E. T. F. Rogers and N. I. Zheludev, “Optical super-oscillations: sub-wavelength light focusing and super-resolution imaging,” *J. Opt.*, vol. 15, no. 9, p. 94008, Sep. 2013.

[101] J. B. Pendry, “Negative Refraction Makes a Perfect Lens,” *Phys. Rev. Lett.*, vol. 85, no. 18, pp. 3966–3969, Oct. 2000.

[102] J. Pendry, “Negative refraction,” *Contemp. Phys.*, vol. 45, no. 3, pp. 191–202, May 2004.

[103] R. A. Shelby, D. R. Smith, S. C. Nemat-Nasser, and S. Schultz, “Microwave transmission through a two-dimensional, isotropic, left-handed metamaterial,” *Appl. Phys. Lett.*, vol. 78, no. 4, p. 489, 2001.

[104] Y.-J. Hsu, Y.-C. Huang, J.-S. Lih, and J.-L. Chern, “Electromagnetic resonance in deformed split ring resonators of left-handed meta-materials,” *J. Appl. Phys.*, vol. 96, no. 4, p. 1979, 2004.

[105] Z. Jacob, I. Smolyaninov, and E. Narimanov, “Broadband Purcell effect: Radiative decay engineering with metamaterials,” Oct. 2009.

[106] A. Greenleaf, Y. Kurylev, M. Lassas, and G. Uhlmann, “Cloaking Devices, Electromagnetic Wormholes, and Transformation Optics,” *SIAM Rev.*, vol. 51, no. 1, pp. 3–33, Feb. 2009.

[107] H. J. Lezec, J. A. Dionne, and H. A. Atwater, “Negative Refraction at Visible Frequencies,” *Science (80-.).*, vol. 316, no. 5823, 2007.

[108] B. D. F. Casse, W. T. Lu, Y. J. Huang, E. Gultepe, L. Menon, and S. Sridhar, “Super-resolution imaging using a three-dimensional metamaterials nanolens,” *Appl. Phys. Lett.*, vol. 96, no. 2, p. 23114, 2010.

[109] D. O. S. Melville and R. J. Blaikie, “Super-resolution imaging through a planar silver layer,” *Opt. Express*, vol. 13, no. 6, p. 2127, 2005.

[110] D. Lu *et al.*, “Hyperlenses and metalenses for far-field super-resolution imaging,” *Nat. Commun.*, vol. 3, pp. 189–195, Nov. 2012.

[111] R. S. Hegde *et al.*, “The Dynamics of Nanoscale Superresolution Imaging With the Superlens,” vol. 59, no. 10, pp. 2612–2623, 2011.

[112] R. E. Collin and R. Emanuel, “FREQUENCY DISPERSION LIMITS RESOLUTION IN VESELAGO LENS,” *Prog. Electromagn. Res. B*, vol. 19, pp. 233–261, 2010.

[113] R. Merlin, “Analytical solution of the almost-perfect-lens problem,” *Appl. Phys. Lett.*, vol. 84, no. 8, p. 1290, 2004.

[114] G. Gómez-Santos, “Universal Features of the Time Evolution of Evanescent Modes in a Left-Handed Perfect Lens,” *Phys. Rev. Lett.*, vol. 90, no. 7, p. 77401, Feb. 2003.

[115] D. R. Smith, D. Schurig, M. Rosenbluth, S. Schultz, S. A. Ramakrishna, and J. B. Pendry, “Limitations on subdiffraction imaging with a negative refractive index slab,” *Appl. Phys. Lett.*, vol. 82, no. 10, p. 1506, 2003.

[116] R. W. Ziolkowski and E. Heyman, “Wave propagation in media having negative permittivity and permeability,” *Phys. Rev. E*, vol. 64, no. 5, p. 56625, Oct. 2001.

[117] V. A. Podolskiy and E. E. Narimanov, “Near-sighted superlens,” *Opt. Lett.*, vol. 30, no. 1, p. 75, Jan. 2005.

[118] Y. Zhang, T. M. Grzegorczyk, and J. A. Kong, “Propagation of electromagnetic waves in a slab with negative permittivity and negative permeability,” *Prog.*

Electromagn. Res., vol. 35, pp. 271–286, 2002.

[119] Z. Liu, N. Fang, T.-J. Yen, and X. Zhang, "Rapid growth of evanescent wave by a silver superlens," *Appl. Phys. Lett.*, vol. 83, no. 25, p. 5184, 2003.

[120] N. Fang, Z. Liu, T.-J. Yen, and X. Zhang, "Regenerating evanescent waves from a silver superlens," *Opt. Express*, vol. 11, no. 7, p. 682, Apr. 2003.

[121] A. Giannattasio, I. R. Hooper, and W. L. Barnes, "Transmission of light through thin silver films via surface plasmon-polaritons," *Opt. Express*, vol. 12, no. 24, p. 5881, 2004.

[122] S. A. RAMAKRISHNA, J. B. PENDRY, D. SCHURIG, D. R. SMITH, and S. SCHULTZ, "The asymmetric lossy near-perfect lens," *J. Mod. Opt.*, vol. 49, no. 10, pp. 1747–1762, Aug. 2002.

[123] G. W. 't Hooft, "Comment on 'Negative Refraction Makes a Perfect Lens,'" *Phys. Rev. Lett.*, vol. 87, no. 24, p. 249701, Nov. 2001.

[124] M. Nieto-Vesperinas and N. Garcia, "Nieto-Vesperinas and Garcia Reply:," *Phys. Rev. Lett.*, vol. 91, no. 9, p. 99702, Aug. 2003.

[125] J. M. Williams, "Some Problems with Negative Refraction," *Phys. Rev. Lett.*, vol. 87, no. 24, p. 249703, Nov. 2001.

[126] N. Garcia and M. Nieto-Vesperinas, "Is there an experimental verification of a negative index of refraction yet?," *Opt. Lett.*, vol. 27, no. 11, p. 885, Jun. 2002.

[127] M.-C. Yang and K. J. Webb, "Poynting vector analysis of a superlens," *Opt. Lett.*, vol. 30, no. 18, p. 2382, Sep. 2005.

[128] D. W. Ward *et al.*, "On the physical origins of the negative index of refraction," *New J. Phys.*, vol. 7, no. 1, pp. 213–213, Oct. 2005.

[129] X.-X. Liu and A. Alù, "Limitations and potentials of metamaterial lenses," *J. Nanophotonics*, vol. 5, no. 1, p. 53509, Jan. 2011.

[130] Y. Zhang, Y.-C. Chuang, J. Schenk, and M. Fiddy, "Study of scattering patterns and subwavelength scale imaging based on finite-sized metamaterials," *Appl. Phys. A*, vol. 107, no. 1, pp. 61–69, 2012.

[131] C. P. Moore, R. J. Blaikie, and M. D. Arnold, "An improved transfer-matrix model

for optical superlenses," *Opt. Express*, vol. 17, no. 16, pp. 14260–14269, Aug. 2009.

[132] A. P. Mosk, A. Lagendijk, G. Lerosey, and M. Fink, "Controlling waves in space and time for imaging and focusing in complex media," *Nat. Photonics*, vol. 6, no. 5, pp. 283–292, 2012.

[133] Z. Liu, V. Shalaev, and A. Kildishev, "Coupling effect in a near-field object–superlens system," *Appl. Phys. A*, vol. 107, no. 1, pp. 83–88, 2012.

[134] S. Huang, H. Wang, K.-H. Ding, and L. Tsang, "Subwavelength imaging enhancement through a three-dimensional plasmon superlens with rough surface," *Opt. Lett.*, vol. 37, no. 8, pp. 1295–1297, Apr. 2012.

[135] S. Maslovski and S. Tretyakov, "Phase conjugation and perfect lensing," *J. Appl. Phys.*, vol. 94, no. 7, p. 4241, Sep. 2003.

[136] S. Maslovski *et al.*, "Perfect lensing with phase-conjugating surfaces: toward practical realization," *New J. Phys.*, vol. 14, no. 3, p. 35007, Mar. 2012.

[137] J. B. Pendry, "Time reversal and negative refraction.," *Science*, vol. 322, no. 5898, pp. 71–3, Oct. 2008.

[138] S. Palomba, S. Zhang, Y. Park, G. Bartal, X. Yin, and X. Zhang, "Optical negative refraction by four-wave mixing in thin metallic nanostructures.," *Nat. Mater.*, vol. 11, no. 1, pp. 34–8, Jan. 2012.

[139] Y. Urzhumov, C. Ciracì, and D. R. Smith, "Nanophotonics: Optical time reversal with graphene," *Nat. Phys.*, vol. 9, no. 7, pp. 393–394, Jul. 2013.

[140] H. Harutyunyan, R. Beams, and L. Novotny, "Controllable optical negative refraction and phase conjugation in graphite thin films," *Nat. Phys.*, vol. 9, no. 7, pp. 423–425, May 2013.

[141] R. Fleury, D. L. Sounas, and A. Alù, "Negative Refraction and Planar Focusing Based on Parity-Time Symmetric Metasurfaces," *Phys. Rev. Lett.*, vol. 113, no. 2, p. 23903, Jul. 2014.

[142] H. Alaeian and J. A. Dionne, "Parity-time-symmetric plasmonic metamaterials," *Phys. Rev. A*, vol. 89, no. 3, p. 33829, Mar. 2014.

[143] G. Rosenblatt and M. Orenstein, "Perfect Lensing by a Single Interface: Defying Loss and Bandwidth Limitations of Metamaterials," *Phys. Rev. Lett.*, vol. 115, no.

19, p. 195504, Nov. 2015.

[144] N. Fang, H. Lee, C. Sun, and X. Zhang, "Sub–Diffraction-Limited Optical Imaging with a Silver Superlens," *Sci.* , vol. 308, no. 5721, pp. 534–537, Apr. 2005.

[145] J. B. Khurgin and G. Sun, "In search of the elusive lossless metal," *Appl. Phys. Lett.*, vol. 96, no. 18, p. 181102, 2010.

[146] M. G. Blaber *et al.*, "A review of the optical properties of alloys and intermetallics for plasmonics," *J. Phys. Condens. Matter*, vol. 22, no. 14, p. 143201, Apr. 2010.

[147] M. Jablan, H. Buljan, and M. Soljačić, "Plasmonics in graphene at infrared frequencies," *Phys. Rev. B*, vol. 80, no. 24, p. 245435, Dec. 2009.

[148] P. Tassin, T. Koschny, M. Kafesaki, and C. M. Soukoulis, "A comparison of graphene, superconductors and metals as conductors for metamaterials and plasmonics," *Nat. Photonics*, vol. 6, no. 4, pp. 259–264, Mar. 2012.

[149] A. J. Hoffman *et al.*, "Negative refraction in semiconductor metamaterials," *Nat. Mater.*, vol. 6, no. 12, pp. 946–950, Dec. 2007.

[150] G. V. Naik and A. Boltasseva, "Semiconductors for plasmonics and metamaterials," *Phys. status solidi - Rapid Res. Lett.*, vol. 4, no. 10, pp. 295–297, Oct. 2010.

[151] S. Anantha Ramakrishna and J. B. Pendry, "Removal of absorption and increase in resolution in a near-field lens via optical gain," *Phys. Rev. B*, vol. 67, no. 20, p. 201101, May 2003.

[152] S. Durant, Z. Liu, J. M. Steele, and X. Zhang, "Theory of the transmission properties of an optical far-field superlens for imaging beyond the diffraction limit," *J. Opt. Soc. Am. B*, vol. 23, no. 11, p. 2383, Nov. 2006.

[153] Zhaowei Liu *et al.*, "Far-Field Optical Superlens," 2007.

[154] Z. Liu *et al.*, "Experimental studies of far-field superlens for sub-diffractional optical imaging," *Opt. Express*, vol. 15, no. 11, p. 6947, 2007.

[155] A. Poddubny, I. Iorsh, P. Belov, and Y. Kivshar, "Hyperbolic metamaterials," *Nat. Photonics*, vol. 7, no. 12, pp. 948–957, Nov. 2013.

[156] L. Ferrari, C. Wu, D. Lepage, X. Zhang, and Z. Liu, "Hyperbolic metamaterials and their applications," *Prog. Quantum Electron.*, Nov. 2014.

[157] D. Lu, J. J. Kan, E. E. Fullerton, and Z. Liu, “Enhancing spontaneous emission rates of molecules using nanopatterned multilayer hyperbolic metamaterials,” *Nat. Nanotechnol.*, vol. 9, no. 1, pp. 48–53, Jan. 2014.

[158] M. A. Noginov *et al.*, “Controlling spontaneous emission with metamaterials,” *Opt. Lett.*, vol. 35, no. 11, p. 1863, Jun. 2010.

[159] Z. Yu *et al.*, “Enhancing far-field thermal emission with thermal extraction,” *Nat. Commun.*, vol. 4, p. 1730, Apr. 2013.

[160] Y. Guo, C. L. Cortes, S. Molesky, and Z. Jacob, “Broadband super-Planckian thermal emission from hyperbolic metamaterials,” *Appl. Phys. Lett.*, vol. 101, no. 13, p. 131106, 2012.

[161] J. Sun, M. I. Shalaev, and N. M. Litchinitser, “Experimental demonstration of a non-resonant hyperlens in the visible spectral range.,” *Nat. Commun.*, vol. 6, p. 7201, Jan. 2015.

[162] Z. Jacob, L. V Alekseyev, and E. Narimanov, “Optical Hyperlens: Far-field imaging beyond the diffraction limit,” *Opt. Express*, vol. 14, no. 18, pp. 8247–8256, Sep. 2006.

[163] A. Salandrino and N. Engheta, “Far-field subdiffraction optical microscopy using metamaterial crystals: Theory and simulations,” *Phys. Rev. B*, vol. 74, no. 7, p. 75103, Aug. 2006.

[164] B. Wood, J. B. Pendry, and D. P. Tsai, “Directed subwavelength imaging using a layered metal-dielectric system,” *Phys. Rev. B*, vol. 74, no. 11, p. 115116, Sep. 2006.

[165] Z. Liu, H. Lee, Y. Xiong, C. Sun, and X. Zhang, “Far-Field Optical Hyperlens Magnifying Sub-Diffraction-Limited Objects,” *Science (80-.).*, vol. 315, no. 5819, 2007.

[166] H. Lee, Z. Liu, Y. Xiong, C. Sun, and X. Zhang, “Development of optical hyperlens for imaging below the diffraction limit,” *Opt. Express*, vol. 15, no. 24, p. 15886, 2007.

[167] J. Rho *et al.*, “Spherical hyperlens for two-dimensional sub-diffractional imaging at visible frequencies,” *Nat. Commun.*, vol. 1, no. 9, p. 143, Dec. 2010.

[168] I. I. Smolyaninov, Y.-J. Hung, and C. C. Davis, “Magnifying Superlens in the Visible Frequency Range,” *Science (80-.).*, vol. 315, no. 5819, 2007.

[169] W. Zhang, H. Chen, and H. O. Moser, “Subwavelength imaging in a cylindrical hyperlens based on S-string resonators,” *Appl. Phys. Lett.*, vol. 98, no. 7, p. 73501, 2011.

[170] Y.-C. Chuang, R. Dudley, and M. a. Fiddy, “Superresolved image reconstruction from incomplete data,” vol. 8500, pp. 850009-850009–9, Oct. 2012.

[171] R. S. Ritter and M. A. Fiddy, “Superresolution imaging from nonlinear inverse scattering,” 2015, p. 96000D.

[172] M. E. Testorf and M. A. Fiddy, “Chapter 5 – Superresolution Imaging—Revisited,” in *Advances in Imaging and Electron Physics*, vol. 163, 2010, pp. 165–218.

[173] R. S. Ritter and M. A. Fiddy, “Imaging from scattered fields: limited data and degrees of freedom,” 2012, p. 850007.

[174] F. Simonetti, M. Fleming, and E. A. Marengo, “Illustration of the role of multiple scattering in subwavelength imaging from far-field measurements,” *J. Opt. Soc. Am. A*, vol. 25, no. 2, p. 292, Feb. 2008.

[175] G. Lerosey, J. de Rosny, A. Tourin, and M. Fink, “Focusing beyond the diffraction limit with far-field time reversal.,” *Science*, vol. 315, no. 5815, pp. 1120–2, Feb. 2007.

[176] R. J. Potton, “Reciprocity in optics,” *Reports Prog. Phys.*, vol. 67, no. 5, pp. 717–754, May 2004.

[177] S. Longhi *et al.*, “Invisibility in $\mathcal {PT}$-symmetric complex crystals,” *J. Phys. A Math. Theor.*, vol. 44, no. 48, p. 485302, Dec. 2011.

[178] M. Lawrence *et al.*, “Manifestation of P T Symmetry Breaking in Polarization Space with Terahertz Metasurfaces,” *Phys. Rev. Lett.*, vol. 113, no. 9, p. 93901, Aug. 2014.

[179] R. Carminati, M. Nieto-Vesperinas, and J.-J. Greffet, “Reciprocity of evanescent electromagnetic waves,” *J. Opt. Soc. Am. A*, vol. 15, no. 3, p. 706, Mar. 1998.

[180] R. Carminati, J. J. Sáenz, J.-J. Greffet, and M. Nieto-Vesperinas, “Reciprocity, unitarity, and time-reversal symmetry of the S matrix of fields containing evanescent components,” *Phys. Rev. A*, vol. 62, no. 1, p. 12712, Jun. 2000.

[181] Jin Au Kong, “Theorems of bianisotropic media,” *Proc. IEEE*, vol. 60, no. 9, pp.

1036–1046, 1972.

[182] A. R. Katko, S. Gu, J. P. Barrett, B.-I. Popa, G. Shvets, and S. A. Cummer, "Phase Conjugation and Negative Refraction using Nonlinear Active Metamaterials," *Phys. Rev. Lett.*, vol. 105, no. 12, p. 123905, Sep. 2010.

[183] N. D. Taket and M. A. Fiddy, "Theory of distortion correction by phase conjugation for strongly scattering media," *J. Opt. Soc. Am. A*, vol. 4, no. 10, p. 1869, Oct. 1987.

[184] F.-C. Chen and W. C. Chew, "Experimental verification of super resolution in nonlinear inverse scattering," *Appl. Phys. Lett.*, vol. 72, no. 23, p. 3080, 1998.

[185] H. Y. Xie, P. T. Leung, and D. P. Tsai, "Clarification and extension of the optical reciprocity theorem," *J. Math. Phys.*, vol. 50, no. 7, p. 72901, Jul. 2009.

[186] W. J. R. Hoefer, "Computational Time Reversal—A Frontier in Electromagnetic Structure Synthesis and Design," *IEEE Trans. Microw. Theory Tech.*, vol. 63, no. 1, pp. 3–10, Jan. 2015.

[187] A. R. Katko *et al.*, "Phase conjugation metamaterials: particle design and imaging experiments," *J. Opt.*, vol. 14, no. 11, p. 114003, Nov. 2012.

[188] L. Zhang, T. Koschny, and C. M. Soukoulis, "Creating double negative index materials using the Babinet principle with one metasurface," *Phys. Rev. B*, vol. 87, no. 4, p. 45101, Jan. 2013.

[189] Y. Nakata, Y. Urade, T. Nakanishi, and M. Kitano, "Plane-wave scattering by self-complementary metasurfaces in terms of electromagnetic duality and Babinet's principle," *Phys. Rev. B*, vol. 88, no. 20, p. 205138, Nov. 2013.

[190] T. Chen, S. Li, and H. Sun, "Metamaterials application in sensing.," *Sensors (Basel).*, vol. 12, no. 3, pp. 2742–65, Jan. 2012.

[191] M. Huang and J. Yang, "Microwave Sensor Using Metamaterials," 2007.

[192] L.-W. Li, Y.-N. Li, T. S. Yeo, J. R. Mosig, and O. J. F. Martin, "A broadband and high-gain metamaterial microstrip antenna," *Appl. Phys. Lett.*, vol. 96, no. 16, 2010.

[193] P. P. Markowicz, W. C. Law, A. Baev, P. N. Prasad, S. Patskovsky, and A. Kabashin, "Phase-sensitive time-modulated surface plasmon resonance polarimetry for wide dynamic range biosensing," *Opt. Express*, vol. 15, no. 4, p. 1745, Feb. 2007.

[194] A. G. Markelz, “Terahertz Dielectric Sensitivity to Biomolecular Structure and Function,” *IEEE J. Sel. Top. Quantum Electron.*, vol. 14, no. 1, pp. 180–190, 2008.

[195] M. Labidi, J. B. Tahar, and F. Choubani, “Meta-materials applications in thin- film sensing and sensing liquids properties,” *Opt. Express*, vol. 19, no. S4, p. A733, Jul. 2011.

[196] J. Y. Ou, E. Plum, L. Jiang, and N. I. Zheludev, “Reconfigurable Photonic Metamaterials,” *Nano Lett.*, vol. 11, no. 5, pp. 2142–2144, May 2011.

[197] X. He, Y. Wang, J. Wang, and T. Gui, “Thin-film sensor based tip-shaped split ring resonator metamaterial for microwave application,” *Microsyst. Technol.*, vol. 16, no. 10, pp. 1735–1739, Oct. 2010.

[198] R. Melik, N. K. Perkgoz, E. Unal, Z. Dilli, and H. V. Demir, “Design and Realization of a Fully On-Chip High-Q Resonator at 15 GHz on Silicon,” *IEEE Trans. Electron Devices*, vol. 55, no. 12, pp. 3459–3466, Dec. 2008.

[199] C.-Y. Chen, I.-W. Un, N.-H. Tai, and T.-J. Yen, “Asymmetric coupling between subradiant and superradiant plasmonic resonances and its enhanced sensing performance,” *Opt. Express*, vol. 17, no. 17, p. 15372, Aug. 2009.

[200] R. Singh, C. Rockstuhl, and W. Zhang, “Strong influence of packing density in terahertz metamaterials,” *Appl. Phys. Lett.*, vol. 97, no. 24, p. 241108, 2010.

[201] R. Singh, Z. Tian, J. Han, C. Rockstuhl, J. Gu, and W. Zhang, “Cryogenic temperatures as a path toward high-Q terahertz metamaterials,” *Appl. Phys. Lett.*, vol. 96, no. 7, p. 71114, 2010.

[202] M. Huang, J. Yang, J. Sun, J. Shi, and J. Peng, “Modelling and Analysis of Ω-shaped Double Negative Material-assisted Microwave Sensor,” *J. Infrared, Millimeter, Terahertz Waves*, vol. 30, no. 11, pp. 1131–1138, Nov. 2009.

[203] X. Xu *et al.*, “Flexible Visible–Infrared Metamaterials and Their Applications in Highly Sensitive Chemical and Biological Sensing,” *Nano Lett.*, vol. 11, no. 8, pp. 3232–3238, Aug. 2011.

[204] R. Melik, E. Unal, N. Kosku Perkgoz, C. Puttlitz, and H. V. Demir, “Flexible metamaterials for wireless strain sensing,” *Appl. Phys. Lett.*, vol. 95, no. 18, p. 181105, 2009.

[205] J. Li *et al.*, “Mechanically tunable terahertz metamaterials,” *Appl. Phys. Lett.*, vol.

102, no. 12, p. 121101, 2013.

[206] A. Karvounis, J.-Y. Ou, W. Wu, K. F. MacDonald, and N. I. Zheludev, “Nano-optomechanical nonlinear dielectric metamaterials,” *Appl. Phys. Lett.*, vol. 107, no. 19, p. 191110, Nov. 2015.

[207] R. Singh, A. K. Azad, J. F. O’Hara, A. J. Taylor, and W. Zhang, “Effect of metal permittivity on resonant properties of terahertz metamaterials,” *Opt. Lett.*, vol. 33, no. 13, p. 1506, Jul. 2008.

[208] V. A. Kalinin and V. V. Shtykov, “The possibility of phase conjugation for radio waves in an artificial nonlinear medium,” *Radiotekhnika i Elektron. (ISSN 0033-8494), vol. 35, Nov. 1990, p. 2275-2281. Russ.*, vol. 35, pp. 2275–2281, 1990.

[209] J. B. Pendry, A. J. Holden, D. J. Robbins, and W. J. Stewart, “Magnetism from conductors and enhanced nonlinear phenomena,” *IEEE Trans. Microw. Theory Tech.*, vol. 47, no. 11, pp. 2075–2084, 1999.

[210] A. A. Zharov, I. V. Shadrivov, and Y. S. Kivshar, “Nonlinear Properties of Left-Handed Metamaterials,” *Phys. Rev. Lett.*, vol. 91, no. 3, p. 37401, Jul. 2003.

[211] M. Lapine, M. Gorkunov, and K. H. Ringhofer, “Nonlinearity of a metamaterial arising from diode insertions into resonant conductive elements,” *Phys. Rev. E*, vol. 67, no. 6, p. 65601, Jun. 2003.

[212] V. M. Agranovich, Y. R. Shen, R. H. Baughman, and A. A. Zakhidov, “Linear and nonlinear wave propagation in negative refraction metamaterials,” *Phys. Rev. B*, vol. 69, no. 16, p. 165112, Apr. 2004.

[213] M. Ren, B. Jia, J. Y. Ou, E. Plum, K. F. Macdonald, and A. E. Nikolaenko, “Giant femtosecond optical nonlinearity of gold metamaterial nanostructures,” in *Metamaterials 2011*, 2011, vol. 1, pp. 1–3.

[214] A. I. Ryasnyanskiy, B. Palpant, S. Debrus, U. Pal, and A. Stepanov, “Third-order nonlinear-optical parameters of gold nanoparticles in different matrices,” *J. Lumin.*, vol. 127, no. 1, pp. 181–185, 2007.

[215] N. Suzuki, “FDTD Analysis of Two-Photon Absorption and Free-Carrier Absorption in Si High-Index-Contrast Waveguides,” *J. Light. Technol.*, vol. 25, no. 9, pp. 2495–2501, Sep. 2007.

[216] I. S. Maksymov, L. F. Marsal, and J. Pallarès, “An FDTD Analysis of Nonlinear

Photonic Crystal Waveguides," *Opt. Quantum Electron.*, vol. 38, no. 1–3, pp. 149–160, Jan. 2006.

[217] R. W. Ziolkowski, "The incorporation of microscopic material models into the FDTD approach for ultrafast optical pulse simulations," *IEEE Trans. Antennas Propag.*, vol. 45, no. 3, pp. 375–391, Mar. 1997.

[218] I. S. Maksymov, L. F. Marsal, and J. Pallarès, "Modeling of two-photon absorption in nonlinear photonic crystal all-optical switch," *Opt. Commun.*, vol. 269, no. 1, pp. 137–141, Jan. 2007.

APPENDIX A: MATLAB CODE TO EXTRACT EFFECTIVE PARAMETERS

```
%%% This program calculates Effective Parameters of selected
Metamaterials
%%% Ref. Chen et al. "Robust method to retrieve the constitutive
effective parameters of metamaterials," Physical Review E 70, 016608
(2004)
%%% Last updated: 6/10/2014 by Morteza Karami


%% Step - 1: Plots magnitudes of S parameters for structure
% the unit of the thickness should be [m], otherwise the calculated n
might not have correct order

d=6.4*10^-3; %[m] metamaterial bulk thickness in the propagation
direction

S=importdata('Sparameters.txt');
% S(:,1)->frequency
% S(:,2)->|S11|
% S(:,3)->phase angle of S11 in deg
% S(:,4)->|S21|
% S(:,5)->phase angle of S21 in deg

f0=S(:,1);% freq [GHz]
f=S(:,1)*10^9; % freq [Hz]

S11=zeros(length(f),1);
S21=zeros(length(f),1);
k0=zeros(length(f),1);
S11_mag=S(:,2);
S11_phas=S(:,3);
S21_mag=S(:,4);
S21_phas=S(:,5);

S11=S(:,2).*cos((S(:,3)./180)*pi)-1i*S(:,4).*sin((S(:,3)./180)*pi);
S21=S(:,4).*cos((S(:,5)./180)*pi)-1i*S(:,4).*sin((S(:,5)./180)*pi);
k0=2*pi*f./3e8;
lambda=3e8./f*1e6; %[um]

figure(1)
```

```
plot(f0,S(:,2),'LineWidth',2) %S11
hold on
grid on
plot(f0,S(:,4),'r-.','LineWidth',2) %S21

title('S parameter of Metamaterial')
xlabel('Frequency [GHz]')
ylabel('S parameters')
legend('S_1_1','S_2_1')
hold off

%% Step - 2: Plots phases of S parameters for structure
% need to manually fix the discontinuous part if necessary
figure(2)
plot(f0,S(:,3),'LineWidth',2) %[deg]
hold on
grid on
plot(f0,S(:,5),'r-.','LineWidth',2) %[deg]

title('S Phase of Metamaterial')
xlabel('Frequency [GHz]')
ylabel('Phase of S parameters [deg.]')
legend('S_1_1','S_2_1')
hold off

%% Step - 3: Implementation of impedance retrieval

z = sqrt(((1.0 + S11).^2 - S21.^2)./((1.0 - S11).^2 -
S21.^2));%Eq.(2a)of Chen(2004)
exp_ink0d = S21./(1.0 - S11.*((z - 1.0)./(z + 1.0)));

% Choosing the proper sign for Re(z) and Im(n)
for ii=1:length(f)
     if (abs(real(z(ii))) >= 1e-1) %if the magnitude of Z is large
enough, we can determine its sign based on Eq.(3a) of Chen (2004)
       if (real(z(ii))<0)
           z(ii)=-z(ii);
           exp_ink0d(ii)=S21(ii)./(1-S11(ii).*(z(ii)-1)./(z(ii)+1));
%Eq(6)of Chen(2004)
       end
     else
       if (abs(exp_ink0d(ii)) > 1.0) %in addition, Z must satisfy
|exp(i*n*k0*d)|<=1; Sec.C of Chen (2004)
           z(ii)=-z(ii);
           exp_ink0d(ii)=S21(ii)./(1-S11(ii).*(z(ii)-1)./(z(ii)+1));
%Eq(6)of Chen(2004)
       end
     end
```

```
end

% Plot of real and imaginary parts of impedance
figure(3)
plot(f0,real(z),'LineWidth',2)
hold on
grid on
plot(f0,imag(z),'r-.','LineWidth',2)
title('Metamaterial Impedance')
xlabel('Frequency [GHz]')
ylabel('Impedance [\Omega]')
legend('Real Z','Imag Z')
hold off

%% Step - 4: Calculate the complex refractive index
% Calculate index(n) branches
mmax=2; % number of index(n) branch calculated/shown
n=zeros(length(f),mmax*2+1); % n matrix
n_Re=zeros(length(f),mmax*2+1); %Re(n) matrix
n_Im=real(log(exp_ink0d))./k0./d; % Im(n))

figure(4);
for mm=-mmax:mmax
    n_Re(:,mm+mmax+1)=(imag(log(exp_ink0d))+2*pi*mm)./k0./d;
    n(:,mm+mmax+1)=n_Re(:,mm+mmax+1)-1i*n_Im; %Eq(4)of Chen(2004)
    plot(f0,n_Re(:,mm+mmax+1),'LineWidth',2);
    hold on
end
hold off

title('Possible Re(n) branches')
xlabel('Frequency [GHz]')
ylabel('Refractive index Re(n)')

%% Step - 5 calculate the complex refractive index
% Calculate the initial branch of index (n)
m_initial=zeros(length(f),mmax*2+1);
Eq9=zeros(length(f),mmax*2+1);

for ii=1:length(f);
    for mm=-mmax:mmax
        Eq9_left(ii,mm+mmax+1)=abs(n_Re(ii,mm+mmax+1)*imag(z(ii)));
        Eq9_right(ii,mm+mmax+1)=-n_Im(ii)*real(z(ii)); % must be
positive
        Eq9(ii,mm+mmax+1)=Eq9_right(ii,mm+mmax+1) -
Eq9_left(ii,mm+mmax+1);

        if Eq9_right(ii,mm+mmax+1) - Eq9_left(ii,mm+mmax+1) < -0.1
```

```
            m_initial(ii,mm+mmax+1)=NaN;
         else
            m_initial(ii,mm+mmax+1)=mm;
         end

    end
end
mstart=m_initial;


%% Determine which branch is valid based on Eq.(7) Chen (2004)

sol=zeros(1,2); %complex n
mstart=input('type in initial branch: ');
n0_true=n_Re(:,mstart+mmax+1);
nf1=zeros(length(f),1);
n_true=n(:,mstart+mmax+1);

for ii=1:length(f)-1; %manually choose the range satisfying Eq(9) Chen
(2004) based on m_initial in Step 5

    A=-0.5*k0(ii+1)^2*d^2;
    B=k0(ii+1)*n(ii,mstart+mmax+1)*k0(ii)*d^2+1i*k0(ii+1)*d;
    C=-(exp_ink0d(ii+1)/exp(1i*n(ii,mstart+mmax+1)*k0(ii)*d)-
1+1i*n(ii,mstart+mmax+1)*k0(ii)*d-
0.5*(1i*n(ii,mstart+mmax+1)*k0(ii)*d)^2);

    sol(1)=(-B+(B^2-4*A*C)^0.5)/(2*A);
    sol(2)=(-B-(B^2-4*A*C)^0.5)/(2*A);
    compare=abs(imag(sol)-imag(n(ii,mstart+mmax+1)));
    whichSolution=find((compare==min(compare)));
    nf1(ii+1)=sol(whichSolution);
    clear compare whichSolution
    compare=abs(n_Re(ii+1,:)-real(nf1(ii+1)));
    m_branch(ii+1)=find((compare==min(compare)))-(mstart+mmax+1);

    if m_branch==0
        n0_true(ii+1)=n_Re(ii+1,mstart+mmax+1);
        % n_true=n(:,mstart+mmax+1); which has been assigned
    else % i.e. if m_branch=0
        n0_true(ii+1)=n_Re(ii+1,mstart+mmax+1+m_branch(ii+1));
        n(ii+1,mstart+mmax+1)=n0_true(ii+1)-1i*n_Im(ii+1);
        n_true(ii+1)=n(ii+1,mstart+mmax+1);
    end
end

% plot true n (real and imag)
figure(6);
```

```
plot(f0,real(n_true),'b','LineWidth',2);
hold on
grid on
plot(f0,imag(n_true),'r-.','LineWidth',2);

title('Metamaterial Refractive Index')
xlabel('Frequency [GHz]')
ylabel('Refractive index')
legend('Real n','Imag n')


%% Step - 6 Calculation of permittivity and permeability using true
index branch
eps=zeros(length(f),1);
mu=zeros(length(f),1);
for ii=1:length(f)
    eps(ii)=n_true(ii)/z(ii);
    mu(ii)=n_true(ii)*z(ii);
end
figure(7)
plot(f0,real(mu),'LineWidth',2)
hold on
grid on
plot(f0,imag(mu),'r-.','LineWidth',2)
title('Metamaterial \mu')
xlabel('Frequency [GHz]')
ylabel('Permeabiliy \mu')
legend('Real \mu','Imag \mu')
hold off

figure(8)
plot(f0,real(eps),'LineWidth',2)
hold on
grid on
plot(f0,imag(eps),'r-.','LineWidth',2)
title('Metamaterial \epsilon')
xlabel('Frequency [GHz]')
ylabel('Permittivity \epsilon')
legend('Real \epsilon','Imag \epsilon')
hold off
```

APPENDIX B: LUMERICAL NONLINEAR MATERIAL PLUGIN

To modify FDTD method in Lumerical, the user can define a specific type of materials with intrinsic characteristics to address the simulation requirements. This advanced feature of the software is through building additional material plugins in C++ programming software. Lumerical's guidelines are available for building the plugin. The user has to implement the theoretical FDTD equations into a suitable algorithm within the defined guidelines.

The following codes represent the codes used to develop the plugin. In C++, multiple files have to be assembled to build the application. The header code sets and defines the variables and their type which later will be used in CPP code. The CPP code contains the main algorithm which is based on the equations of the material polarization.

A.1. Material's Header File Code

```
#ifndef _CHI3KERRTPAITERATION_H
#define _CHI3KERRTPAITERATION_H

#include "imaterialplugin.h"

class Chi3KerrTPAiterationMaterialPlugin : public IMaterialPlugin
{
public:
    Chi3KerrTPAiterationMaterialPlugin(){};
    virtual ~Chi3KerrTPAiterationMaterialPlugin(){};

    const char* name() const {return "Chi3 Kerr TPA iteration";};
    const char* uniqueId() const {return "{F23F3E69-6913-49B2-B51A-
C3A742AD1D86}";};
```

```
    const char** parameterNames() const {return names;};
    float calculateEx( float U, float V, float Ex, float* storage);
    float calculateEy( float U, float V, float Ey, float* storage);
    float calculateEz( float U, float V, float Ez, float* storage);
    void initialize(const double** parameters, double dt);
    void initializeStorageEx(float* storage){};
    void initializeStorageEy(float* storage){};
    void initializeStorageEz(float* storage){};
    size_t storageSizeE() const {return 9;};

private:
    float calculate(int axis, float U, float V, float E, float* storage);

    static const double c;
       static const double eps0;

       double eps_r[3]; //er is relative permittivity of material
       double chi3[3]; // Kerr sussceptiblity
       double betaTPA[3]; // TPA coeficient

    static const char* names[4];
};
#endif
```

A.2. CPP File Code

```
#include "chi3kerrtpaiteration.h"
#include <cmath>

const double Chi3KerrTPAiterationMaterialPlugin::eps0 = 8.854187817e-12; //vacuum
permittivity [F/m]
const double Chi3KerrTPAiterationMaterialPlugin::c = 2.99792458e8; //speed of
light in vacuum [m/s]

const char* Chi3KerrTPAiterationMaterialPlugin::names[4] = {"Permittivity",
"\xcf\x87 3", "betaTPA", 0};

void Chi3KerrTPAiterationMaterialPlugin::initialize(const double** parameters,
double dt)
{

       for(int i=0; i<3; i++){
              eps_r[i] = float(parameters[0][i]);
        chi3[i] = double(parameters[1][i]);
              betaTPA[i] = double(parameters[2][i]*dt);
    }
}

float Chi3KerrTPAiterationMaterialPlugin::calculate(int axis, float U, float V,
float E, float* storage)
```

```
{
	double Vn = (double)storage[0];
	double Un = (double)storage[1];
	double En = double(E);
	double Enp1 = double(E);

	int n = 1.0;
	int ii = 1.0;

	while (n < 6){
		double g1 = chi3[axis] * (Enp1*Enp1) + c*c*eps0*eps_r[axis] * 
betaTPA[axis] * (Enp1*Enp1 + En*En) / 8;
		double g2 = chi3[axis] * (En*En) - c*c*eps0*eps_r[axis] * 
betaTPA[axis] * (Enp1*Enp1 + En*En) / 8;
		Enp1 = 1 / (g1 + U)*((g2+Un)*En + (V - Vn)); //calcluates E from 
D=epsilon*E+P where V = D / e0 and U = Lumerial's background perimittivity for the 
material (plugin assumes this is set to 1)
		n = n + 1;
		storage[ii + 3] = Enp1;
		ii = ii + 1;
	}
		//updating storage
		storage[0] = V;
		storage[1] = U;

		storage[2]= eps_r[axis]; //additional storage field for debugging

	return Enp1;
}

float Chi3KerrTPAiterationMaterialPlugin::calculateEx(float U, float V, float Ex, 
float* storage)
{
    return calculate(0, U, V, Ex, storage);
}

float Chi3KerrTPAiterationMaterialPlugin::calculateEy(float U, float V, float Ey, 
float* storage)
{
    return calculate(1, U, V, Ey, storage);
}

float Chi3KerrTPAiterationMaterialPlugin::calculateEz(float U, float V, float Ez, 
float* storage)
{
    return calculate(2, U, V, Ez, storage);
}

MATERIAL_PLUGIN(Chi3KerrTPAiterationMaterialPlugin);
```